NRL Report 6731

Applications of Computer-Aided Ionospheric Ray Tracing Techniques to the Analysis of Over-the-Horizon Radar Signatures From Launch-Phase Rockets

J. R. Davis, M. E. Harding, J. W. Willis, and F. H. Utley

Radar Techniques Branch
Radar Division

July 30, 1968

Second Printing

NAVAL RESEARCH LABORATORY
Washington, D.C.

CONTENTS

ABSTRACT

NRL's Madre research radar has been used for 11 years in a long-term investigation of the applicability of high-frequency ionospheric radar for detecting and tracking over-the-horizon aircraft and launch-phase rocket vehicles. Associated with this investigation is a concurrent and complementary study of the ionosphere as a propagating medium and of the earth as a scatterer for decameter electromagnetic waves.

An ionospheric ray-tracing program has been developed to perform a propagation analysis which uses ionosonde data from stations located along the transmission path to describe a family of propagation rays between the radar site and a selected target region. This program permits ground-backscatter profiles to be synthesized and compared with observed ground-backscatter data and allows the adjustment of such parameters as the angular dependence of the earth's scattering coefficient and nondeviative absorption of the electromagnetic energy in the ionosphere, to achieve a fit to the observed data. The resultant propagation model is used to predict the behavior of a launch-phase missile's signature as detected by an over-the-horizon radar under appropriate propagation conditions.

The results of this computer-aided propagation analysis were compiled for several Polaris missile launches on the Eastern Test Range and were then compared with data acquired by the Madre radar. The ray-tracing technique has been generally quite successful, for the cases treated, in predicting:

(a) the position and the extent of the ground-backscatter echo,

(b) the locations and the relative amplitude of localized peaks and nulls in the illumination caused by ionospheric layer structure,

(c) the onset and the loss time of missile signatures (with some exceptions),

(d) the doppler shift of missile signatures, including multipath effects, and

(e) the temporary losses of signal due to voids in the illumination of the missile.

PROBLEM STATUS

This is the final report on USAF MIPR FD2310-7-0016, Project 673A. Work will be continued on this and associated problems under different sponsorship.

AUTHORIZATION

NRL Problem R02-23
USAF MIPR FD2310-7-0016

Manuscript submitted April 5, 1968.

APPLICATIONS OF COMPUTER-AIDED IONOSPHERIC RAY-TRACING TECHNIQUES TO THE ANALYSIS OF OVER-THE-HORIZON RADAR SIGNATURES FROM LAUNCH-PHASE ROCKETS

INTRODUCTION

The Madre Research Radar

The Madre research radar is a coherent, moving-target-indicating radar developed by NRL to investigate the utility of high-frequency ionospheric propagation for extending the useful range of radar beyond the geometric horizon. Using single-hop ionospheric propagation alone, the range limit of surface-based radar may be extended from a line-of-sight maximum range of some tens of nautical miles (for near-surface coverage) to an over-the-horizon maximum range of more than 2200 naut mi. Multihop propagation may, under relatively normal, favorable circumstances, permit even greater range coverage. A second attractive feature of ionospheric radar, quite independent of its range-extending feature, is its illumination of the entire region between the earth's surface and the ionospheric reflection height in all the range intervals illuminated. Thus the threat of fly-under is eliminated, and the potential warning time for missile attack can be near the instant of launch.

The Madre research radar has evolved over 11 years from a low-power, fixed-frequency device with a rudimentary crosscorrelation analysis feature (1-4) into a powerful, flexible tool for investigating radar signal-processing techniques and for studying a variety of radar illumination and target discrimination problems. The Madre radar's employment has diversified along with its evolution, and its initial direction toward investigating the feasibility of using coherent signal-processing methods to extract the low-amplitude echoes of over-the-horizon aircraft from a noisy environment has sprouted branches in many new directions, including radar-astronomical studies of the moon (5,6), studies of around-the-world radio propagation, high-altitude nuclear explosions (7,8), the characteristics of ground backscatter, high-frequency channel availability (9), and, most significantly, investigations of ionospheric radar's applicability to detecting ballistic missile launches. Despite this diversification, Madre's commitment to investigate long-range aircraft echoes has been preserved, and an extensive series of successful over-the-horizon aircraft-tracking experiments has been conducted (10-16).

The Madre research radar uses a 4.6-Mw-peak-power, 100-kw-average-power transmitter, capable of operating over a frequency band extending from 10 MHz to 27 MHz. An elevated corner-reflector antenna, rotatable in azimuth, is used for observing the Eastern Test Range. The center of this antenna is approximately 205 ft above the surrounding terrain, which is the effective reflecting surface at most azimuthal positions (including the direction of the Eastern Test Range), and is 315 ft above the surface of the Chesapeake Bay, which forms the reflecting surface for easterly propagation. This antenna consists of a pair of horizontal dipole elements placed in a 90- by 70-ft-aperture corner reflector. Figure 1 is a photograph of the rotatable antenna taken from the north with the camera pointing in the general direction of the Eastern Test Range. The reflecting surface at ground level is gently rolling, forested land. The broadside array to the left and below the rotatable antenna in Fig. 1 is used for studies of over-the-horizon aircraft and radar and radio astronomy experiments. Figure 2 is a plot of the estimated effective gain of the rotatable antenna over most of its operating band. The gain figures shown in Fig. 2 contain an estimated 5-dB enhancement above free-space gain, due to an

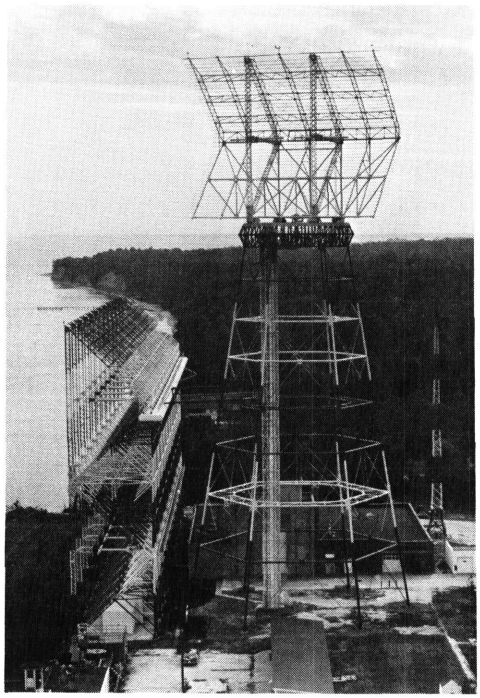

Fig. 1 - View from the north of the elevated rotatable antenna and the fixed broadside array (end view)

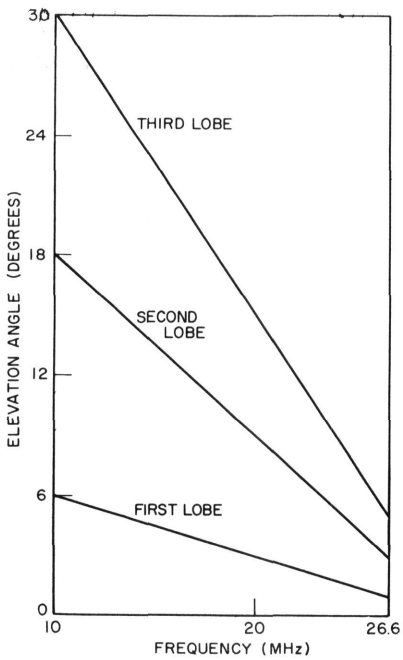

Fig. 3 - Lobe elevation vs center frequencies for the rotatable antenna

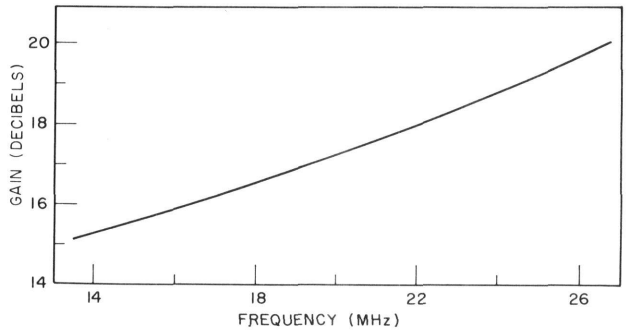

Fig. 2 - Estimated effective gain vs frequency for the rotatable antenna's principal lobe (including an assumed 5-dB ground enhancement)

assumed, imperfect ground-plane enhancement. Figure 3 shows the estimated elevation position versus frequency for the first three lobes of this antenna when it points in a direction in which the surrounding terrain serves as a reflecting surface; coverage from below 1-degree elevation to 30 degrees elevation is provided over the operating bandwidth. Figure 4 presents a measured elevation-plane pattern for the rotatable antenna near midband showing the excellent coverage at this frequency in the 2-degree to 7-degree elevation region. This region is important for F-layer transmission to the Eastern Test Range. This pattern, and similar data obtained at two frequencies near the lower and the upper extremes of Madre's operating bandwidth, was acquired with a specially instrumented KC-135 aircraft from Rome Air Development Center, which flew a series of pattern flights for NRL in the spring of 1966.

Figure 5 is a plot of the approximate half-power beamwidth in the azimuthal plane for this antenna over its operating bandwidth. Irregularities in the terrain to the south of the antenna probably cause its pattern to deviate somewhat from the estimated parameters in Figs. 2, 3, and 5.

During the six years in which the Madre research radar has been used in its high-power configuration, the wide variability of the propagation conditions which have been encountered and the disparate nature of the missile trajectories which have been studied have permitted a variety of propagation/illumination circumstances to be investigated. Indeed, there have been so many differences between the circumstances surrounding the launches, even of identical missiles

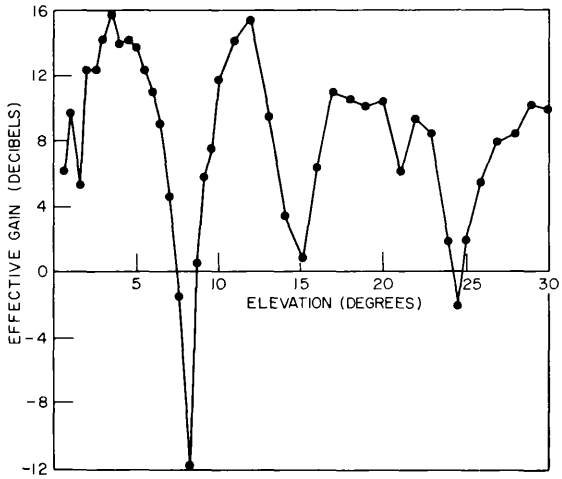

Fig. 4 - Measured elevation-plane pattern of the rotatable antenna at 15.6 MHz, with the antenna oriented in a southerly direction

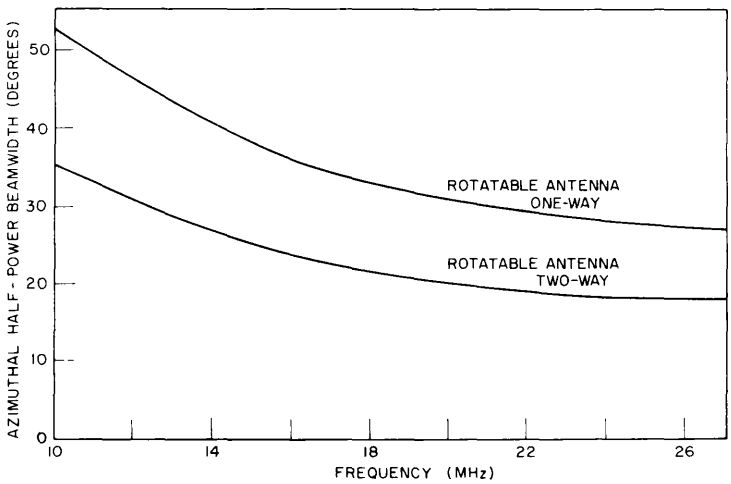

Fig. 5 - Azimuthal half-power beamwidth vs frequency for the rotatable antenna

along nearly identical trajectories, that only the grossest correlation has been possible between the results of these launches. The antenna parameters illustrated in Figs. 2 through 5 represent just a few of the many variables with which the true radar-echoing behavior of a missile is convolved in these data.

It is important for the reader to be familiar with the characteristics of the Madre signal processor in order that he may fully understand the results presented below.

The Madre radar is, basically, a coherent pulse-doppler radar in which the spectral integrity of the transmitted signal, and of the received signals, are preserved through all

mixing, filtering, and storage processes, permitting a coherent juxtaposition of all echo data received over a period as long as 20 sec.

The rotating magnetic drum and the scanning doppler filter which form the heart of the Madre signal processor were initially designed for extracting weak signals from remote, stable-velocity targets. A coherent integration time, or predetection filter bandwidth, was selected to exploit the expected doppler-frequency stability of constant-velocity target echoes received over an ionospheric path, and a 10-sec integration time (equivalent to 1/10-Hz filter bandwidth) was chosen.

In performing this 10-sec coherent integration, the rotating magnetic drum has stored upon it range-gated signal information in a bipolar video (or "undetected" video) format for a 20-sec period. This information is stored in a way that permits the accumulated signal information from all range gates to be read off the drum in a fraction of a second through an equivalent 1/10-Hz scanning doppler filter. For constant-velocity targets, which, for the purpose of this description, are defined as targets whose doppler-shifted radar echo remains within a single 1/10-Hz filter bandwidth for at least 20 sec, the total predetection signal-to-noise ratio enhancement achieved in this coherent integration can be as great as 33 dB, depending on the pulse-repetition frequency (prf).

Although the 10-sec coherent integration most fully exploits the 20-sec storage feature of the Madre drum for constant-velocity targets, an alternative 3-sec (or 1/3-Hz filter bandwidth) coherent-integration feature permits the study of targets whose velocities are less stable. When used with 20 sec of postdetection integration, and with a relatively high signal-to-noise ratio, this wider-band coherent-pulse-doppler processing can approach full exploitation of the Madre storage time. A 1-Hz filter is also provided for some types of signal processing, and this filter has been used for the investigation described in this report.

A second type of velocity-processing, independent of the Madre magnetic drum and its 20-sec storage feature, is provided by a Kay Electric Company Sonalyzer, which permits an effective 1/3-sec coherent integration (or 3-Hz bandwidth predetection filtering) to be performed on moving-target echoes. The analysis provided by this 3-Hz bandwidth filtering of received echo information is often useful in studying the short-period behavior of relatively large signals from rapidly accelerating targets.

A third type of signal analysis, and one which displays the dual attractions of (a) sensitivity to small echoes and narrow resolution bandwidth, plus (b) the ability to employ this sensitivity and resolution to rapidly accelerating targets, is provided by an acceleration-processing feature which has been developed as part of the Madre program. This feature permits at least a 3-sec coherent integration time to be retained, even for accelerating targets, by use of a series of shifting doppler filters whose center frequencies can be shifted with time to match the acceleration profiles of a wide variety of missiles (17-20). Refinements of each of these signal processing methods have permitted the amplitude spectra of received target echoes to be acquired for purposes of detailed analysis, and a study of the amplitude spectra for selected missile targets is planned as a later part of the study presented in this report.

An additional feature of the Madre research radar, which is instrumental in permitting the achievement of its high sensitivity, is the provision for removing the overwhelmingly large ground clutter (or ground-backscatter) return which seriously impairs the effectiveness of noncoherent ionospheric radars. A series of crystal comb rejection filters attenuates, by 70 to 80 dB, the large clutter signal (whose spectrum is normally concentrated within one or two Hz of the center frequency and prf-associated harmonics)

without degrading moving-target echoes whose doppler shifts do not fall within the rejection notches. These filters are described thoroughly in Ref. 21, and one illustration of their value appears in Ref. 15.

The relative performance of the Madre system in each of these configurations may be assessed with the aid of a figure of merit related to the radar equation:

$$\left(\frac{P_r}{P_N}\right) = \frac{\overline{P}_t G_t G_r T_f \lambda^2}{(4\pi)^3 R^4 p_n L} \sigma ,$$

where

$\left(\frac{P_r}{P_N}\right)$ denotes the average signal-to-noise power ratio at the output of the radar signal processor, after all bandwidth-narrowing operations have been performed,

$\overline{P}_t$ denotes the average transmitted power in watts,

G_t denotes the total effective gain of the transmitting antenna expressed as a power ratio,

G_r denotes the total effective gain of the receiving antenna expressed as a power ratio,

T_f denotes the coherent integration time in seconds, equivalent to the reciprocal of the final predetection filter bandwidth,

λ represents the transmitted wavelength in meters,

R denotes the target range in meters,

p_n denotes the received noise power in watts per Hz,

L represents miscellaneous losses in the transmission lines and in the interfaces, and (most significantly) in the propagation medium, expressed as a power ratio greater than unity, and

σ denotes the target's radar cross section in square meters.

Over the 13.5-MHz to 27.0-MHz frequency band in which the observations which follow have been made, the peak effective gain of the single antenna used for transmitting and for receiving varies from approximately 15 dB to approximately 20 dB. The average power transmitted is normally 100 kW. An estimate of the average noise power must include the effects of (a) atmospheric and galactic noise, for which a gross estimate of one microvolt per meter noise-field strength per 10-kHz bandwidth may be taken (equivalent to -160-dBW noise power per Hz for the Madre antenna aperture), plus (b) the less easily quantized effects of man-made noise and cochannel interference. Several years of operation of the Madre radar in a very noisy, crowded radio-frequency environment have enabled the operators to develop a rule-of-thumb in estimating noise power content. This rule, which is taken here as the best available estimate of the artificial noise contribution to the total noise power under Madre's normal operating conditions, is that the true total noise power in a nominally empty channel nearly always will exceed the estimated atmospheric/galactic noise power by 10 dB. For the purposes of this approximate performance assessment, then, a noise power of -150 dBW per Hz will be assumed. The range parameter will be taken equal to the range to the Eastern Test Range launch complex, 650 naut mi from the Madre radar site. Miscellaneous losses can only be estimated,

and all such losses will be neglected here except for D-layer absorption. Table 1 lists the expected nondeviative path absorption (in dB) for various times of the day, seasons of the year, and sunspot number (SSN), with the propagation in each case assumed to be at or slightly below the maximum usable frequency (MUF). The loss figures for summer, winter, and the equinoxes are placed into three subgroups corresponding to sunspot numbers of 10, 50, and 100 for local mean time (LMT) at 2-hr intervals between 0800 and 1800 LMT. A letter indicating whether E-layer, F-layer, or E/F propagation is the predicted propagation mode for that listing appears with each loss figure. Single-hop propagation is appropriate in all cases.

Table 1
Estimated Nondeviative Absorption Values for Typical Operating Conditions of the Madre Research Radar

Local Mean Time (LMT)	Sunspot Number (SSN)	Absorption (dB) and Ionospheric Layer in Use		
		Summer	Winter	Equinox
0800	10	2F	2F	2F
1000	10	3F	3F	4F
1200	10	12F	3F	5F
1400	10	18E/F	7F	15F/F
1600	10	24E	11F	21E
1800	10	24E	11F	15E
0800	50	2F	2F	2F
1000	50	2F	2F	2F
1200	50	12E/F	3F	6F
1400	50	20E	6F	12F
1600	50	24E	9F	14F
1800	50	25E	9F	9F
0800	100	2F	2F	2F
1000	100	3F	2F	2F
1200	100	9F	2F	4F
1400	100	16E/F	5F	8F
1600	100	21E	6F	11F
1800	100	21E	8F	11F

These data were extracted from a series of predictions performed for NRL by the Environmental Science Services Administration using their empirical prediction routines for ionospheric propagation.

For the various types of analysis represented in the analyses to follow, the coherent integration time T_f varies between 1 sec and 10 sec (for the Madre signal processor with fully effective coherent integration — this circumstance is probably approached for missile-launch operations only when acceleration processing is used, and even then only when careful attention is devoted to matching the shifting-filter profile to a known missile acceleration profile from post-flight range instrumentation data). If a nominal 10-dB-average signal-to-noise level is required for a low false-alarm rate combined with a relatively high probability of detection, the minimum effective radar cross sections for which Madre may be expected to yield useful data range between extremes of 3×10^5 m^2 (for the worst propagation case considered: summer evening E-layer propagation combined with the least sensitive analysis bandwidth of 1 Hz and the lowest antenna gain of

15 dB indicated on Fig. 2) and 72 m^2 (for one of the lowest (2 dB) nondeviative absorption cases listed in Table 1, combined with the most sensitive analysis system bandwidth of 1/10 Hz and the highest antenna gain of 20 dB in Fig. 2). More than fifty percent of Madre operations have been run at a frequency of from 15 to 16 MHz, however, and normal operations involve using the medium-sensitivity, 1/3-Hz bandwidth predetection filter. Furthermore, the probability distribution of expected nondeviative path absorption, shown in Fig. 6 (extracted from Table 1), indicates that during more than fifty percent of the usual operating day these losses can be expected to be 6 dB or less. Using these criteria as gross indications of normal operation, the minimum effective radar cross section for which the Madre radar may normally be expected to yield useful information is approximately 960 m^2.

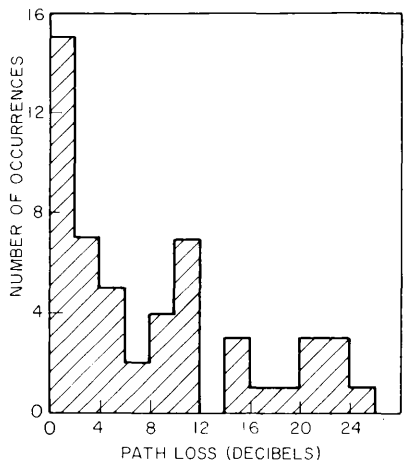

Fig. 6 - Probability distribution of the expected nondeviative path absorption

Finally, Table 2 lists the important parameters of the Madre radar as it has been used in studies of ballistic missile launches from the Eastern Test Range.

Table 2
Performance Parameters of the Madre Radar

Parameter	Magnitude or Range of Parameter
Frequency Band	13.5 MHz to 27.0 MHz
Average Power	100 kW
Peak Power	4.6 MW
Antenna Gain (including estimated 5-dB imperfect ground enhancement)	15 dB to 20 dB
Pulse Length (at -20-dB points)	250 μsec to 800 μsec
Pulse Repetition Frequencies	45, 60, 90, and 180 pps
Automatic On-Line Coherent Integration:	
Storage Time	10 sec
Predetection Filter Bandwidths	1, 1/3, or 1/10 Hz
Off-Line (Sonalyzer) analysis predetection filter bandwidth	3 Hz

Purpose of this Report

The objective of the related investigations described in this report is to apply diagnostic ionospheric propagation techniques, such as computer-assisted ray tracing, to an understanding of the influence of ionospheric phenomena on over-the-horizon radar. In the present stage of these investigations a digital-computer ray tracing program has been developed which enables the user to perform analyses of the radar signal data due to moving targets at single-hop range from the radar site. For this report the program has been used to analyze radar data from several submarine-launched Polaris A2 and A3 ballistic missiles (SLBM) launched on the Eastern Test Range from Cape Kennedy, Florida.

The coherent pulse-doppler feature of the radar signal processor permits a direct measurement of the vehicle doppler shift, or velocity, and the spectral dispersion of the radar signal permits analyzing the character of the target as a reflector, in combination with the effects of turbulence in the intervening medium. The use of ionospheric soundings from points along the radar propagation path allows a model of the electron density to be constructed from which propagation paths (or rays) may be calculated between the radar and two regions of interest: (a) the region of the earth from which ground backscatter emanates, and (b) the position of the vehicle as it moves along its trajectory. This ray trace may be used in conjunction with the *observed* ground backscatter to refine the ionospheric electron-density model utilized and to adjust the predicted or simulated received signal amplitude with respect to path absorption. With these preliminary "controls" achieved, the simulated propagation path may be used with received radar data from the vehicle itself to analyze the target signature. It is hoped that, ultimately, this technique will be developed to a degree in which the variation of a target's echoing cross section and the behavior of its echo spectrum can be used to deduce the effects of the vehicle on its environment from their manifestations on ionospheric radar signals. A subsidiary objective of this program, albeit one which is probably of greater ultimate importance, is the study of the ground backscatter echo itself. It is hoped that the ionospheric propagation analysis techniques pursued in this study can be used to determine the behavior of various types of terrain as scatterers of electromagnetic energy in the shallow-incidence regime, which is difficult to investigate in a line-of-sight geometry due to the uncertainties introduced by practical antenna parameters. It is hoped also that the study of ground backscatter with these techniques can be helpful in refining the empirical models of nondeviative absorption which are at present in a rudimentary stage of development. Finally, it is proposed to use these ray-tracing analysis techniques to determine the extent to which ground-backscatter information may be used as a diagnostic device for assessing over-the-horizon-radar target-area illumination and for high-frequency broadcast area coverage.

A detailed description of the digital computer ray-tracing program appears in Appendix A, and a subroutine which uses this program for the synthesis of ground-backscatter profiles is described in Appendix B. The program is constructed to make direct use of vertical ionospheric soundings or of true-height profiles which may be determined from the soundings, to synthesize a spherically symmetric ionospheric layer structure. Rays are calculated on the basis of a simple Snell's law treatment in a spherically stratified medium of varying index of refraction, exclusive of the effects of the geomagnetic field. The stratification is at present arbitrarily constrained to yield strata with a constant thickness of 1 km, although a provision is included for permitting the stratum-thickness to vary to increase the precision of the refraction treatment in regions where the electron density changes rapidly with height. Simple reflection of each ray about a vertical axis through the path midpoint is used for the downward portion of its trajectory. Rays may be calculated for any elevation separation, although a separation of 0.05 to 1.0 degree is used for most calculations. For calculating path absorption,

ground and target illumination, and received signal amplitude from both ground backscatter and targets, the variation of antenna gain with azimuth and elevation is inserted into the program. For ground-backscatter calculations, an integration is performed over the azimuthal pattern, whereas, for target-echo amplitude calculations, antenna gain in only the target direction is used. For display purposes the spacing of ray trajectory lines is weighted on the ray plot in inverse proportion to the total relative power density radiated and received in the appropriate direction by the antenna. For cases in which ground backscatter alone is treated, this display represents a vertical cut of the propagation geometry taken in the plane of the antenna beam center. For cases in which a missile launch is treated (all the examples in this report are in this class), the display represents a collapsed ensemble, presented in a single plane, of ray paths computed in a fan-shaped series of vertical planes which contain the radar site and the missile position at different points along its trajectory. Figure 7 is a perspective drawing of three such radar site-missile position planes. The three ray trajectories in Fig. 7 would appear undistorted on a ray plot at their appropriate elevation positions, and the points P_1, P_2, and P_3 would be joined on this presentation in a much distorted facsimile of the missile trajectory; this facsimile would be faithful only in showing the correct vehicle position along each ray path.

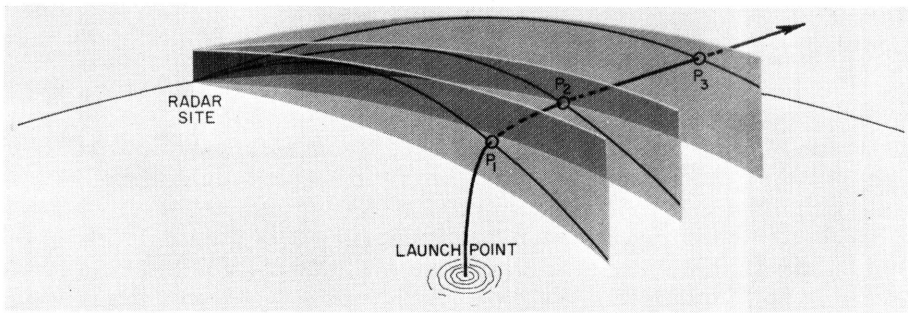

Fig. 7 - Perspective view of three adjacent vertical planes upon which ray trajectories are shown emanating from the radar site and intersecting the missile trajectory

In calculating the ground-backscatter amplitude which is expected from a selected ionospheric model, a full set of ray trajectories from the radar site to the illuminated region of the earth at one-hop distance is calculated. Path absorption is calculated on the basis of an empirical formula determined by Lucas and Hayden (22). A scattering model is used in which the proportion of power available for diffuse scattering is determined arbitrarily (and a provision is made for an iterative procedure by which this proportion may be adjusted to fit the actual amplitude of the received ground-backscatter echo). A dependence of diffuse scattering amplitude versus elevation angle is also assumed (with a provision for subsequent adjustment to fit the measured ground-backscatter variation in time delay). Rays then are repropagated *from* incremental areas of the illuminated region, using the same propagation geometry from each area as was used for the initial ray *to* the illuminated region, and the contributions along all possible paths to the site from all incremental areas in the illuminated region are summed and displayed versus the path time-delay, on an amplitude-versus-time-delay presentation. Examples of this presentation are given in the second part of this report, in comparison with the received ground-backscatter signals.

The propagation analysis is also used to determine the predicted doppler shift and the range to a target having known trajectory in the illuminated region. Doppler shift is calculated on the basis of the rate of change of the phase path, and is presented versus time after launch in a graphical display. Examples of this presentation are given in the second part of this report, in comparison with actual radar data in a similar format.

The second part of this report contains analyses of several Polaris A2 and A3 launches on the Eastern Test Range obtained by applying the techniques described above. The principal effort in these analyses has been to determine the efficacy of the ionospheric propagation simulation in predicting: (a) the illumination of the single-hop region from which the launches took place, (b) the onset and the loss time of target signatures, (c) the doppler shift of target echoes, and (d) the intermittency of target echoes, as caused by antenna parameters and propagation constraints. These analyses are not presented as an exhaustive treatment of Polaris missile signature characteristics. They represent the results of one stage of a continuously evolving program in ionospheric propagation analysis, and should be expected to be augmented by additional signal information and to be refined themselves as this program continues to develop.

COMPUTER-AIDED ANALYSIS OF OVER-THE-HORIZON SLBM SIGNATURES

The digital computer ray-tracing analysis described in the introduction has been employed to study the over-the-horizon radar signatures from numerous Polaris A2 and A3 missiles launched on the Eastern Test Range between 1961 and the present. Several such missile-launch signatures are analyzed below, and this analysis may best be introduced through an illustrated example. Eastern Test Range launch 2955, of May 25, 1964, is a convenient vehicle for this introduction. The circumstances of the launch and the radar illumination are summarized in Table 3. Figure 8 is a photograph of the earth echo acquired on the Madre radar receiver with 4.6-MW peak power and 100-kW average power illumination at 15.595 MHz. This photograph is a display of the received echo amplitude versus the time delay, and was taken at the first-receiver intermediate-frequency (500-kHz) stage with no bandwidth-narrowing or detection. A time exposure of several seconds was made to smooth out the typical 2- to 3-sec fading period of earth backscatter, and hence to eliminate as nearly as possible the sampling effect of this type of presentation. A sequence of calibration pulses of approximately 500-μV amplitude appears on this photograph, with a spacing of approximately 5.5 msec.

Table 3
Data for Eastern Test Range Launch 2955

Missile Type	Launch Time (EST)	Radar Frequency (MHz)	PRF (pps)	Pulse Length (at -20 dB points) (μsec)	Average Power (kw)	Illumination Modes
Polaris A3	1415:03	15.595	90	700	100	E and F Layers

The illumination represented in Fig. 8 results from a combination of E- and F-layer propagation to the target region, with the near-range echoes attributed to E-layer illumination and the intermediate and far-range echoes attributed to F-layer illumination.

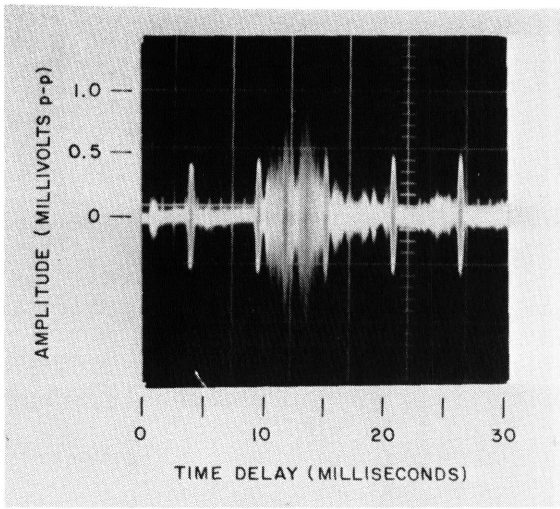

Fig. 8 - Observed ground-backscatter distribution, 1425 EST, May 25, 1964 ETR launch 2955

The ionospheric electron-density profile which has been used for the computer simulation was scaled from ionospheric sounding data acquired at the time of the launch from ionosondes at Grand Bahama Island and Fort Belvoir, Virginia. These locations are near the extremes of the propagation path used for coverage of missile-launch trajectories, and the ionospheric data from them or other similarly located stations normally are used as the basis for an interpolative estimate of electron density versus height. This interpolated result is then assumed to hold throughout the ionosphere between the radar site and the propagation path terminus, and from it is acquired a spherically stratified layer structure from which ray paths are calculated. This one-dimensional approach is presently being supplanted by a two-dimensional treatment which is, however, still incomplete. Figure 9 is a ray plot based upon this model. In Fig. 9 the peaks and nulls of the antenna pattern are represented by compression and rarefaction of the rays' separation in elevation, as described above. All dimensions appear in kilometers, with the vertical scale expanded relative to that along the earth's surface by a factor of

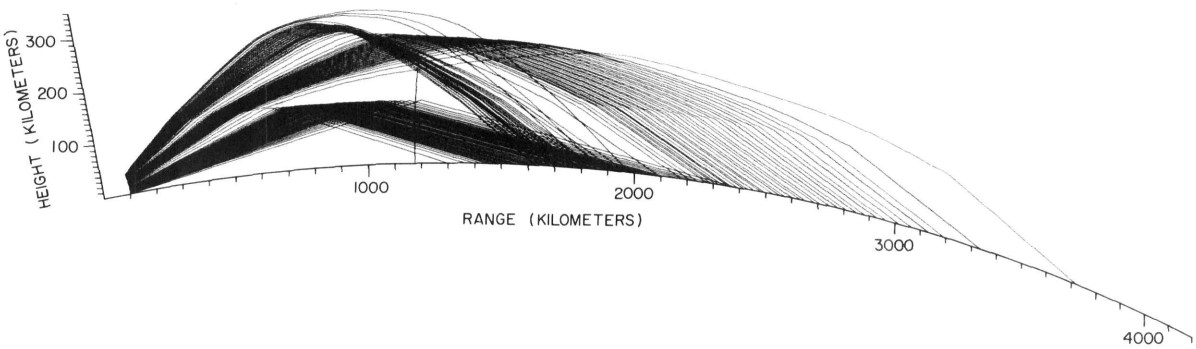

Fig. 9 - Ionospheric ray plot for ETR launch 2955

two. This distortion is introduced simply to permit more detailed examination of the ray trace, especially in regions where ray focusing is indicated. The missile trajectory is plotted on this ray plot as a curved line originating at approximately 1170 km range, the range of the launch point from the radar site. The abrupt termination of the missile trajectory at about 190 km altitude occurs simply because this altitude is the highest one for which range tracking data were available.

A limited amount of E-layer propagation at the lower takeoff angles is evidenced by the relatively sharp reflection of the entire first antenna lobe at an altitude of approximately 110 km. Even the second-lobe ray paths are deviated substantially in this region, both in their ascending and descending legs. This E-layer blanketing, in combination with the position of the first antenna-pattern null, gives rise to a rather large void in coverage of the missile trajectory between 110-km and 160-km altitude. From 160 km to approximately 240 km, coverage is reestablished and can be seen to arise from contributions due to both second-lobe and third-lobe radiation. It might be expected that the missile signature acquired in this upper-altitude region would be complex in doppler shift and amplitude behavior, due both to the multiplicity of the propagation paths to the target and to the focused character of the rays in some regions.

This ray trace has been used as the basis for describing a simulated ground-backscatter power distribution, which appears in Fig. 10 in terms of received amplitude versus time delay. The amplitude scale in this illustration, as on all simulated ground-backscatter profiles to follow, is an arbitrary linear scale. This circumstance reflects an uncertainty in the true amplitude, which is due to the present imperfect state of the computer program. Current efforts are, in part, directed toward resolving this uncertainty. The principal features of this illustration, in comparison with the actual measured values in Fig. 8, are that (a) it correctly predicts the nearest delay time at which ground-backscatter energy is received and the farthest delay time at which first-hop ground backscatter is received, and (b) it correctly predicts the position in time delay of the second (F-layer) amplitude peak of the ground-backscatter echo. Its inability to predict the amplitude of the first (E-layer) ground-backscatter echo peak correctly is not necessarily indicative of a deficiency of the ray-tracing technique. The large E-layer echo which was measured could well have arisen from a localized patch of sporadic E-layer ionization (E_s) which was not indicated on the ionograms. In fact, both the season and the time of day when this measurement was made (late spring, midday) are notorious for the prevalence of E_s ionization.

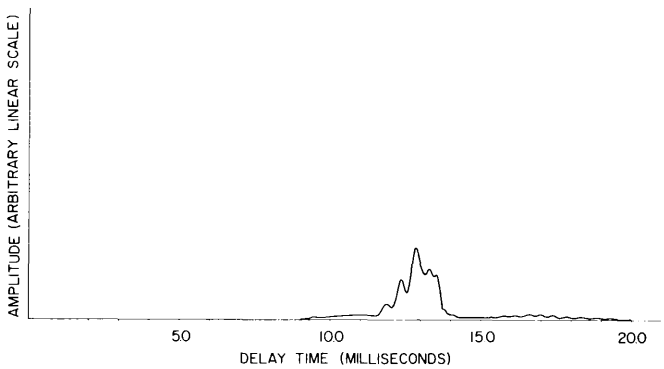

Fig. 10 - Predicted ground-backscatter distribution for ETR launch 2955

The simulated ground-backscatter distribution in Fig. 10 should be viewed simply as a first iteration. A simple, isotropic dependence of backscattering coefficient upon radiation takeoff angle was used, with no attempt to adjust this coefficient to more nearly match the measured distribution. The amplitude of the simulated backscatter echo cannot be compared in an absolute sense with the measured amplitude (and hence only a relative amplitude scale is indicated), because no attempt has been made here to determine what proportion of the electromagnetic energy which strikes the earth is available for diffuse scattering (and hence may contribute to the ground-backscatter echo). This problem is a part of NRL's planned continuing effort in the analysis of ground backscatter.

Figure 11 contains a computer-plotted simulation of the doppler shift which would be expected of a radar echo from the missile at all points on the trajectory in Fig. 9 which are illuminated by radar rays. The discontinuous character of Fig. 11, particularly in the interval between 45 sec and 100 sec (all times indicated are times relative to range zero, or launch time), is due in part to the sampled character of the ray trace and also, in part, to the limited accuracy of the computer operations. In some cases, similar discontinuous behavior can in fact be related to the existence of a multiplicity of ray paths which strike the missile at different aspect angles, or to actual sudden changes in the missile's motion; in the present case, neither condition exists. The void in coverage between 110-km and 160-km altitude is represented by the absence of data between 122 sec and 142 sec in Fig. 11. The nearly vertical lines which characterize the doppler shift behavior versus time at 120 sec and 142 to 144 sec in Fig. 11 result from true, rapid acceleration of the vehicle in these regions. One additional point is of concern in viewing Fig. 11 and all subsequent doppler-versus-time presentations: the Madre radar, like all pulse-doppler devices, is limited in unambiguous doppler sensitivity by its

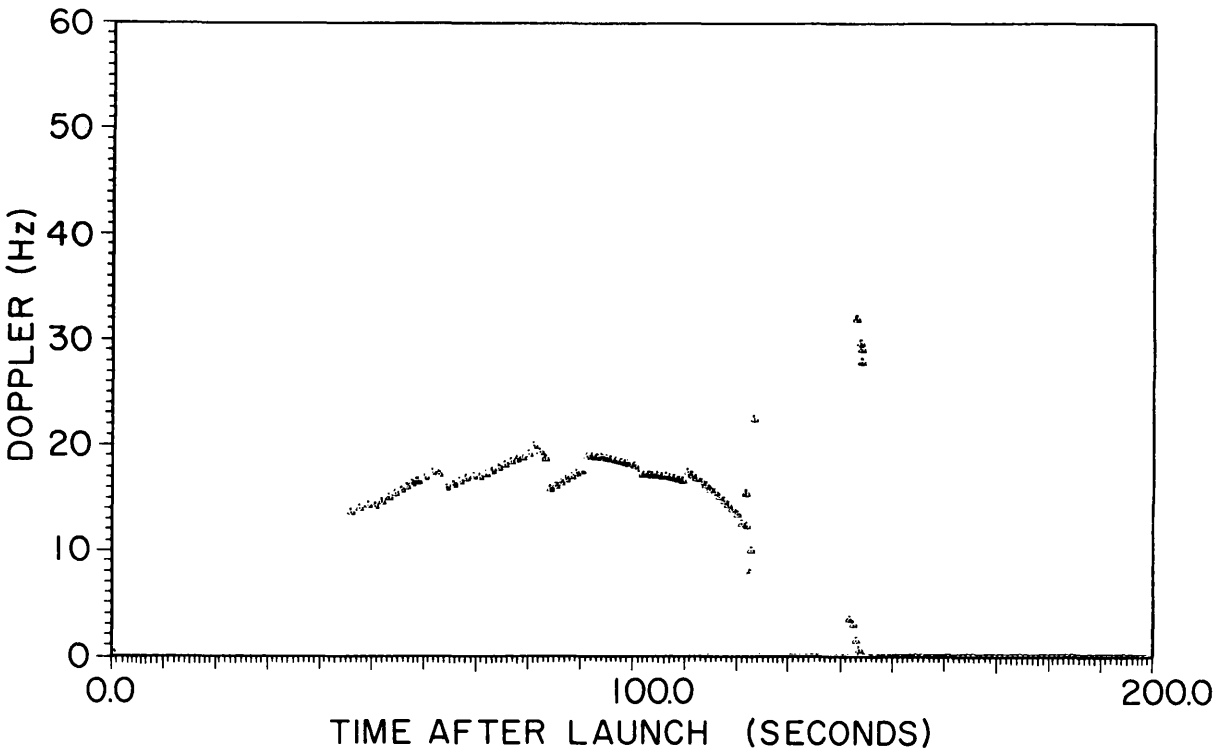

Fig. 11 - Simulated signature for ETR launch 2955

pulse-repetition frequency (prf). For the 90 pulse-per-second (pps) rate which was used during this launch, the available unambiguous doppler interval extends from 0 to 45 Hz; all data below zero (i.e., all negative doppler shifts, or receding targets) are "reflected" into this interval, as are all data for the several continuous 45-Hz intervals through which an accelerating missile's doppler shift passes. The nearly vertical lines actually represent (in the 120- to 122-sec region) an acceleration from +13 Hz to -75 Hz, and (in the 141- to 144-sec region) reflections via a multiplicity of paths which yield both an *approaching* doppler shift (+28 to +32 Hz) and a *receding* doppler shift (-89 to -94 Hz). The fact that both approaching and receding components are possible in the latter time interval is readily apparent from the ray geometry near the end of the trajectory line plotted in Fig. 9.

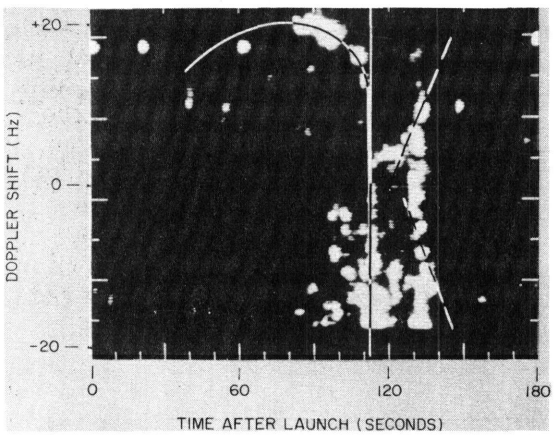

Fig. 12 - Observed signature fir ETR launch 2955

Figure 12 is a photograph of the doppler shift versus time-after-launch measured with the Madre radar during the Polaris launch whose simulated signature appears in Fig. 11. The reader should be cautioned in interpreting this illustration that its format is not identical to that in Fig. 11, because the doppler-shift data are projected (or reflected) here not into the 0- to 45-Hz frequency interval, but into the -22.5- to +22.5-Hz frequency interval. For convenience in effecting a comparison between Figs. 11 and 12, the doppler-shift data from the former are overlaid on the latter in the appropriate format. In this illustration, as on others below, the overlaid lines are drawn in white where the background is dark, and in black where the background is light. Some care must be taken in distinguishing the color changes along these lines from true *dashed* lines, which also appear in some figures. The line segments indicated by the few points near 140 to 144 sec in Fig. 11 are supplemented in Fig. 12 by dashed-line continuations in both directions, included to indicate their approximate slopes. Also included in Fig. 12, at a doppler shift of approximately +17 Hz, is a row of blobs at 0, 20, 60, and 180 sec after launch. These blobs are simply timing marks.

One circumstance of the signal processor's characteristics, which manifest themselves upon all output data, is also of concern. The filter network which provides these data is not capable of passing signals below an *effective* doppler frequency of 5 Hz. This characteristic is imposed upon the lowest 5 Hz of the doppler-frequency-versus-time presentation; hence, in the present case, no information between doppler shifts of -17.5 and -22.5 Hz is displayed — the display is simply blank in this interval. In the more common 0- to 45-Hz format, of which some examples appear below, all information between 0 and 5 Hz will be similarly suppressed.

One final remark is pertinent to the circumstances of the comparison between the simulated doppler-versus-time behavior and the observed behavior in Fig. 12. The uncertainty in the actual launch time (up to 1 sec possible error) plus whatever operator error may occur in the placement of the timing marks, when added to the effects of possible motions in the ionospheric reflection region (which would be undetectable to the radar),

combine to prevent a precise placement of the simulated doppler-versus-time display on the measured version. Approximately 3 sec leeway from the nominal launch time has been used (but no doppler-shift deviation) in view of these uncertainties, to permit a striking, complementary orientation of the two plots. The signature onset at approximately 80 sec, its subsequent downward curvature and steep decline, the brief absence of signature between 120 and 130 sec, and the ultimate reappearance of the signal all agree extremely well with the simulated version. The two dashed lines may even be seen, with only a small exercise of imagination, to correspond to parts of the later signature behavior. The observed signature also seems to terminate approximately at the same time as the simulation. This circumstance reflects the frequent tendency of signals to cease at missile burnout, the time when instrumentation data from which the simulation is constructed also cease.

A second, similar example of the comparison of computer-simulated ground backscatter and SLBM signature data with the measured versions acquired using the Madre radar is afforded by Eastern Test Range launch 2903, also of May 25, 1964. Launch and illumination data are contained in Table 4.

Table 4
Data for Eastern Test Range Launch 2903

Missile Type	Launch Time (EST)	Radar Frequency (MHz)	PRF (pps)	Pulse Length (at -20 dB points) (μsec)	Average Power (kw)	Illumination Modes
Polaris A3	1329:05	15.595	90	700	100	E and F Layers

This case is of particular interest in that the 46-min period which elapsed between this launch and ETR launch 2955, which followed it, was adequate for small changes to occur in the locations of the illumination amplitude peaks and nulls, but brief enough that wholesale movement of the illuminated region, such as might stem from diurnal ionospheric effects, did not occur. Figure 13 is a photograph of the earth echo which was made slightly after this first launch, but more than a half-hour before the second launch. Comparison between Figs. 8 and 13 shows that although small shifts in the fine structure can be discerned readily, the overall amplitude and general location of the ground backscatter echo along the time base are not substantially different. A small amount of growth in the F-layer echo, which appears in Fig. 8 between 15 and 20 msec time delay, can be seen to have occurred; hence, it may be expected that ETR launch 2903, the earlier launch, will have yielded a less extensive F-layer signature than the later launch. This expectation is confirmed by the data presented below.

Figure 14 is the computer-derived ray plot, determined from ionospheric sounding data acquired near the extremes of the propagation path. In comparison with Fig. 9, the ray plot pertinent to ETR launch 2955, it is clear that the F layer in the present case is indeed capable of less refraction. None of the third-lobe contribution and very little of the second-lobe contribution, which were rather intense in Fig. 9, can be found in Fig. 14. The F layer provides some illumination of the missile trajectory in the 200-km altitude region, but it should be noted that this illumination is quite sparse in comparison to that indicated by Fig. 9. Figure 15 is the simulated ground backscatter distribution for the present example, exhibiting an unusually peaked character. This illustration does

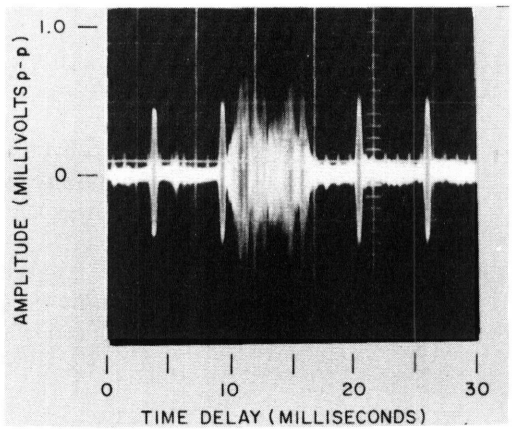

Fig. 13 - Observed ground-backscatter distribution, 1340 EST, May 25, 1964, ETR launch 2903

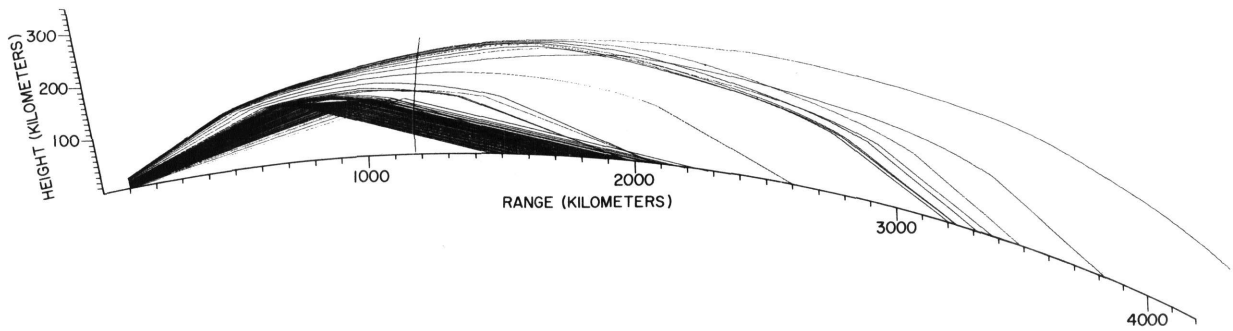

Fig. 14 - Ionospheric ray plot for ETR launch 2903

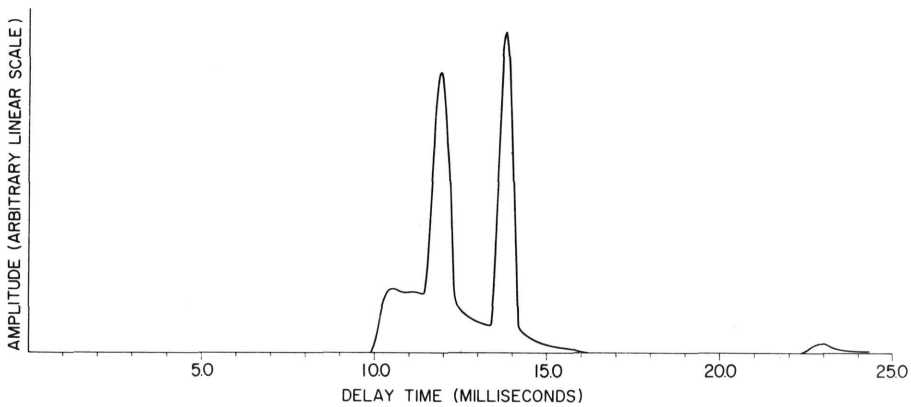

Fig. 15 - Predicted ground-backscatter distribution for ETR launch 2903

accurately predict the general location in time delay of the ground-backscatter echo and properly reflects, by its peaked character, the comparatively peaked behavior of the observed version in Fig. 13 relative to that in Fig. 8. The positions of the two peaks in this simulated version correspond roughly with the first and last peaks on the corresponding observed ground-backscatter profile. The small peak at 23-msec time delay cannot be discerned in the observed echo of Fig. 13 and corresponds to weak F-layer illumination which may yield an echo below the noise level.

A direct comparison of Figs. 10 and 15 should not be attempted; the vertical scale of the latter is exaggerated by a factor of 10 in comparison with the former, and, actually, the peak amplitude predicted in Fig. 10 is twice that in Fig. 15. Figure 16 contains the simulated target signature for ETR launch 2903. This graph indicates a more extensive F-layer contribution than does Fig. 11, but it should be remembered that little energy was actually contained in the illumination which provided this component.

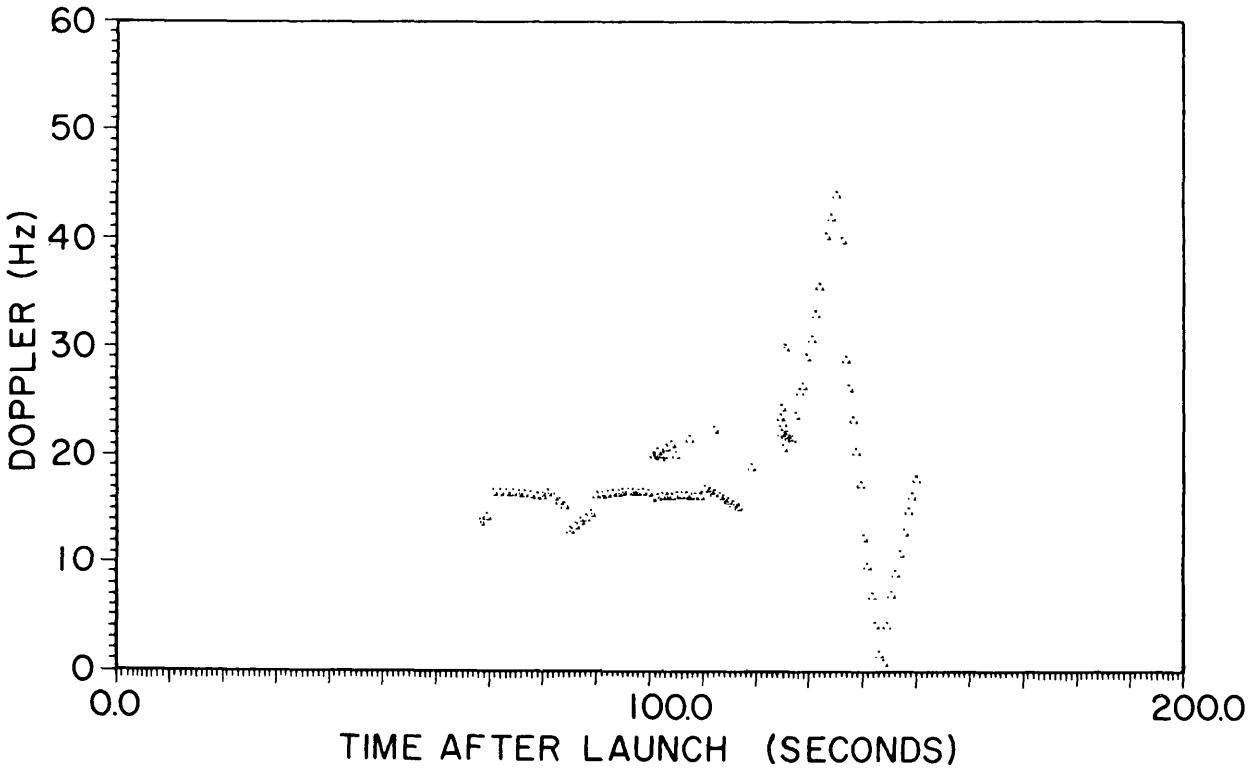

Fig. 16 - Simulated signature for ETR launch 2903

Comparison of the simulated ray plots (Figs. 9 and 14) illustrates the relatively less intense *predicted* F-layer illumination of the vehicle in the present case, and comparison of the observed ground-backscatter echoes (Figs. 8 and 13) for the two cases indicates that these predictions were indeed realized. The F-layer contribution in Fig. 16 must be viewed as resulting from extremely weak illumination and cannot be expected to appear in the measured version. Figure 17 shows observed missile signature for ETR launch 2903 and appears in the normal, 0- to 45-Hz doppler-shift format. The simulated signature behavior from Fig. 16 is superimposed on Fig. 17. Actual acquisition of the

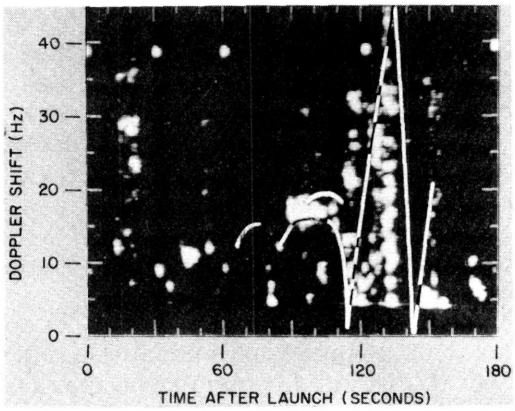

Fig. 17 - Observed signature for ETR launch 2903

target echo lagged the predicted acquisition by 20 sec. This time (T_0 + 90 sec) corresponds to the time at which the vehicle traversed the area in Fig. 14, where a pronounced focusing effect is apparent in the density of the rays.

This focusing effect is illustrated in Fig. 15 by the high-amplitude peaks at 12 and 14 msec time delay, whose double character arises from the multiplicity of paths which contribute to that same closely bunched bundle of rays. The observed signature falls precisely amidst the predicted doppler shifts of the two contributions and is not shifted by any detectable amount from the predicted doppler-shift values. No substantial void in illumination coverage is predicted in this case, in contrast to that of ETR launch 2955 (Fig. 9), where a large illumination vacuum was predicted immediately above the E layer. Correspondingly, there appears to be an echo represented in Fig. 17 throughout the period from 90 to 136 sec after launch, which follows roughly along the upward leg of the predicted doppler-shift curve. The echo seems to have been lost approximately 136 sec after launch, as the vehicle entered the sparsely illuminated region above the E layer. It is interesting that, in this case, the signature loss was definitely due to a cessation of illumination — burnout occurred at 144 sec. The few traces which parallel the predicted line near 150 sec after launch *could* represent the vehicle's entry into the more heavily illuminated region at about 180 km altitude; however, the authors do not attempt to claim these traces as confirmed missile echoes. That this echo seemed to disappear at a slightly earlier point than the previous one, and certainly was less intense than the previous one in the interval where the vehicle was F-layer illuminated, is interpreted as evidence for the success of the ray-tracing technique in treating even a rather diffuse, changing F layer.

A third example of the computer simulation compared with actually measured ground backscatter and SLBM signature data is the treatment of ETR launch 3670, of July 30, 1964. The pertinent launch and illumination data are summarized in Table 5. Figure 18 is a photograph of the ground-backscatter echo, taken as a time exposure over several seconds, somewhat earlier than the launch period. Conditions were relatively unchanged at the actual launch time, however, from those illustrated. Figure 18 indicates a rather

Table 5
Data for Eastern Test Range Launch 3670

Missile Type	Launch Time (EST)	Radar Frequency (MHz)	PRF (pps)	Pulse Length (at -20 dB points) (μsec)	Average Power (kw)	Illumination Modes
Polaris A3	1130:03	18.036	90	700	100	E and F Layers

dense E layer, as is expected near midday in July, with a contribution to the ground backscatter echo which occurs between 10 and 15-msec time delay. The weaker F-layer contribution is evident in Fig. 18 between 18 msec and the end of the trace at 25 msec time delay.

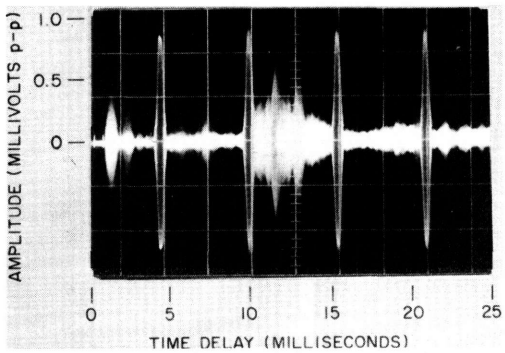

Fig. 18 - Observed ground-backscatter distribution, 1050 EST, July 30, 1964, ETR launch 3670

The simulation for this case was made from ionograms acquired near the launch site and at Ft. Belvoir, Virgnia. However, a complication which arose in this treatment required that the F-layer and E-layer contributions be treated separately. This necessity stemmed from the circumstance that the same elevation-angle interval (i.e., the same antenna lobe) was required to provide both contributions, and hence that the F-layer contribution actually was a result of energy which (a) penetrated the E layer in the same region from which some of the energy was reflected, (b) continued upward to the F layer where it was itself reflected, (c) continued to the earth, was scattered, and (d) returned to the receiver. The ray-tracing routine does not allow reflection and transmission of energy at the same layer, and predicted initially that *all* energy would be reflected at the E layer. The F-layer contribution was acquired only by rerunning the routine with a slightly less dense and more nearly normal E layer. Figure 19a is a ray plot of the E-layer contribution, and Fig. 19b is a ray plot of the F-layer contribution, as determined by the ray-tracing routine. If these two plots are superimposed, it is evident that continuous coverage of the missile trajectory is effected from approximately 25 to 120 km altitude via the E layer, and from 120-km altitude to 150 km via the F layer.

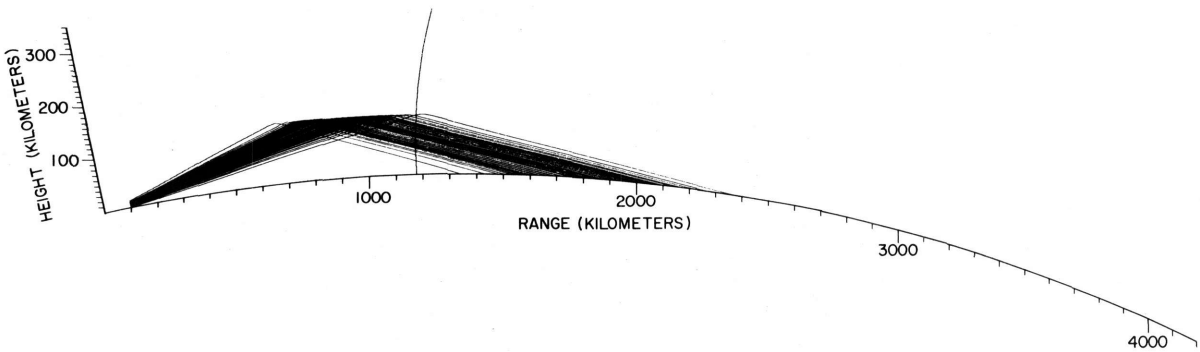

Fig. 19a - Ionospheric ray plot for ETR launch 3670, E-layer propagation

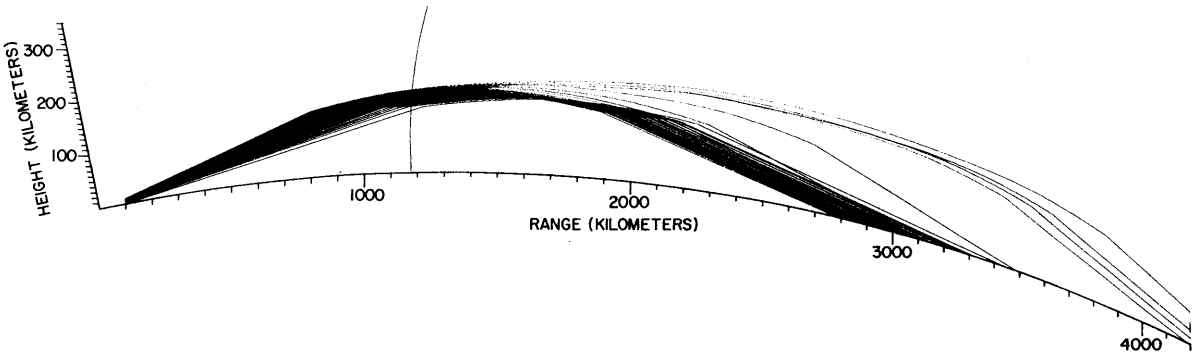

Fig. 19b - Ionospheric ray plot for ETR launch 3670, F-layer propagation

Figure 20 is a graph of the predicted ground-backscatter profile with both contributions superimposed. Comparison of the graph of Fig. 20 with the actual measured ground-backscatter profile in Fig. 18 illustrates the substantial success which the ray-tracing approach can have in predicting ground-backscatter profiles. The two versions display close agreement in (a) the time-delay interval and the general amplitude behavior of the E-layer contribution, (b) the separation in time delay of the two contributions, (c) the time-delay interval of the F-layer contribution, and (d) the relative amplitudes of the two contributions.

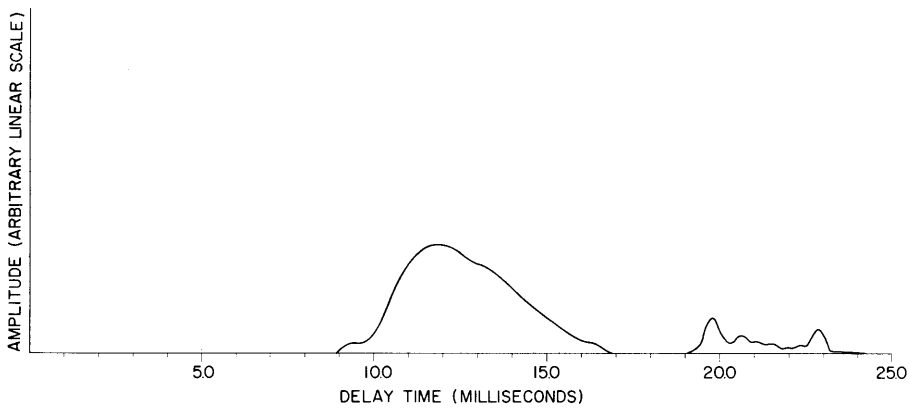

Fig. 20 - Predicted ground-backscatter distribution for ETR launch 3670 with the E- and F-layer contributions superimposed

Figure 21 contains the simulated doppler-shift behavior of the missile traveling along the trajectory indicated on the ray plots, once again with both contributions superimposed. No void in coverage is indicated, with the vehicle illuminated from 50 sec to 140 sec after launch. Figure 22 shows the actual observed doppler-shift-versus-time behavior. In Fig. 22 the data are ambiguous, as always, with all doppler shifts outside the 0- to 45-Hz frequency interval folded into that interval. The predicted doppler shift behavior is drawn on Fig. 22 for convenience in comparison. The E-layer contribution

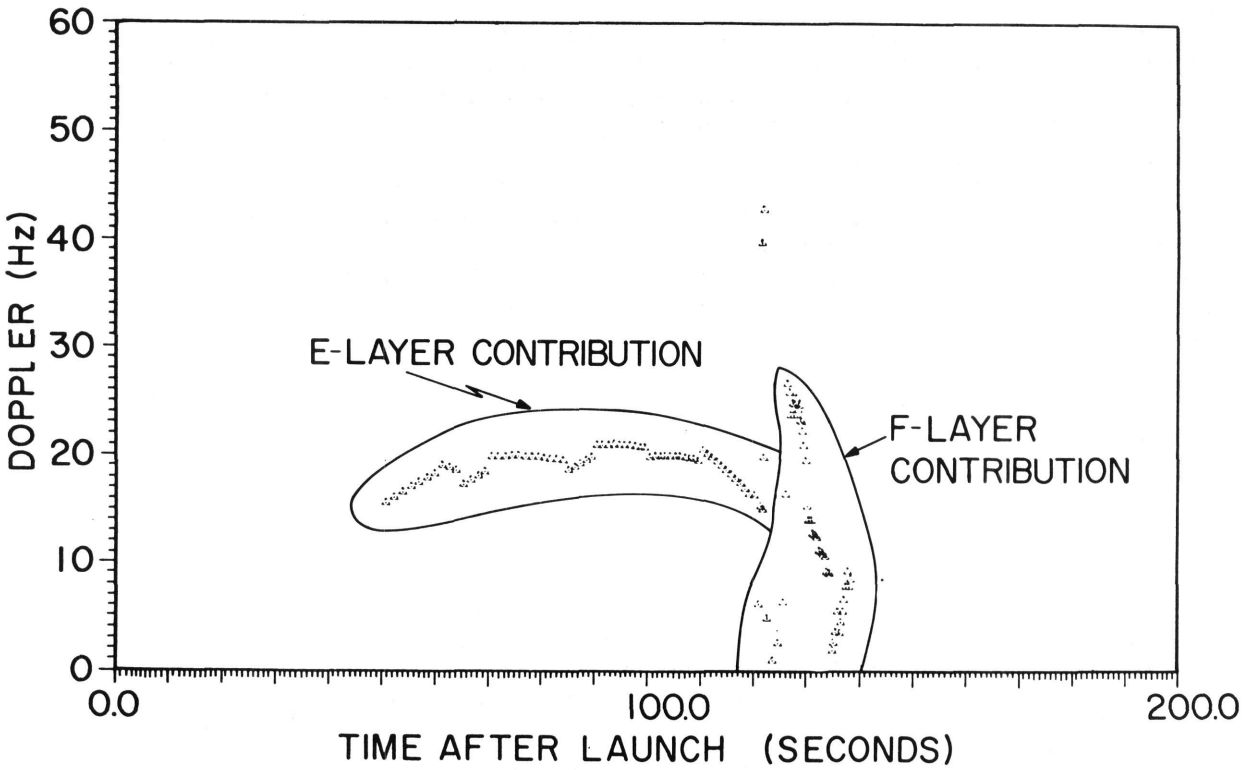

Fig. 21 - Simulated signature for ETR launch 3670 with the E- and F-layer contributions superimposed

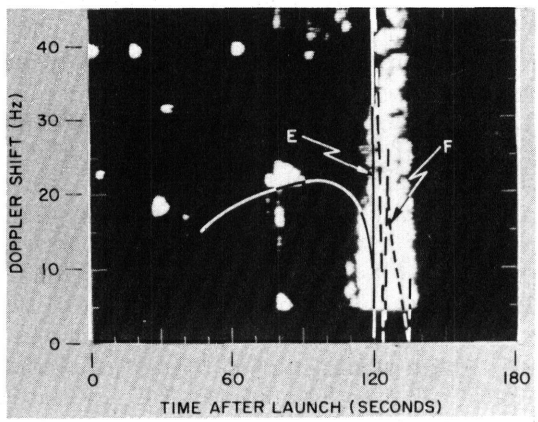

Fig. 22 - Observed signature for ETR launch 3670

is indicated by a solid line, and the F-layer contribution is indicated by a dashed line. Time blobs appear in a line at 39 Hz. It is evident at a glance that the actual E-layer coverage is not nearly as complete as predicted. This circumstance is partially a result of the sparse illumination (indicated by a low density of rays in Fig. 19a) of the initial part of the missile trajectory. It also lends some validity to the artificial suppression of the E-layer electron density which was necessary to reproduce the F-layer contribution to the ground backscatter, and illustrates once again the difficulty of

ionospheric propagation analysis in an environment of sporadic E ionization. The ground-backscatter echo, as well as the direct ionospheric backscatter echo which is received by a vertical-incidence ionosonde, represent the summed contributions from a large region of the ionosphere and cannot display the likely localized character of sporadic E reflection regions. Radar illumination and reflection from a small target depends on a point-to-point path which traverses only a small part of the ionosphere. The characteristics of this small patch of ionosphere cannot be fully described by vertical or oblique sounding methods which represent averaged results from large reflecting regions. The study of sporadic E phenomena, as well as other localized ionospheric reflecting anomalies, forms a large part of NRL's planned future program in over-the-horizon radar.

The E-layer contribution in Fig. 22 begins at approximately 75 sec after launch and falls on the predicted doppler-shift line. Its disappearance at 90 sec after launch suggests (by comparison of the missile trajectory with the ray-trace result) that the sporadic E ionization was localized to within 900 km of the radar site, permitting rays which reached E-layer altitude at farther ranges to continue upward.

The initial onset of the missile signature at 75 sec after launch suggests that the E-layer ionization was inadequate to support reflection at radiation takeoff angles exceeding 5.3 degrees; this circumstance contradicts the ionograms which were used for the ray trace, and permits the F-layer coverage which was indeed achieved. Reappearance of the missile echo at approximately 112 sec after launch corresponded to a missile location where E-layer coverage was still predicted, but the propagation in this region was nearly rectilinear; hence the echo observed could well have resulted from nearly line-of-sight coverage by only slightly refracted energy. The F-layer contribution in Fig. 22 obeyed the predicted behavior insofar as the resolution of the radar display permitted, and the signal disappeared at the predicted time, suggesting that the layer-height measured by the ionosondes for the F layer did indeed correspond to its true location.

July 30, 1964, also was a date on which two Polaris missiles were launched within a short time of each other. ETR launch 3670, above, and ETR launch 3688, whose launch and illumination data appear in Table 6, present a second opportunity to compare the signatures of two identical missiles which were launched under very similar ionospheric conditions. No earth backscatter photograph is available for this later period, but ionospheric conditions change slowly at midday in summer; hence, Fig. 18 may be considered approximately valid for the later interval as well. Ionograms from the later time were used for a propagation simulation, and, as in the earlier period, a separate treatment of the E- and F-layer contributions was necessary. Figures 23a and 23b contain separate ray plots for the two contributions. This later simulation, in comparison with Fig. 19, predicts a slightly more dense E layer, and hence a closer-range leading edge for the illuminated region. It also indicates a slightly lower and slightly more refractive F layer, which would tend to bring the leading edge of its illuminated region closer to the radar site. Figure 24 contains the simulated earth echo, although in this case the contributions have not been superimposed, since they were not plotted by the computer to the same scale. Figure 24a, showing the E-layer contribution, is compressed in amplitude by a factor of ten relative to Fig. 19, and also to Fig. 24b, showing the F-layer contribution. The large initial peak in Fig. 24a, which is actually eight times the amplitude of the earlier E-layer echo peak, arises from the highly focused bunch of rays which is incident at about 1100 to 1150 km from the radar site in Fig. 23a. This component does not make a contribution to the illumination of the missile trajectory. The smaller hump in Fig. 24a is at the same position and same amplitude as the E-layer contribution in the earlier period. The F-layer contribution in Fig. 24b is at the same amplitude, but it is 3.5 msec closer in time delay than that during the earlier period. This circumstance

Table 6
Data for Eastern Test Range Launch 3688

Missile Type	Launch Time (EST)	Radar Frequency (MHz)	PRF (pps)	Pulse Length (at -20 dB points) (μsec)	Average Power (kw)	Illumination Modes
Polaris A3	1200:03	18.036	90	700	100	E and F Layers

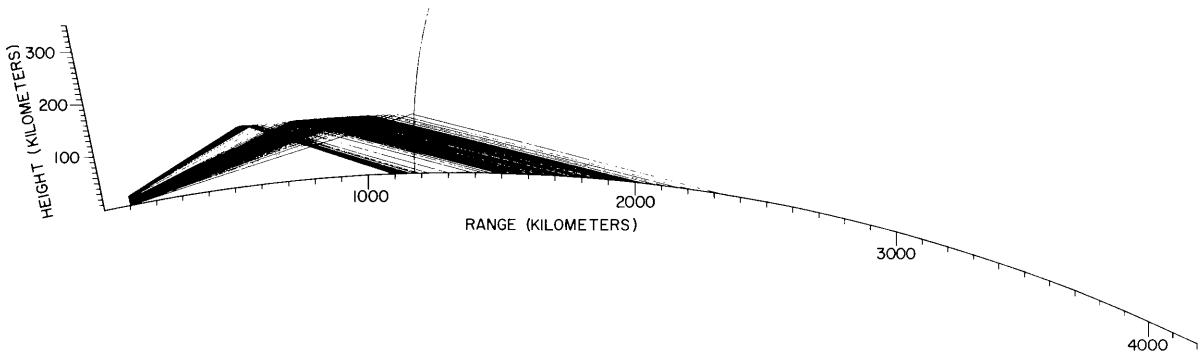

Fig. 23a - Ionospheric ray plot for ETR launch 3688, E-layer propagation

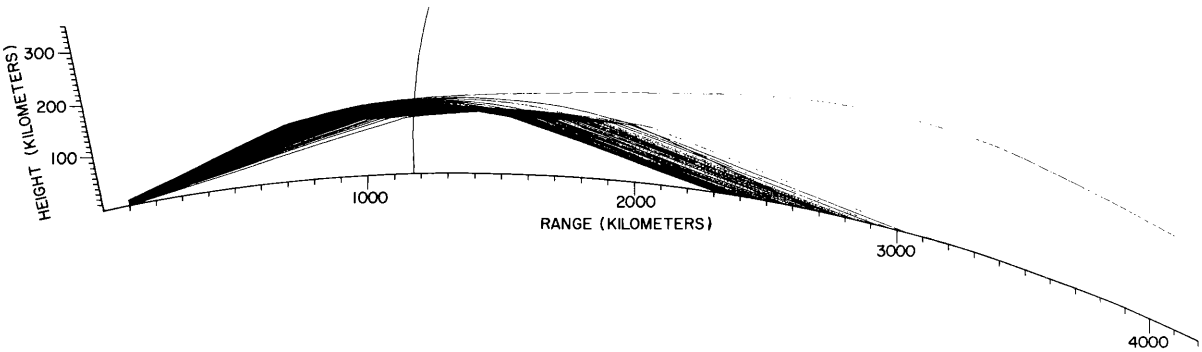

Fig. 23b - Ionospheric ray plot for ETR launch 3688, F-layer propagation

would be expected to make the F-layer contribution to the missile signature appear earlier than before. It should also be noticed in Fig. 24b that the F-layer earth echo extends, at a barely discernible level, somewhat beyond that in Fig. 20.

Figure 25 contains, superimposed, the simulated doppler-shift profile from both the E-layer and F-layer contributions for ETR launch 3688. Earlier acquisition of the target than for the previous example is predicted by virtue of the denser E layer, although

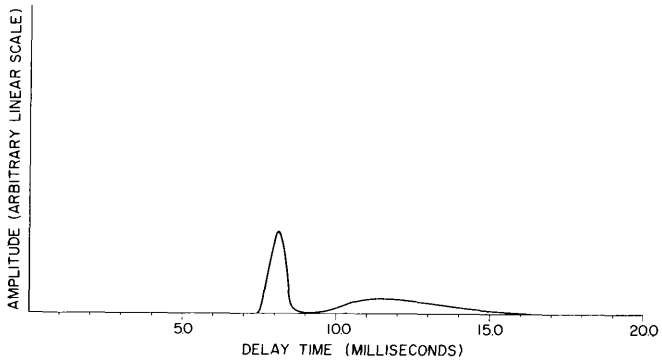

Fig. 24a - Predicted ground-backscatter distribution for ETR launch 3688; E-layer contribution

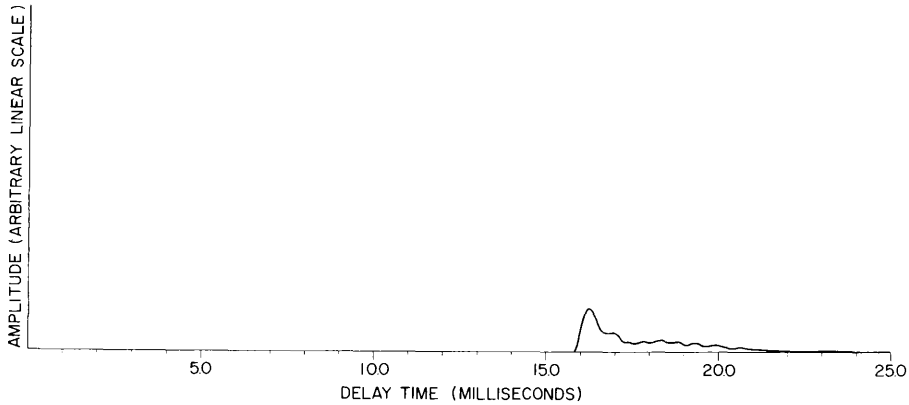

Fig. 24b - Predicted ground-backscatter distribution for ETR launch 3688; F-layer contribution

illumination of the launch point is in this case provided by a null in the antenna pattern, as indicated by the low density of rays at the launch point in Fig. 23a, and by the valley at 9 msec delay in Fig. 24a. The F-layer contribution, as expected, appears earlier than the F-layer contribution for the previous example. Figure 26 is the observed signature for ETR launch 3688, with the simulated signature from Fig. 25 superimposed.

As in Fig. 22, the predicted E-layer contribution appears as a solid line, and the predicted F-layer contribution appears dashed. The earliest possible occurrence of the missile signature is the small trace which appears at the small, sharp peak on the predicted E-layer contribution in Fig. 26. This trace is not claimed as a verifiable missile echo, however. The diffuse trace at about 80 sec after launch, between 30- and 45-Hz doppler shift, is definitely a missile echo. No explanation of its displacement from the predicted doppler shift is attempted, nor is any additional explanation offered for the absence of other evidence of an E-layer contribution. The F-layer contribution, however, is distinguished from that in Fig. 22 by its early appearance, intense character, and long persistence. These qualities all are appropriate to the denser, more extensive F layer which was predicted by the simulation. That the persistence of this F-layer

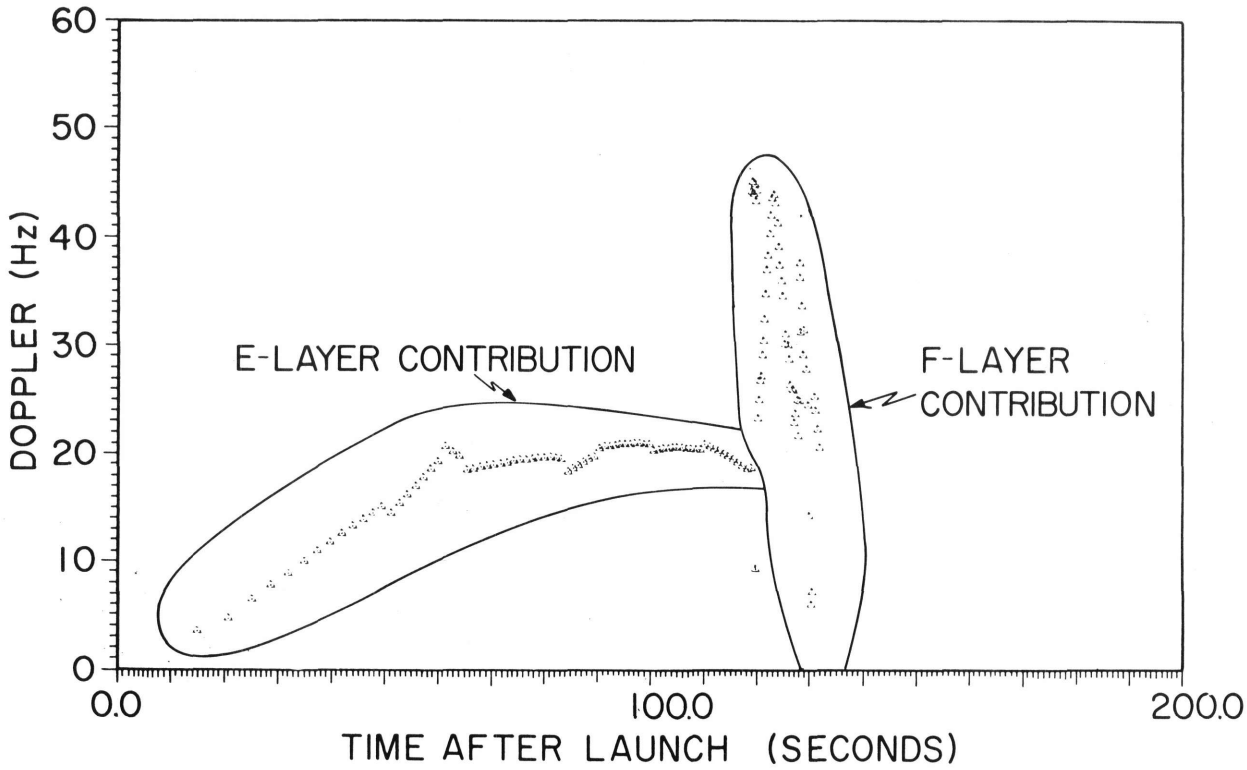

Fig. 25 - Simulated signature for ETR launch 3688. The E- and F-layer contributions are superimposed.

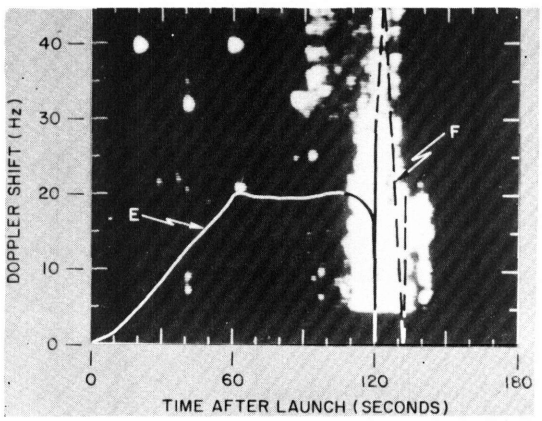

Fig. 26 - Observed signature for ETR launch 3688

contribution is a result of propagation circumstances is suggested by the fact that ETR vehicle 3688 burned out 6 sec earlier than the previous vehicle, for which a less extensive F-layer contribution was acquired.

An example of the computer simulation which illustrates the degree of complexity that can be introduced into a missile signature when there exists a multiplicity of propagation paths is represented by the analysis of Eastern Test Range launch 0324 of Jan. 20, 1964. The pertinent launch and illumination data appear in Table 7.

Table 7
Data for Eastern Test Range Launch 0324

Missile Type	Launch Time (EST)	Radar Frequency (MHz)	PRF (pps)	Pulse Length (at -20 dB points) (μsec)	Average Power (kw)	Illumination Modes
Polaris A3	1202:00	13.560	90	700	100	E and F Layers

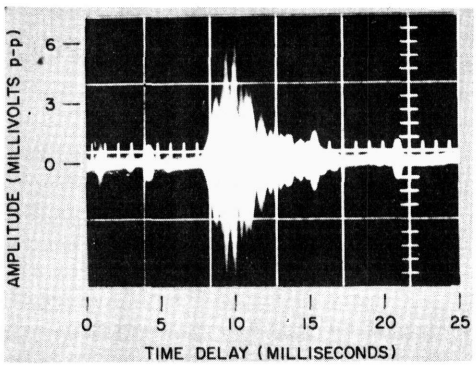

Fig. 27 - Observed ground-backscatter distribution, 1225 EST, Jan. 20, 1964, ETR launch 0324

Figure 27 is a photograph of the earth echo acquired at a period slightly after the launch, indicating coverage from about 8-msec to 17-msec time delay, with clearly delineated peaks in amplitude at 9.0 msec, 9.6 msec, and 10.4 msec, a multiple peak between 10.8 msec and 11.2 msec, and another pronounced peak at 12 msec. The subsequent gradual decline in amplitude is complete at approximately 17 msec (the apparent peak at 16 msec is a calibration pulse).

The computer simulation, constructed as always from ionograms near both ends of the propagation path, yielded the ray plot in Fig. 28. This ray plot indicates a complex mixture of E- and F-layer propagation, with F-layer coverage

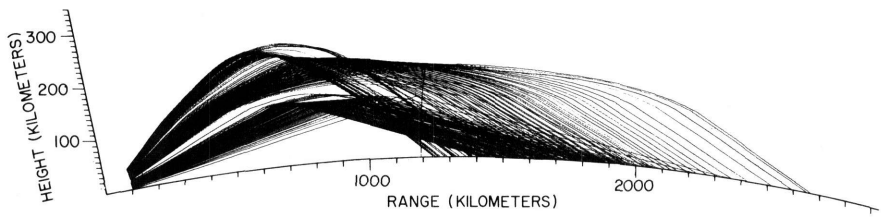

Fig. 28 - Ionospheric ray plot for ETR launch 0324

dominant at the far ranges, and E-layer coverage of primary importance within a 2000-km range. Figure 29 presents the ground-backscatter versus time delay simulation, which can be compared directly with Fig. 27. The simulated ground-backscatter plot predicts the relative positions of the various measured peaks, their relative heights, and the depths of intervening nulls to a remarkable degree. It displays a systematic lag in time delay of approximately 0.5 msec, however, and also fails to predict as accurately as in other cases the time delay at which illumination coverage begins. This failure is not considered to be a serious one, however, insofar as the missile-signature data presented below indicate quite strongly that the close-in coverage suggested by the backscatter photograph, in contrast to the simulation, was actually not achieved in the direction of the missile-launch region. This circumstance confirms once more the opinion that data acquired on a broadbeam antenna cannot be used reliably to predict the behavior of a point-to-point transmission path.

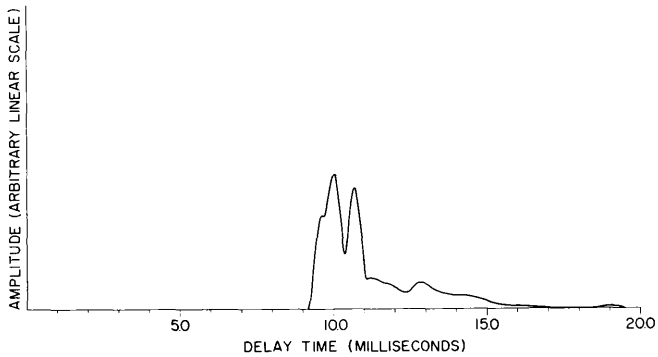

Fig. 29 - Predicted ground-backscatter distribution for ETR launch 0324

Figure 30 shows the simulated doppler frequency behavior of ETR launch 0324, and (as promised) the predicted signature is rather complex. Different doppler-shift behavior is indicated throughout the illumination period for two, and sometimes three, separate paths. It should be mentioned here, as a reminder, that no prediction of illumination *amplitude* has been made, and that the initial period of the simulated signature, beginning 50 sec after launch, actually corresponds to extremely weak illumination via high-angle F-layer propagation. Figure 28 illustrates this circumstance on portions of the missile trajectory immediately after the launch.

Figure 31 shows the observed doppler frequency vs time of the signature acquired during this launch. It should be noted that the time scale in Fig. 31 is compressed relative to the time scale of previous illustrations of the same type by a factor of approximately 2.5; hence, detail is lacking in comparison. A row of time blobs appears at 30 Hz. The straight slanted line rising from 13 Hz at 72 sec to 30 Hz at 138 sec after launch is a contaminant and should be ignored. The presence of radio interference throughout the launch period gave rise to many such extraneous responses and, in fact, contributed to a general deficiency in system sensitivity which resulted in a degraded signature. Figure 31 is included here largely for completeness; of principal concern in its treatment is the comparison of observed and predicted ground backscatter for complicated propagation conditions. It may be seen on this illustration that the two vertical stripes, at 124 sec and 135 sec after launch, coincide with the period in which wide excursions of doppler

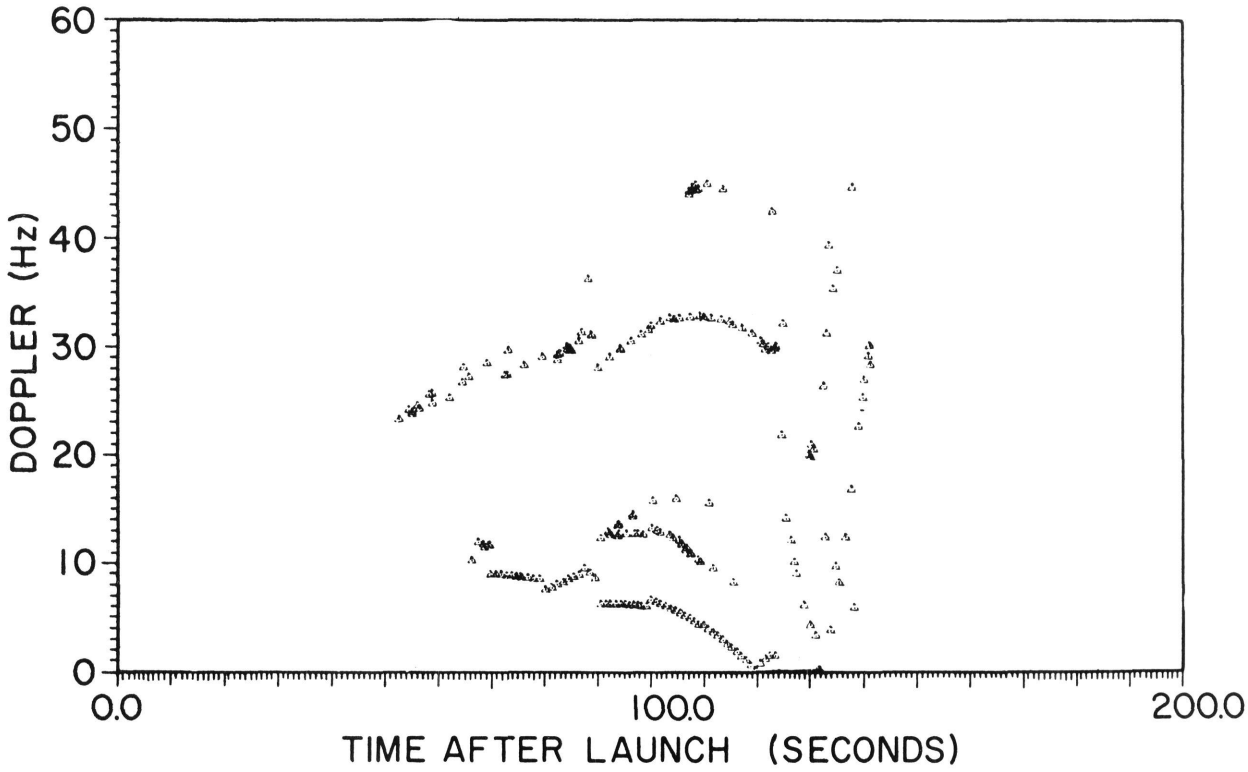

Fig. 30 - Simulated signature for ETR launch 0324

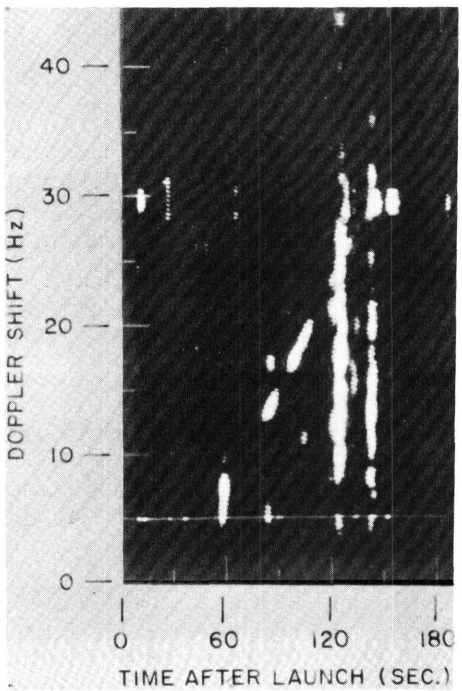

Fig. 31 - Observed signature for ETR launch 0324

frequency are predicted on Fig. 30. The onset time of 124 sec occurs during the rapid-acceleration phase of the missile flight, as indicated on Fig. 30, and the fact that earlier acquisition of the target was not effected indicates that the E-layer and high-angle F-layer propagation illustrated on Fig. 28 did not contribute to the signature. Although the F-layer coverage might be expected to be weak, the absence of an E-layer echo is somewhat of a surprise, and could possibly have resulted from the decreased system sensitivity.

A sixth example of this more-or-less standard, combination E- and F-layer propagation coverage is represented by the analysis of ETR launch 0038, of April 6, 1964. Pertinent launch and illumination data appear in Table 8. Figure 32 is a ground-backscatter photograph taken a few minutes after the launch, displaying continuous coverage in time delay from approximately 6 msec to beyond 15 msec. The sharp peak in amplitude at 10 msec is simply a member of the sequence of calibration pulses which stretches across the time base at 5.5-msec intervals. The peaks in ground backscatter

Table 8
Data for Eastern Test Range Launch 0038

Missile Type	Launch Time (EST)	Radar Frequency (MHz)	PRF (pps)	Pulse Length (at -20 dB points) (μsec)	Average Power (kw)	Illumination Modes
Polaris A2	1130:03	15.595	90	700	100	E and F Layers

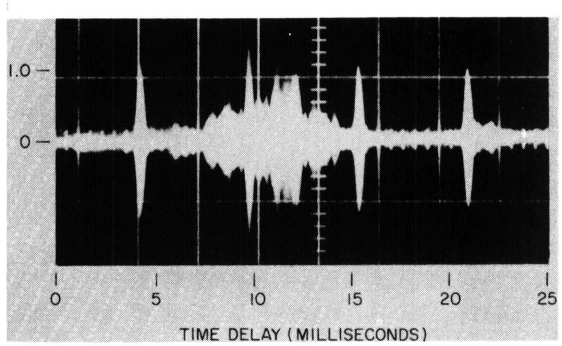

Fig. 32 - Observed ground-backscatter distribution, 1142 EST, Apr. 4, 1964, ETR launch 0038

occur at two locations: between 7- and 9-msec time delay and, at a higher level, between 11- and 13-msec time delay. Ionospheric soundings taken at the extremes of the propagation path could be treated only with similar complications to those involved in ETR launch 3670. Separate treatment of the most intense E-layer contribution to the illumination was necessary to properly include the highest-frequency extreme of the E-layer ionosonde trace. Figure 33a is a ray plot of this E-layer contribution. Figure 33b contains the normal E-layer contribution (i.e., that which could be expected to accompany the existing F-layer propagation), together with the appropriate (but small) F-layer contribution. Figure 34 is the total simulated distribution of ground-backscatter versus time-delay. It should be noticed that, as has come to be expected, the positions of the peaks in ground-backscatter amplitude and the time delay positions at which coverage begins and ends in Fig. 34 are remarkably faithful to the actual measurement in Fig. 32. However, it should be noted that in Fig. 34 the E-layer contribution, between 7- and 8.5-msec time delay, is disproportionately high in relative amplitude. This effect is greatly exaggerated in comparison to a similar but less apparent circumstance displayed in Figs. 18 and 20, which stemmed from separate E- and F-layer treatments also. In both cases this behavior may be at least speculatively attributed to the fact that the amount of energy which was able to completely *penetrate* the E-layer (quite a large proportion in the present case, as evidence by the large F-layer ground echo in Fig. 32) cannot be treated in the present backscatter analysis program, in which partial layer penetration is not permitted.

Figures 35a and 35b contain the simulated behavior of the missile's radar echo in doppler shift versus time after launch. Figure 35a represents the contribution due to the strong, blanketing-type E layer, while Fig. 35b represents the contribution from the normal E and F layers. It should be noticed that, where these two illustrations coincide, they predict nearly identical behavior. The former predicts earlier signal acquisition,

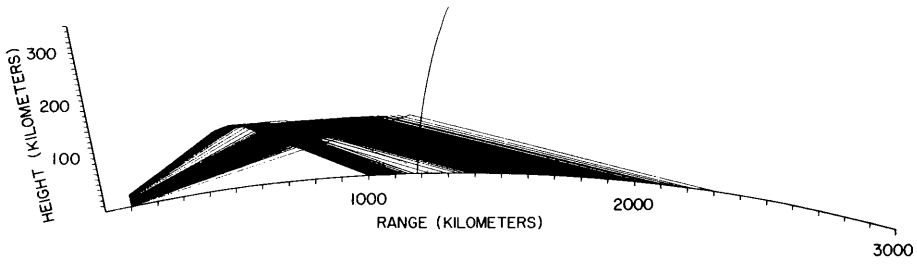

Fig. 33a - Ionospheric ray plot for ETR launch 0038, E-layer propagation

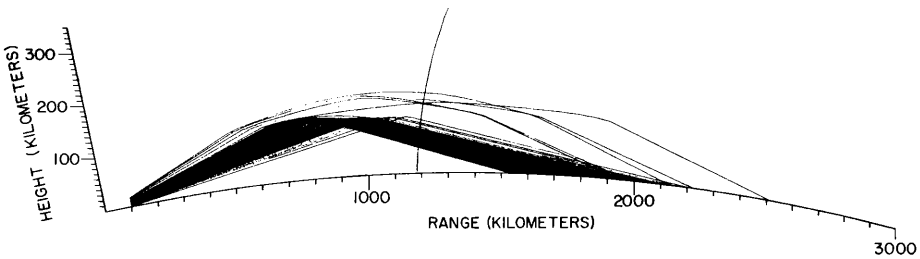

Fig. 33b - Ionospheric ray plot for ETR launch 0038, E- and F-layer propagation

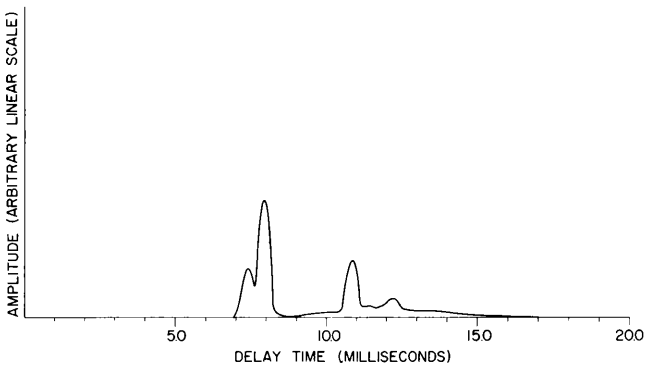

Fig. 34 - Predicted ground-backscatter distribution for ETR launch 0038 with the E- and F-layer contributions superimposed

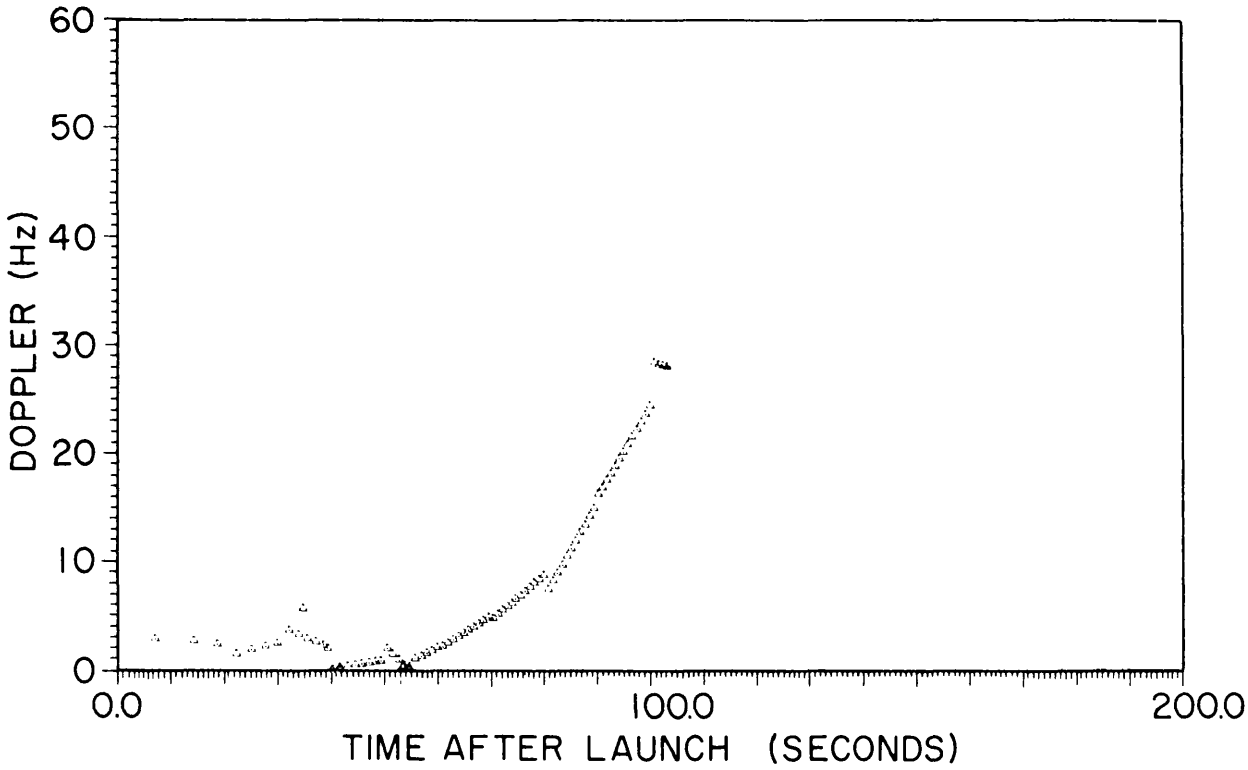

Fig. 35a - Simulated signature for ETR launch 0038, E-layer contribution

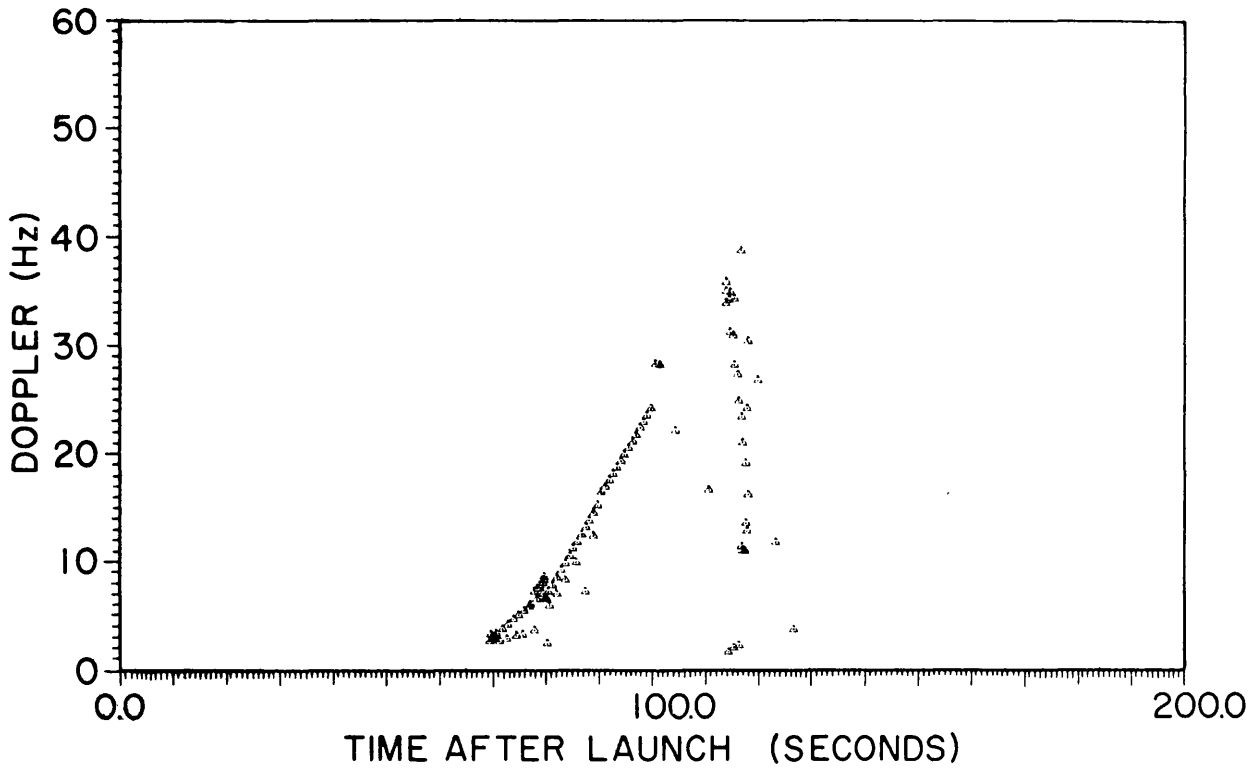

Fig. 35b - Simulated signature for ETR launch 0038, F-layer contribution

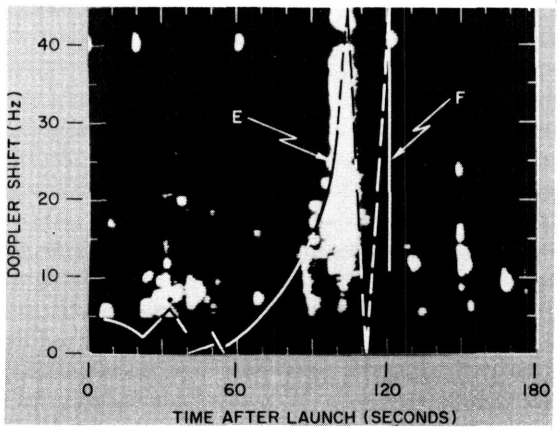

Fig. 36 - Observed signature for ETR launch 0038

and the latter predicts later signal loss plus a double propagation path between 70 sec and the end of the record. Figure 36 shows the observed version of this signature. The smears between approximately 20 and 50 sec after launch, and again between 85 and 110 sec after launch, are associated with the vehicle. A line is also drawn in Fig. 36 which corresponds to the behavior predicted by the computer simulation, with labeled solid lines to indicate the E- and F-layer illumination regions, and a dashed line to indicate the behavior in regions where the simulation predicted rather sparse coverage. (This sparsity is indicated by the low density of points in Fig. 35b between 100 and 115 sec after the launch.)

The measured data agree reasonably well with the predicted data, principally in the later E-layer illumination regions. However, radar echoes were acquired at the beginning of the period in which a void in illumination coverage was predicted. This circumstance is of particular concern in that the predicted void in illumination stemmed largely from the supposed passage of the vehicle through the E layer and into an illumination vacuum between the E and F layers. That such a vacuum did not exist, at least for several seconds after the vehicle passed through the expected altitude of the E-layer peak electron density, is evident, and it can only be suggested that the actual E-layer peak was somewhat higher than the ionospheric sounding data indicated. It is questionable whether any data were actually acquired by F-layer illumination, although the small blob at about 135 sec after launch and 12-Hz doppler shift falls on an extension of the predicted F-layer illumination line. It should be noted in this regard that radiation at the elevation angle necessary for this F-layer contribution was rather sparse, due to the occurrence of an antenna pattern null at that position.

The confirmed, missile-associated blob which occurs on Fig. 36 between 20 and 50 sec after launch does not fit well into the predicted doppler shift, although it does appear at a point when the predicted doppler shift passes through a local maximum. The reader is reminded that all doppler-shift information between 0 and 5 Hz on this photograph has been suppressed by the signal processor; hence, no signal data should be expected to appear until about 70 sec after launch. The behavior exhibited in Fig. 36 is a common phenomenon, however. The data acquired during ETR launch 3670, shown in Fig. 22, display a slightly similar tendency to appear above the predicted doppler shift between 80 and 90 sec after launch, and those for ETR launch 3688, shown in Fig. 26, display a pronounced displacement above the predicted doppler shift profile in this interval. These data also were acquired during a period when abnormally high E-layer illumination required the E- and F-layer propagation simulation to be conducted separately. Further evidence of this behavior under intense E_s blanketing is presented below. Tentatively, the interpretation which the authors have chosen to apply to this behavior is contained in the following list of alternatives (in order of credibility):

1. the sporadic E patches which were responsible for these contributions were actually in motion at the indicated velocities, and with the turbulences indicated by the wide doppler spread of the data (especially in the latter case),

2. the broad spread of the data was in fact simply a result of a momentarily saturating signal at some unmonitored stage of the signal-processing apparatus, which served to broaden the spectrum of the ETR 3670 signature slightly and to spread the spectrum of the ETR 0038 signature well above the 5-Hz lower limit of the signal processor,

3. a target, such as a rapidly spreading shock front accompanying the vehicle, actually possessed the proper doppler spectrum to yield the observed signal, or

4. an extraneous echo from a meteor, or a noise burst, coincidentally occurred at the indicated time, in the appropriate range interval, and in the indicated doppler region, to yield a spurious missile-like signature.

Eastern Test Range launch 0303, of January 26, 1964, was also illuminated by E- and F-layer propagation and, in fact, presents possibly the best example ever acquired of the early portions of the signature which an over-the-horizon radar can obtain under favorable propagation conditions. The geographical circumstance of the Madre radar's location relative to the SLBM launch area on the Eastern Test Range is such that these conditions are achieved only occasionally, when particularly intense E-layer propagation is effected; an operational over-the-horizon radar can be located so that favorable conditions may be normal for expected hostile launch areas. Table 9 contains a summary of the launch and illumination data for this event.

Table 9
Data for Eastern Test Range Launch 0303

Missile Type	Launch Time (EST)	Radar Frequency (MHz)	PRF (pps)	Pulse Length (at -20 dB points) (μsec)	Average Power (kw)	Illumination Modes
Polaris A2	1459:06	13.56	90	700	100	E and F Layers

Figure 37 is a photograph of the earth echo which was made, unfortunately, more than 90 min before the launch. The usual behavior of even the midday ionosphere is variable enough over such a time period as to partially negate the value of this photograph for comparison with the computer simulation, which was based upon ionograms acquired much nearer the launch time. The observed ground-backscatter echo should be considered simply as an indication of *probable* conditions nearer launch time. Figure 37 shows illumination coverage beginning as close as 6 msec and extending approximately to 16 msec in time delay, with amplitude peaks at about 9 and 12 msec. Figure 38 is the computer-generated ray plot pertinent to this example, with an important E-layer contribution plus a substantial F-layer component. It should be noted that Fig. 38 illustrates continuous, high-density illumination of the missile trajectory from shortly after launch until F-layer penetration. Figure 39 is the simulated earth-echo distribution based upon this ray plot, showing peaked but continuous illumination coverage at a range from 8 to 18 msec in time delay. This interval correlates reasonably well with the measured ground backscatter of Fig. 37 and, in particular, displays a pronounced peak at 12 msec in time delay, as does the observed version. This peak is directly attributable to a focused bunch of E-layer rays which pass just below the illumination void in Fig. 38. The illumination peak observed in Fig. 37 at 9 msec is vestigial in Fig. 39. Figure 40 is

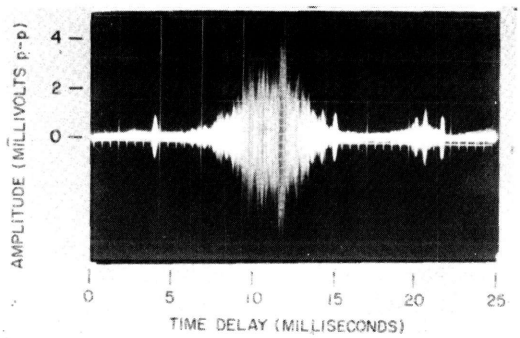

Fig. 37 - Observed ground-backscatter distribution (near launch time) on Jan. 26, 1964 for the ETR launch 0303

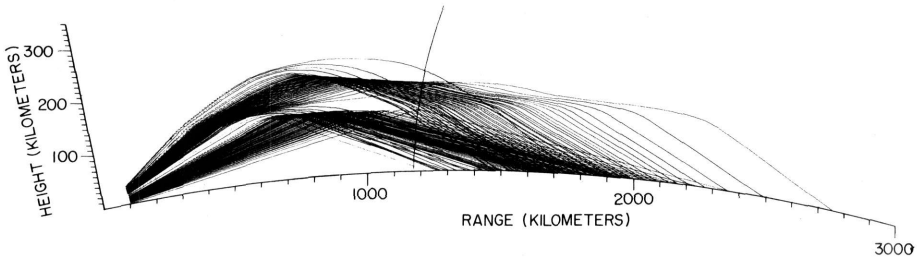

Fig. 38 - Ionospheric ray plot for ETR launch 0303

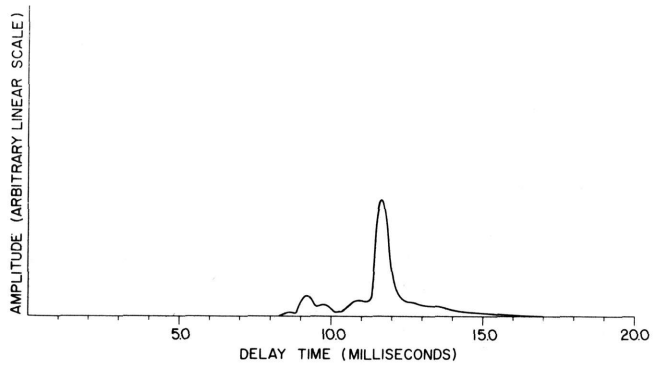

Fig. 39 - Predicted ground-backscatter distribution for the ETR launch 0303

the simulated signature of ETR launch 0303, showing a predicted signal onset at 20 sec after launch, and continuous reception from that time until more than 130 sec after launch. A multiplicity of paths is seen to contribute to the signature during much of its duration. Figure 41 is the observed version of the missile signature, and, as suggested, it represents the most complete Polaris signature yet acquired. There is a slight error in the doppler-shift scale of Fig. 41; the appearance of a signal below 5 Hz (where none should appear) suggests that the entire scale should be lowered by about 2 Hz. This slight adjustment would not materially affect the comparison between the predicted and the observed signatures. The high level of radio interference which existed during the

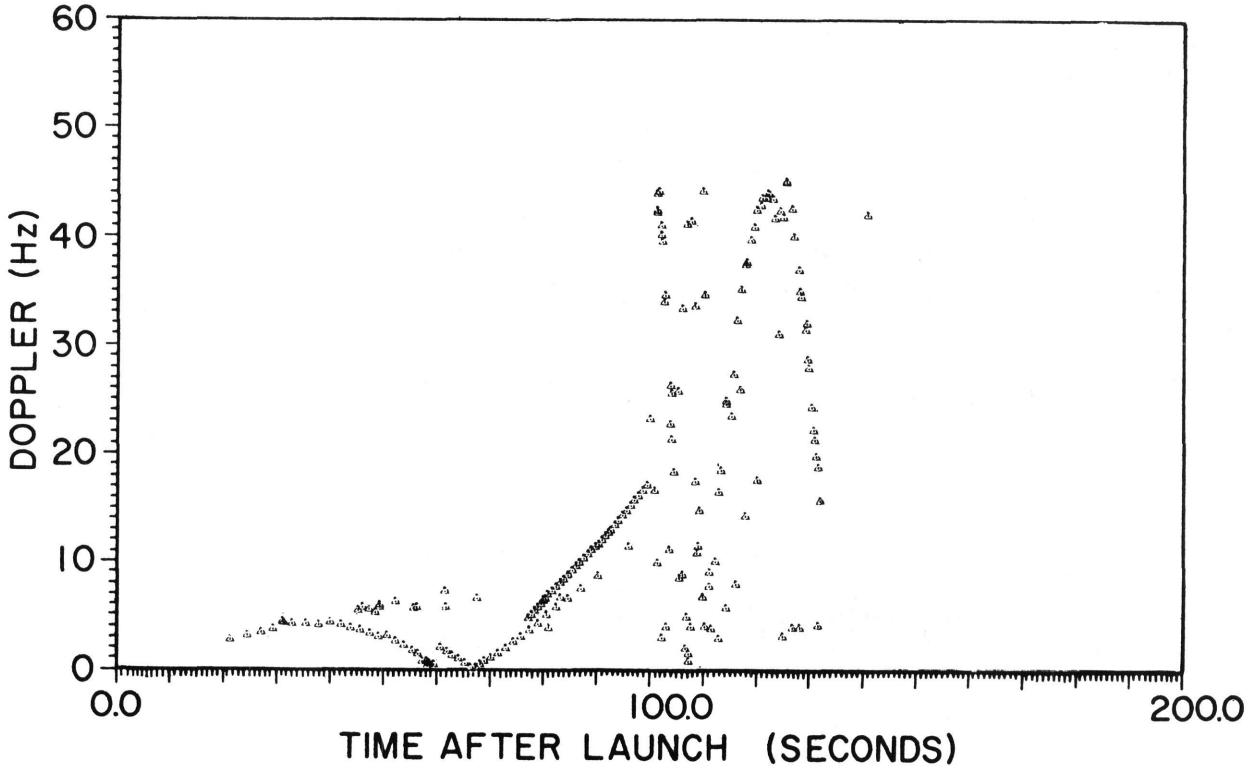

Fig. 40 - Simulated signature for the ETR launch 0303

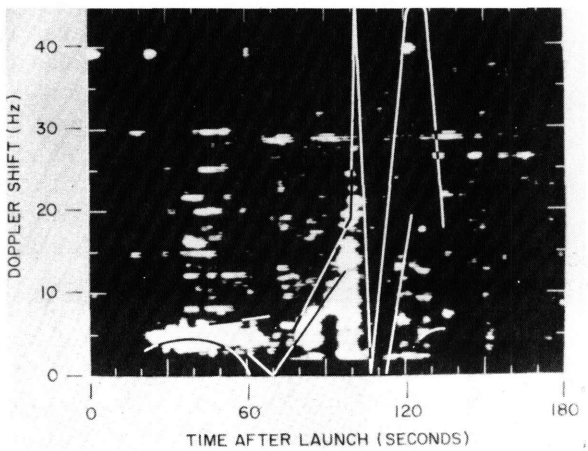

Fig. 41 - Observed signature for the ETR launch 0303

launch contaminates Fig. 41 somewhat, but most parts of the missile signature are unaffected. Superimposed on this illustration is an indication of the main features of the predicted signature behavior from Fig. 40. The simulated and measured signatures may be seen to match extremely well from the predicted (and observed) onset time of 20 sec after launch, until the signal was lost about 105 sec after the launch. The absence of the signal after this time indicates that the F-layer illumination actually achieved may have been much less intense than predicted, a situation which could stem from more intense E-layer blanketing than was predicted. The pronounced, early signature displayed in Fig. 41 suggests that the possibility of E-layer blanketing is, indeed, a strong one.

One more example of the combination of E/F layer illumination will be presented. Table 10 contains a listing of launch and illumination data for the ETR launch 4941 of September 28, 1964.

Table 10
Data for Eastern Test Range Launch 4941

Missile Type	Launch Time (EST)	Radar Frequency (MHz)	PRF (pps)	Pulse Length (at -20 dB points) (μsec)	Average Power (kw)	Illumination Modes
Polaris A3	1130:03	13.68	90	700	100	E and F Layers

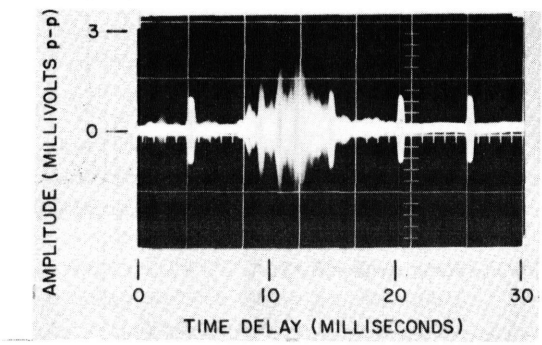

Fig. 42 - Observed ground-backscatter distribution at 1105 EST on Sept. 28, 1964 for the ETR launch 4941

Figure 42 is a time-exposure photograph of the ground-backscatter echo taken immediately after the launch, and indicates the illumination of the 8- to 20-msec time delay interval, with peaks in amplitude at 11 and 13 msec. The earth echo also displays a steady decline from 13 to about 15 msec, where a shallow hump appears, and a gradual decline from this point to 20 msec, where the echo descends into the noise. Figure 43 is the computer-simulated ray plot, displaying for the first time in this report the presence of three ionospheric layers. The usual E-layer contribution is responsible for the nearest-range illumination, followed by the contribution from an F_1 layer at 140 km altitude, and by the contribution from an F_2 layer at 180 to 240 km altitude. It should be noted that a pronounced void in illumination of the missile trajectory is predicted in this case between the F_1 and F_2 layers, and a lesser void is predicted (largely due to antenna lobe structure) between the E and the F_1 layers.

Figure 44, the simulated version of the earth echo, displays the same prominences as Fig. 42. However, these prominences appear with a systematic lag of 1 msec throughout the first 4 msec of the simulated earth-backscatter echo. This circumstance can be interpreted to be the consequence of a gradual E- and F_1-layer downward tilt from north

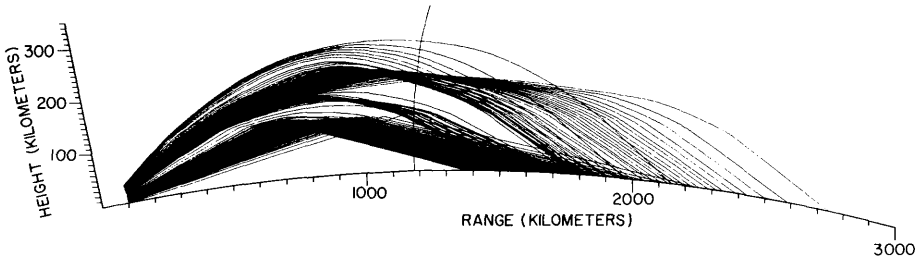

Fig. 43 - Ionospheric ray plot for the ETR launch 4941

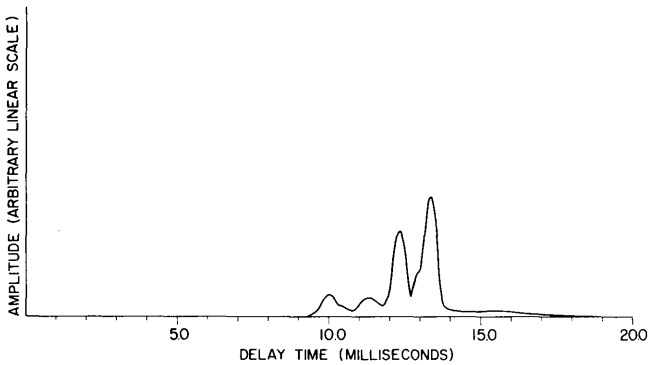

Fig. 44 - Predicted ground-backscatter distribution for the ETR launch 4941

to south along the propagation path. The F_2-layer contribution, which is represented by the last large peak, is faithful to the measured data. This comparison of the simulated and measured ground-backscatter echo suggests that, at least in this instance, the F_1-layer is more closely associated with the E layer than with the F_2 layer. Figure 45 shows the simulated doppler shift versus the time-after-launch profile, displaying quite clearly the illumination void between the F_1 and F_2 layers, in addition to an obvious mixture of propagation path contributions throughout the interval shown.

Figure 46 is the observed signature's doppler shift versus the time after launch, with the important parts of the simulated signature superimposed on it. The verifiable missile echo begins, nearly as predicted, at about 65 sec after launch, and although it is displaced to a point amidst the three predicted contributions, it does follow the shape of the predicted curves. A small component at 120 sec after launch, near 30 Hz, agrees well in doppler shift and onset time with a small predicted trace at that point. A trace with the same slope as that predicted appears to begin at that point and continue for several seconds. The lower frequency E-layer echo, represented by the hump at 15 to 20 Hz and at 85 to 105 sec after launch, disappears somewhat earlier than is predicted, indicating that the void in illumination coverage between the E and F_1 layers occurred lower than predicted. The F_1-layer contribution at about 30 Hz persists longer than expected. This circumstance suggests that the F_1 layer actually was higher than either the simulated or the measured ground backscatter indicated. The F_2-layer contribution enters

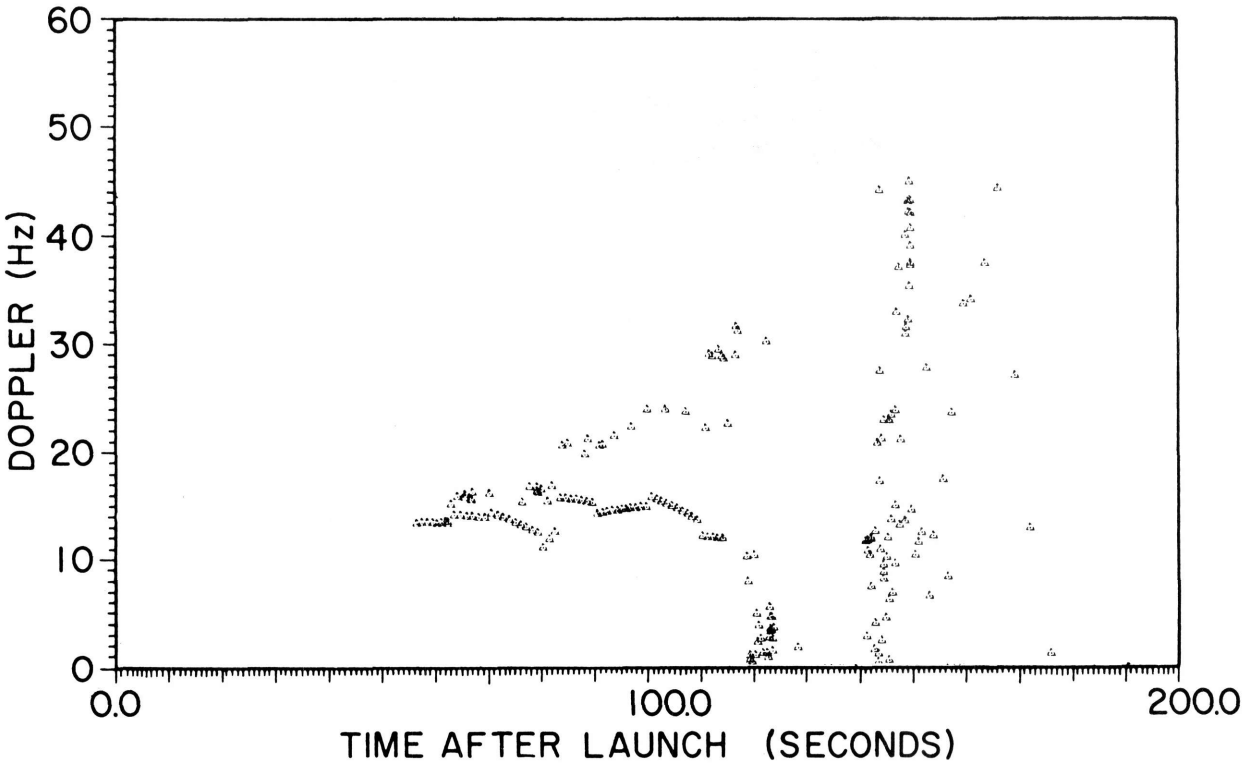

Fig. 45 - Simulated signature for the ETR launch 4941

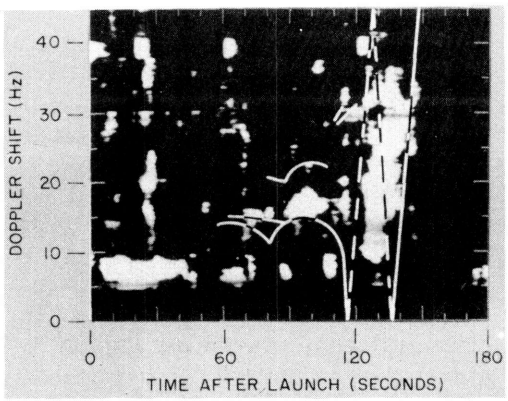

Fig. 46 - Observed signature for the ETR launch 4941

earlier than predicted and yields a contribution which falls along the dashed line segment (which was included to indicate the missile's expected doppler-shift behavior when it was in the predicted illumination void). The observed F_2-layer contribution possesses the same slope as the predicted version. The generally uncharacteristic appearance of Fig. 46 in comparison to other Polaris signatures confirms the implication of Fig. 45 that a multiplicity of propagation paths seems to have contributed to the later portion of the signature.

E-layer propagation, due to its simplicity, is so easily treated by even the most rudimentary of ray-tracing techniques as to be useful principally as a check on the accuracy of the methods used. The condition of E-layer blanketing is valuable, however, because under the present geographical constraints it affords the only opportunity for reliable illumination of a missile trajectory from the moment of launch until E-layer penetration. The signature acquired from ETR launch 0303, treated above, is one example of the complete coverage afforded by E-layer illumination, although in that case a substantial F-layer contribution occurred as well. Eastern Test Range launch 0238, of February 3, 1964, represented another excellent

example of the signature which a high-power, coherent over-the-horizon radar can be expected to acquire under conditions of thorough illumination coverage. Table 11 contains a listing of the pertinent launch and illumination data.

Table 11
Data for Eastern Test Range Launch 0238

Missile Type	Launch Time (EST)	Radar Frequency (MHz)	PRF (pps)	Pulse Length (at -20 dB points) (μsec)	Average Power (kw)	Illumination Mode
Polaris A2	1141:08	19.27	90	700	100	E_s Layer

Figure 47 is a photograph of the ground echo somewhat earlier than the launch, displaying illumination coverage from 7 msec to beyond 30 msec time delay. Only the first 20 msec, representing the first-hop illumination interval, are of concern in this analysis. The first peak in coverage occurs at 8 msec, followed by a null at 10.5 msec and a series of peaks between 12 and 16 msec. The subsequent null at 19 msec is the limit for single-hop propagation. Figure 48 is the appropriate ray plot, showing that the first null in illumination coverage is a result of the antenna pattern, and that the second, sharper null is a result of both the antenna pattern and the cessation of first-hop illumination coverage

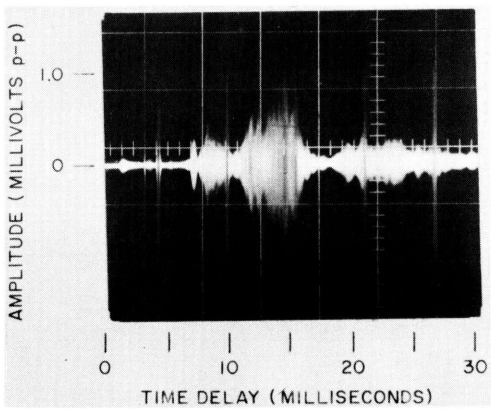

Fig. 47 - Observed ground-backscatter distribution at 1040 EST on Feb. 3, 1964 for the ETR launch 0238

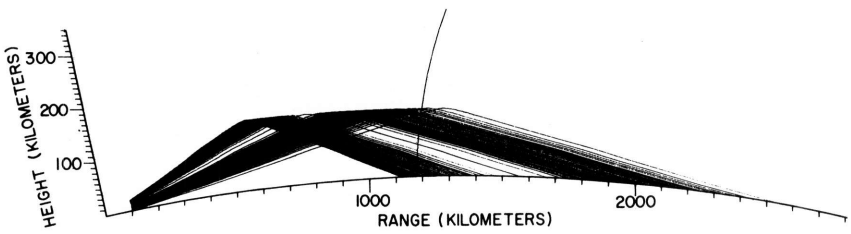

Fig. 48 - Ionospheric ray plot for the ETR launch 0238

in range. Figure 49 is the simulated ground-backscatter profile. This profile agrees remarkably well in the position of the earth echo and in the location of amplitude peaks and nulls; it fails to predict the relative height of the peaks accurately, however, and this fact once again attests to the vagaries of E_s propagation: it simply cannot be properly assessed with a narrow-aperture antenna.

Figure 50 shows the predicted doppler shift versus the time-after-launch for ETR launch 0238, and this illustration indicates that illumination of the missile trajectory should have been effected from launch time until the vehicle penetrated the E_s layer at

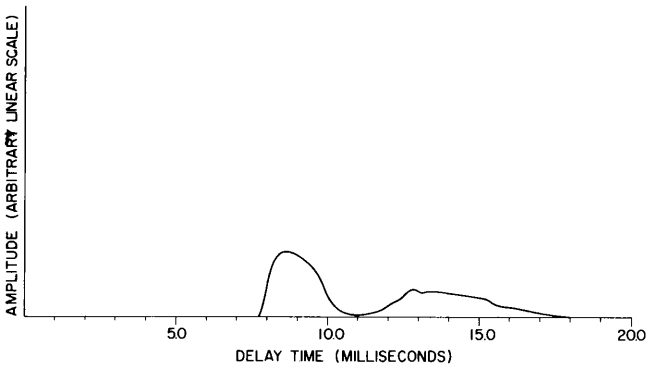

Fig. 49 - Predicted ground-backscatter distribution for the ETR launch 0238

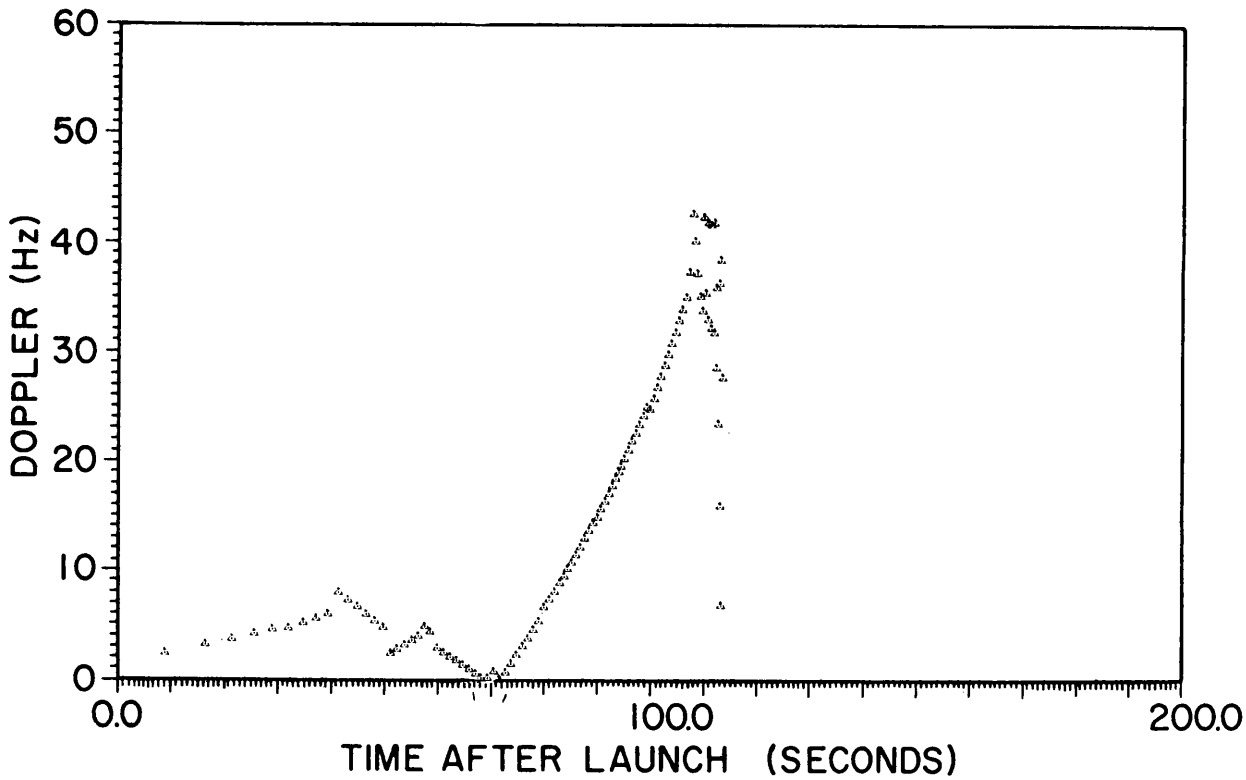

Fig. 50 - Simulated signature for the ETR launch 0238

114 sec after the launch. 'Figure 51 contains the observed data with the predicted signature from Fig. 50 superimposed. As in a previous case the predicted data are positioned along the time axis to yield the best possible fit to the observed data. As should be expected of such simple propagation geometry and thorough illumination, the comparison is striking. The fact that such a striking fit can be achieved by shifting the time axis slightly should satisfy the reader that this expedient, however arbitrary, is taken on adequate grounds. Although continuous agreement exists between the predicted and the measured data between 80 and 110 sec after launch, the earliest data appear to agree principally on the basis of their general shape and orientation. The earliest observed data, in agreement with the E_s data for ETR launch 0038 (Fig. 36), are displaced by 2 to 5 Hz above the corresponding predicted data. This behavior is given the same interpretation as in that previous case.

A second example of the simple, exclusively E-layer illuminated vehicle signature is represented by ETR launch 2949 of June 23, 1964, for which data appear in Table 12.

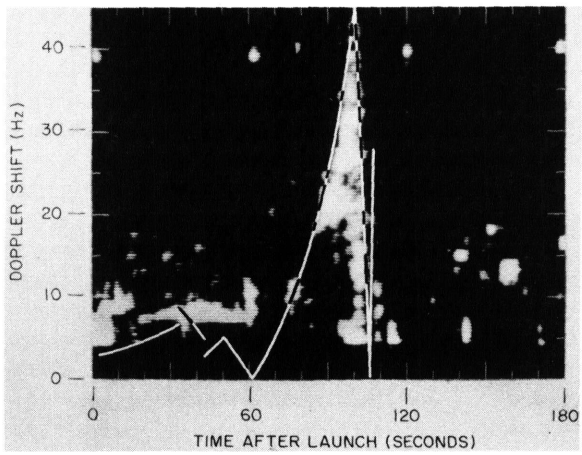

Fig. 51 - Observed signature for the ETR launch 0238

Table 12
Data for Eastern Test Range Launch 2949

Missile Type	Launch Time (EST)	Radar Frequency (MHz)	PRF (pps)	Pulse Length (at -20 dB points) (μsec)	Average Power (kw)	Illumination Mode
Polaris A2	1731:02	15.595	90	700	100	E Layer

There is no photograph of the earth backscatter echo available for the period during which ETR launch 2949 took place. However, the propagation condition at the time was recognized as indicating complete E-layer blanketing, and vertical-incidence ionograms from stations near the extremes of the propagation path confirmed this diagnosis.

Figure 52 is the ray plot determined from these soundings, showing a moderate condition of E-layer blanketing and illumination coverage of the missile trajectory from the launch point to the point of E-layer penetration at approximately 110 km altitude. Figure 53 is the simulated ground-backscatter echo distribution, with a sharp initial peak followed by a deep, antenna pattern-associated null at 9 msec time delay. The existence of this illumination null indicates that the earliest portions of the missile's trajectory were only sparsely illuminated. However, this circumstance cannot be used as a device for establishing the effect of the antenna pattern on signal acquisition (as might be attempted, for example, in comparison with ETR launch 0238, for which intense illumination of the launch point was effected and early signal acquisition was achieved) because, as the simulated doppler shift profile of Fig. 54 illustrates, the signal is predicted to be below the 5-Hz lower limit of detectability for 50 sec after launch. The missile does not have adequate relative velocity to yield a detectable signal until it has entered the region of intense illumination. The peculiar V-shaped discontinuity beginning 50 sec after launch in Fig. 54 occurs as a result of a change in the vehicle's motion, not as a consequence of the propagation geometry, or as an artifact of the sampling procedure used in the propagation analysis; hence, on this occasion irregular behavior of the simulated doppler shift profile can be expected to be seen on the measured version regardless of the fidelity of the propagation simulation. The remainder of Fig. 54 is more-or-less normal in appearance, with the abrupt predicted signal loss at approximately 113 sec after launch due to E-layer penetration (109-km altitude). Figure 55 shows the observed doppler shift versus the time-after-launch with the predicted signal behavior from Fig. 54 superimposed.

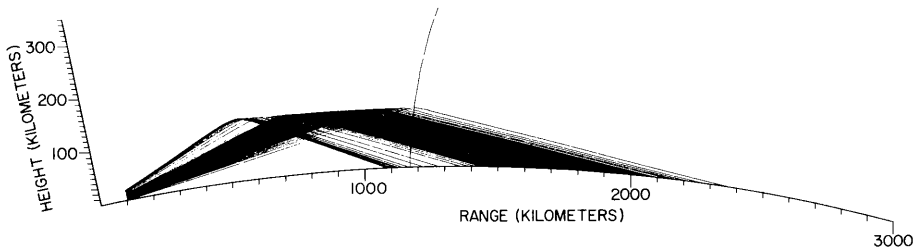

Fig. 52 - Ionospheric ray plot for the ETR launch 2949

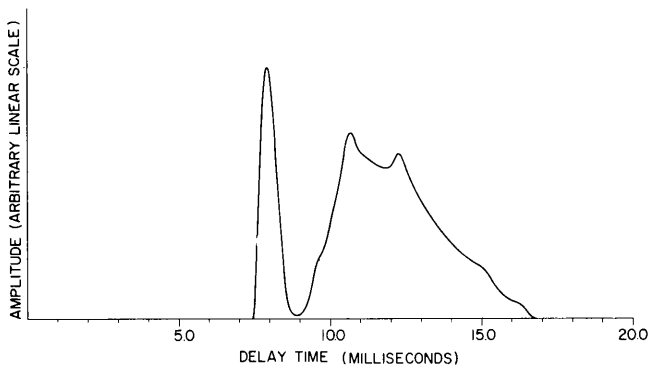

Fig. 53 - Predicted ground-backscatter distribution for the ETR launch 2949

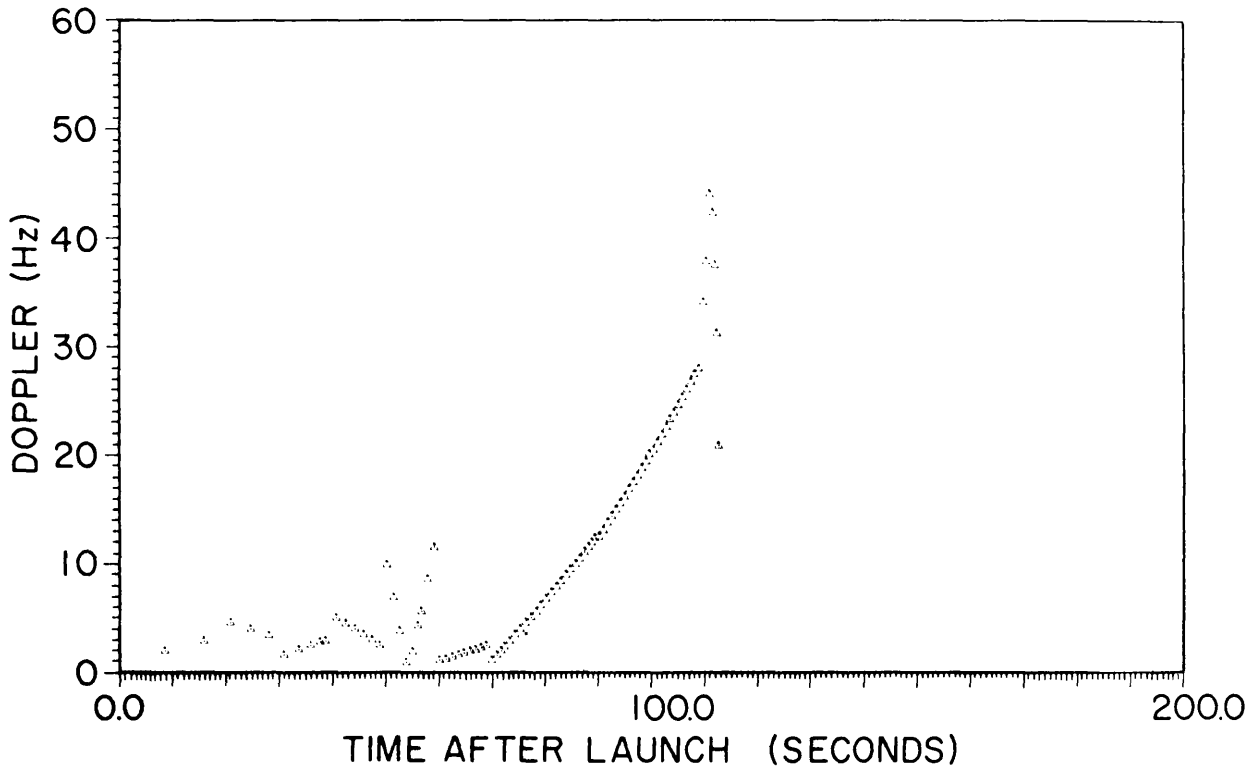

Fig. 54 - Simulated signature for the ETR launch 2949

The earliest obvious appearance of the missile echo in Fig. 55 occurs at the time and at the predicted position in doppler shift of the V-shaped discontinuity. It is interesting that, in this case, there is not observed an early signal displaced by 2 to 5 Hz above the predicted doppler shift, in contrast to other E-layer illumination examples. This circumstance confirms the notion that there exists no shock wave or exhaust-associated target moving more rapidly than the missile, which would be expected to be observed regularly. The small trace at 40 sec after the launch, displaced by about 2 Hz above the triangular peak on the simulated signature, is not claimed as a confirmed missile signature. The remainder of Fig. 55 displays a close similarity to the simulated version, with signal loss at about 113 sec after launch, as predicted. The sparsity of the measured data between 80 and 100 sec after launch is not explained, and most probably results from physical effects related to the effective target size and target composition during this period. An investigation of the physical mechanisms which affect missile target behavior in the ionosphere is a part of NRL's current program in ionospheric research.

CONCLUSIONS

The analyses presented here, while preliminary to the extent that they are based on an evolving propagation assessment technique, are consistent enough among themselves and successful enough on the average, that a set of tentative conclusions may be drawn from them. Table 13 is a compilation of successes and failures of the ray-tracing analysis, for the cases treated above, both for the prediction of ground-backscatter illumination and for the prediction of missile-signature behavior. It can be seen from Table 13 that the predictions (graded on a three-level scale of good, fair, or poor) are uniformly

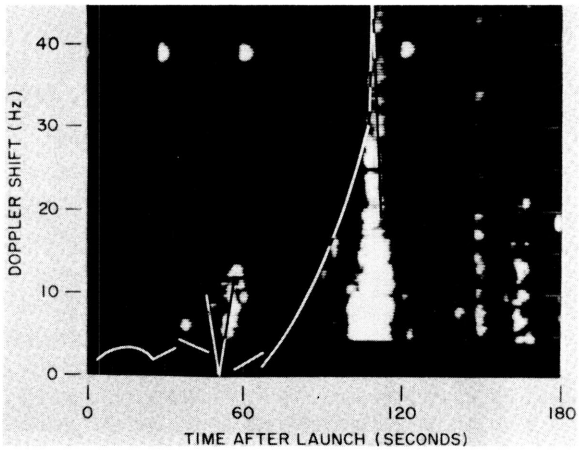

Fig. 55 - Observed signature for the ETR launch 2949

Table 13
Tabulation of Successes and Failures of the Ray-Tracing Analysis

Missile Launch Number	Propagation Modes*	Efficacy of Prediction							
		Ground Backscatter†				Missile Signature‡			
		Leading Edge	Trailing Edge	Relative Peak Placement	Relative Peak Amplitude	Onset Time	Loss Time	Illumination Voids	Doppler Shift
2955	E/F	Good	Good	Good	Fair	Fair	Good	Good	Good
2903	E/F⁻	Good	Good	Fair	Good	Poor	Good	Good	Good
3670	E⁺/F	Good	Good	Good	Good	Poor	Good	Poor	Good
3688	E⁺/F	NO DATA				Fair	Good	Good	Fair§
0324	E/F	Fair	Good	Good	Good	Poor	Good	Poor	Good
0038	E⁺/F	Good	Good	Good	Fair	Fair	Fair	Fair	Fair
0303	$E/F_1/F_2$	NO DATA				Good	Poor	Good	Good§
4941	E/F	Fair	Good	Good	Good	Good	Good	Poor	Good
0238	E_s	Good	Good	Good	Poor	Good	Good	Good	Good
2949	E_s	NO DATA				Good	Good	Good	Good§

*The notation E/F^- indicates a combination of E- and F-layer propagation, with only a small F-layer contribution. The notation E^+/F indicates such a combination with evidence of some E-layer blanketing.

†Predicted positions of leading and trailing edges of ground-backscatter echo are considered to be accurate if they are within 1/2 msec (approximately 75 km) of the observed positions. Relative positions of peaks are considered to be predicted accurately if they fall within 1/2 msec of the observed positions. Relative amplitudes of peaks are considered to be predicted accurately if they fall within 3 dB of the observed values.

‡Times are considered to be predicted accurately if they fall within 5 sec of the observed values. The doppler shift is considered to be predicted accurately if the signature's appearance conforms to the predicted curve shape, and values average within 10% of the predicted doppler shift behavior.

§Because the measured ground-backscatter data were acquired at times which differed substantially from the missile launch times in these cases, they were considered to be of little use in making a comparison with predictions.

good, with few exceptions, in predicting the placement of the ground-backscatter echo and the relative positions of the peak-amplitude contributions. They are slightly less successful in predicting the relative peak amplitudes, but the deficiencies in this regard almost invariably arise from propagation circumstances which the ray-tracing technique is not expected to treat accurately. The simulated missile signatures fit rather well in most aspects, with the notable exception of signature onset time (and also the doppler shift of the early E-layer echo in the same cases). This circumstance may also be attributed to recognized uncertainties, principally with respect to the treatment of intense, probably localized, possibly moving, sporadic E-layer patches. The inability of the computer simulation technique to predict the behavior of missile echoes under these conditions is not considered to be a deficiency of the analysis technique, but is regarded as an inadequacy of diagnostic information concerning ionospheric layer structure. It should be noted that in the cases where widespread, intense E_s-layer blanketing was known to exist, the simulated missile signature agreed extremely well with the observed version. This circumstance should be no surprise to the reader, since it simply reflects the fact that the ray-tracing analysis can be most efficacious in predicting missile signature behavior when the propagating medium is fully described.

It can be concluded from the analyses above, as indicated roughly by the data in Table 13, that the ray-tracing propagation analysis technique is very valuable under normal propagation conditions for predicting:

1. the location and the extent of ground-illumination regions,

2. the location and the relative intensity of localized peaks in illumination coverage within these regions, and

3. the positions of illumination nulls and their attribution to either antenna pattern effects or ionospheric layer structure.

With respect to predicting the behavior of rocket vehicles launched through well-known illumination profiles, the ray-tracing propagation analysis may be seen to be valuable in predicting:

1. signature onset and loss times,

2. doppler shift behavior, and

3. temporary signature loss due to illumination voids.

It may also be seen that the principal effects of incompletely understood illumination conditions are uncertainties in:

1. signature onset time and

2. early signature doppler shift.

It is believed that these deficiencies may be expected only in an environment of extensive, localized sporadic E-layer ionization. The actual movement of these localized ionization regions is suspect as the source of imprecision in the doppler shift predictions, while the inability of a narrow-aperture antenna to resolve the localized E_s ionization patches is suspect as the ultimate source of imprecision in the signature-onset predictions. The value of a wide-aperture antenna for further investigations to resolve this uncertainly is unquestionable. One further and more speculative conclusion may be

drawn from the two pairs of missiles which were launched within less than an hour of each other. It should be noted in comparing both the ground-backscatter and the missile-signature data (in particular from ETR launches 2955 and 2903) that (a) the small shifts in location of the local illumination peaks within the relatively stable ground illumination region were reflected clearly in the simulated ground-backscatter distribution, and (b) the effects of such shifts in illumination distribution upon missile-signature appearance are pronounced indeed. Hence, it may be at least suggested that detailed knowledge of ground-backscatter echo *fine* structure is vital to the employment of these data in a diagnostic role.

PLANS AND SUGGESTIONS FOR FUTURE STUDY

This initial attempt to use ionospheric ray tracing to study high-frequency radar ground-backscatter and launch-phase rocket echoes has been gratifying in that its success encourages further development of the technique so that more detailed study of ionospheric propagation and earth- and target-scattering phenomena may be conducted. There comes to mind a number of allied studies in ionospheric propagation which can be conducted in concert with further improvements in propagation analysis by the ray-tracing technique. It is believed that *joint* pursuit of experimental studies and theoretical and empirical propagation analyses can most effectively advance both areas of study, and the list of planned and suggested study programs which follows is recommended as being of the most immediate importance for this objective.

Target Radar Cross-Section Studies

It is planned to study the signal-amplitude behavior of signatures from over-the-horizon launch-phase missiles to further refine the knowledge to be gained regarding (a) the causes of scintillation effects observed in the signatures, (b) the behavior of metallic bodies in rapid motion through the ionosphere as scatterers of electromagnetic energy, and (c) the relative contributions to signatures from these targets due to exhaust components, shock-boundary ionization, and the inert bodies themselves.

It is planned to attempt a comparison of the radar echoing behavior of rocket vehicles traversing the ionosphere over a span of radio frequencies extending from the 10-MHz lower limit of the Madre research radar to the 435-MHz upper limit of NRL's vhf/uhf radar facility. This latter facility contains a steerable 150-ft-diameter parabolic reflector, and will soon contain a 5-MW peak power, 50-kw average power vhf transmitter. It is hoped that this radar will be provided with the necessary coherent frequency sources so that its data may be analyzed by the Madre signal processor for this investigation. The studies also will require detailed inspection of missile-signature data on a pulse-to-pulse basis, and it is planned to use the Madre digital signal processor in conjunction with NRL's CDC 3800 digital computer for the necessary data analysis.

Earth Backscatter Studies

A program of investigation into the scattering behavior of the earth at oblique incidence for decameter-length radio waves will be conducted with the aid of improved ionospheric ray-tracing techniques. The authors intend to construct a scattering model for the earth at these wavelengths based upon a comparison of predicted earth backscatter signals acquired from ray-tracing analysis with measured data. This study will require the further development of two- and three-dimensional ray-tracing methods which are

already under study at NRL, the Environmental Science Services Administration, Stanford University, and other places. It also is intended to combine this investigation of the earth's behavior as a scatterer with an attempt to improve the knowledge of the nondeviative ionospheric absorption phenomena which can be studied with the aid of the techniques being developed.

Wide-Aperture Antenna

It is proposed that an antenna or group of antennas be constructed to provide high power handling (5- to 10-MW peak power, 100- to 200-kw average power) capability and narrow beamwidths over the 6- to 40-MHz frequency band. This antenna or group of antennas should provide a beam of approximately 3 degrees beamwidth in both the elevation plane and the azimuthal plane, with the former of primary importance. This beam should be steerable in both azimuth and elevation, and the antennas should be constructed so that they may radiate in either easterly or westerly directions. This antenna ensemble will be used for (a) detailed study of the sporadic E-layer ionization which limits the accuracy of propagation analysis in an environment of patchy ionospheric layer structure, (b) study of irregularity motions which may give rise to extraneous doppler shifts in received echoes, (c) investigations of multipath and off-azimuth propagation and their implications with regard to measurement accuracy in target positions, and (d) further studies of the earth backscatter echo.

Speculations

Some applications of these techniques, together with other methods which may be used effectively to augment them, seem to have promise for use in an operational version of an over-the-horizon radar. In particular, it should be recognized that an ionospheric radar whose purpose is to survey a large geographic area and provide early warning of hostile rocket launches from within that area must be capable of handling a large volume of data on a continuous basis. The refinement of automated data handling and analysis techniques is absolutely necessary if these data are to be handled efficiently and if the maximum information is to be extracted from them. Of particular concern in the context of this report is the possibility of extracting trajectory information from the missile signature acquired by an ionospheric radar. It is believed that a useful estimate of such parameters as rocket launch point, intended target area, time of flight, and possibly even certain trajectory parameters can be acquired from a refined ray-tracing analysis of the type employed for the studies reported here, coupled with a certain degree of knowledge (or an intelligent guess) of the hostile missiles to be expected. The procedure of obtaining these estimates might proceed as follows.

1. Ionospheric sounders in the surveillance region (contained, perhaps, in buoys on the Atlantic and Pacific Oceans) would automatically sample the ionosphere on a continuous basis and would telemeter their data in digital form to a computer at the radar site.

2. A digitally controlled oblique sounder at the radar site would also sample the ionosphere regularly to fill in coverage gaps and provide range and azimuth calibration marks from transponders located upon the ionosonde buoys.

3. A continual refinement of the ionospheric propagation model for propagation to selected areas in the surveillance region would be accomplished by the computer, which would use the digital data input from the various sounders plus earth-backscatter data in

digital form from the radar itself. To permit near-real-time ionospheric ray tracing, and to permit frequent adjustment of the propagation model, the ray tracing itself could be carried out in a hybrid process. Digital data input could be used in conjunction with a more rapid analog solution of the appropriate propagation equations to accomplish this task.

4. Knowledge of some performance parameters of the targets expected (such as velocity profiles, and staging and thrust termination times and altitudes) would be used to generate *expected* missile signatures appropriate to likely launch points and target areas. This process could be conducted in a hybrid computer also, and the resultant signatures could be projected on radar display consoles or stored in a digital memory.

5. The radar operator would have a set of controls available for adjustment to alter a postulated missile trajectory and match an *actual* signature by adjusting launch and target points and whatever other appropriate parameters could be manipulated by changing the analog computer settings. This function could also be carried out partially by a digital computer, which could scan its memory for a stored sample signature which approximately matches the observed one and present this sample to the operator, who could make final adjustments via analog computer parameter changes.

The employment of these techniques in an operational over-the-horizon radar will require a substantial refinement in the methods of automatic pattern recognition and hybrid computer operation. It will also require the development of digitally controlled ionospheric sounders and refinement of the methods for extracting and exploiting ionosonde data in digital form. These areas are of interest to NRL, and it is proposed that they be pursued in connection with NRL's continuing efforts in ionospheric studies.

ACKNOWLEDGMENT

The authors are indebted to the staff of the Radar Techniques Branch, Radar Division, for the acquisition of the large volume of data upon which these studies have been based, and to Mr. Arthur Knopp, Search Radar Branch, Radar Division, for a painstaking critical review of the manuscript which has resulted in several important improvements.

REFERENCES

1. Page, R.M., "Storage Radar," NRL Report 3532 (Secret Report, Unclassified Title), Oct. 1949

2. Page, R.M., and George, S.F., "Magnetic Drum Storage Applied to Surveillance Radar," NRL Report 4878 (Confidential Report, Unclassified Title), Jan. 1957

3. Jensen, G.K., and Gager, F.M., "Crosscorrelation Electronic Storage Radar," NRL Report 5016 (Unclassified), Oct. 1957

4. Wyman, F.E., and Zettle, E.N., "Magnetic Drum Storage Correlation Radar," NRL Report 5023 (Secret Report, Unclassified Title), Nov. 1957

5. Davis, J.R., and Rohlfs, D.C., "Lunar Radio-Reflection Properties at Decameter Wavelengths," J. Geophys. Res. 69:3257-3262 (1964)

6. Davis, J.R., Rohlfs, D.C., Skaggs, G.A., and Joss, J.W., "Decameter-Wave Radar Studies of the Lunar Surface," Radioscience 69D(No. 12):1659-1667 (1965) (paper 69D12-619)

7. Davis, J.R., Headrick, J.M., Rohlfs, D.C., and Utley, F.H., "A High-Frequency Ionospheric Radar Study of High-Altitude Nuclear Detonations," NRL Report 5962 (Secret Report, Unclassified Title), May 1963

8. Davis. J.R., and Headrick, J.M., "A Comparison of High-Altitude Nuclear Explosion Effects in the E Layer with Variations in Geomagnetic Field Strength," J. Geophys. Res. 69:911-916 (1964)

9. Ahearn, J.L., Headrick, W.C., Headrick, J.M., and Ward, E.W., "Some Skywave Radar Constraints," NRL Memorandum Report 1811 (Secret Report, Unclassified Title), Oct. 1967

10. Gager, F.M., Headrick, W.C., Morgan, G.A., Utley, F.H., and Zettle, E.N., "MADRE Performance Part 1 - Very Long Range, Over-the-Horizon Detection of Aircraft with the MADRE Radar," NRL Report 5862 (Secret Report, Secret Title), Dec. 1962

11. Gager, F.M., Headrick, W.C., Morgan, G.A., Rohlfs, D.C., Tesauro, C.B., and Zettle, E.N., "MADRE Performance Part 2 - Observations of Feb. 8, 1962," (Unclassified Title), "MADRE Performance Part 2 - Very Long Range, Over-the-Horizon Detection of Aircraft with the MADRE Radar," NRL Report 5898 (Secret Report, Secret Title), Feb. 1963

12. Gager, F.M., Morgan, G.A., Tesauro, C.B., Skaggs, G.A., and Zettle, E.N., "MADRE Performance Part 3 - Observations of February 12, 1962," (Unclassified Title), "MADRE Performance Part 3 - Very Long Range, Over-the-Horizon Detection of Aircraft with the MADRE Rdar," NRL Report 5991 (Secret Report, Secret Title), Aug. 1963

13. Gager, F.M., Morgan, G.A., Headrick, W.C., Tesauro, C.B., and Zettle, E.N., "MADRE Performance Part 4 - Observations of February 15, 1962," (Unclassified Title), "MADRE Performance Part 4 - Very Long Range, Over-the-Horizon Detection of Aircraft with the MADRE Radar," NRL Report 6019 (Secret Report, Secret Title), Jan. 1964

14. Ahearn, J.L., Headrick, W.C., Headrick, J.M., Tesauro, C.B., and Zettle, E.N., "Extended-Range Aircraft Tracking," NRL Report 6272 (Secret Report, Unclassified Title), May 1965

15. Davis, J.R., Thomason, J.F., Hudnall, J.M., Boyd, F.E., and Utley, F.H., "The Spectral Characteristics and Temporal Behavior of HF Radar Echoes from OTH Aircraft Targets," NRL Report 6371 (Secret Report, Unclassified Title), Nov. 1965

16. Thomason, J.F., Hudnall, J.M., Utley, F.H., and Boyd, F.E., "Detection of Aircraft Using OTH Radar," NRL Report 6508 (Secret Report, Unclassified Title), Jan. 1967

17. Jensen, G.K., and McGeogh, J.E., "Development of a Gate System for the Improvement of the MADRE Radar, Part I - System Theory, Calculations and Planning," (Unclassified Title), "Development of an Acceleration Gate System for the Improvement of the MADRE Radar, Calculations and Planning," NRL Report 5876 (Secret Report, Secret Title), Jan. 1963

18. Jensen, G.K., and McGeogh, J.E., "Development of a Gate System for the Improvement of the MADRE Radar, Part 2 - Development of Key Circuits and a Signal Simulator," (Unclassified Title), "Development of an Acceleration Gate System for the Improvement of the MADRE Radar, Part 2 - Development of Key Circuits and a Signal Simulator," NRL Report 5899 (Secret Report, Secret Title), Feb. 1963

19. Jensen, G.K., and McGeogh, J.E., "Development of a Gate System for the Improvement of the MADRE Radar, Part 3 - Experimental Verification of System Theory by Means of the Signal Simulator and Key System Components," (Unclassified Title), "Development of an Acceleration Gate System for the Improvement of the MADRE Radar, Part 3 - Experimental Verification of System Theory by Means of the Signal Simulator and Key System Components," NRL Report 5900 (Secret Report, Secret Title), Feb. 1963

20. Jensen, G.K., and McGeogh, J.E., "Development of a Gate System for the Improvement of the MADRE Radar, Part 4 - Laboratory Evaluation of the Complete System and Report of Recent Circuit Development," (Unclassified Title), "Development of an Acceleration Gate System for the Improvement of the MADRE Radar, Part 4 - Laboratory Evaluation of the Complete Acceleration Gate System and a Report of Recent Circuit Developments," NRL Report 5926 (Secret Report, Secret Title), Apr. 1963

21. McGeogh, J.E., Jensen, G.K., and Uniacke, C.L., "A 100-kc Quartz Crystal Comb Rejection Filter," NRL Report 5589 (Confidential Report, Unclassified Title), Feb. 1961

22. Lucas, D.L., and Hayden, G.W., "Predicting Statistical Performance Indexes for High Frequency Ionospheric Telecommunications Systems, ESSA Technical Report IER 1-ITSA 1, Aug. 1966

Appendix A

DESCRIPTION OF RAY-TRACING COMPUTER ROUTINE

BASIC RAY-TRACING TECHNIQUE

Prior to computation, the programmer is given the option of inserting ionospheric data in one of two forms: (a) as a true-height versus electron-density profile, or (b) as unreduced ionogram data.

In the event that true-height versus electron-density profiles are unavailable and ionogram data must be used, the virtual-height versus plasma-frequency data for the ordinary wave are reduced via a Budden Matrix subroutine in the program.

The method of solution is one devised by K. G. Budden of Cavendish Laboratories (A1), which involves the evaluation of a matrix known as the Budden Matrix. In this method it is assumed that the relationship between the virtual height $h'(f)$ and the true height z_0 of reflection for vertical incidence is given by

$$h'(f) = \int_0^{z_0} \mu'(N, f)\, dz ,$$

where $N(z)$ is the electron density at height z, and μ' is the group refractive index. In place of direct z-dependence, the electron density $N(z)$ can be expressed as a function of the plasma frequency $f_0(z)$, or

$$f_0(z) = \left[\frac{N(z)\, e^2}{4\pi^2 \epsilon_0 m}\right]^{1/2} .$$

This relationship allows $h'(f)$ to be expressed as

$$h'(f) = \int_0^{z_0} \mu'[N(z), f]\, dz .$$

Assuming that $z(f_0)$ is a monotonic function of f_0 in the interval $0 \leq f_0 \leq f$, f_0 can be made the variable of integration. Then we have

$$h'(f) = \int_0^{f} \mu'(f, f_0)\, \frac{\partial z}{\partial f_0}\, df_0 .$$

If $h'(f)$ is given as a tabulated function at equal intervals of the frequency Δf, then one may define

$$h'(n\Delta f) = h'_n .$$

The integration is then divided into discrete intervals of magnitude Δf. It is assumed that in the mth interval (where m is an integer index),

$$\frac{\partial z}{\partial f_0} \approx \frac{z_m - z_{m-1}}{\Delta f} .$$

Here, $z_m = z(m\Delta f)$; i.e., z_m is the height of reflection of a wave of frequency $m\Delta f$.

Then

$$h'_n \approx \sum_{m=1}^{n} \frac{z_m - z_{m-1}}{\Delta f} \int_{(m-1)\Delta f}^{m\Delta f} \mu'(n\Delta f, f_0)\, df_0 .$$

A matrix element $M_{n,m}$ is now defined by

$$M_{n,m} = \frac{1}{\Delta f} \int_{(m-1)\Delta f}^{m\Delta f} \mu'(n\Delta f, f_0)\, df_0 \quad \text{for} \quad m \leq n$$

and by

$$M_{n,m} = 0 \quad \text{for} \quad m > n .$$

M is a lower triangular matrix, and $h' = MDZ$, where

$$h' = \begin{bmatrix} h'_1 \\ h'_2 \\ h'_3 \\ \cdots \\ h'_n \end{bmatrix}$$

$$D = \begin{bmatrix} 1 & 0 & 0 & 0 & \cdots \\ -1 & 1 & 0 & 0 & \cdots \\ 0 & -1 & 1 & 0 & \cdots \\ 0 & 0 & -1 & 0 & \cdots \\ \cdots & \cdots & \cdots & \cdots & \cdots \end{bmatrix}$$

and

$$Z = \begin{bmatrix} z_1 \\ z_2 \\ z_3 \\ \cdots \\ z_n \end{bmatrix}$$

The product of the matrices M and D is lower triangular and nonsingular. It can therefore be inverted to give the solution

$$Z = [MD]^{-1} h' .$$

To evaluate the elements $M_{n,m}$ it is convenient to change the variable of integration. Defining $f_0/f = \sin \varphi$, the integral in the expression for $M_{n,m}$ becomes

$$\int_{\sin^{-1}\frac{(m-1)\Delta f}{f}}^{\sin^{-1}\frac{m\Delta f}{f}} \mu'(f, f \sin\phi) f \cos\phi \, d\phi$$

and can be evaluated by the method of Shinn and Whale (A2). The computer routine performs this integration using Simpson's rule. The elements of the product MD are given by

$$\begin{bmatrix} M_{11} & 0 & 0 & 0 & \cdots \\ M_{21} - M_{22} & M_{22} & 0 & 0 & \cdots \\ M_{31} - M_{32} & M_{32} - M_{33} & M_{33} & 0 & \cdots \\ \cdots & \cdots & \cdots & \cdots & \cdots \end{bmatrix}.$$

The inversion of this lower triangular matrix is then performed by Cholesky's method.

After the electron density versus height has been determined, an interpolation is performed using a sliding-parabola method. This method stores $N(h)$ versus the true height for every kilometer of altitude. The ionosphere is then assumed to consist of a series of earth-centered concentric spherical shells 1 km apart.

For cases where a higher frequency is used and much of the missile return data are from nonreflected (direct) rays, a Chapman distribution above the maximum electron density of the F_2 layer can be assumed. This distribution yields an exponential decrease in $N(h)$ versus height.

The electron density distribution for a Chapman layer is given by the relationship

$$N(h) = N_0 \exp[1 - \sec\chi \exp(-z)],$$

where $z = (h - h_{max})/H$, and χ is the solar zenith angle. H is the scale height at h. The program calculates the solar zenith angle at a point midway between the radar and the point of origin of the missile to be observed. Alternatively, the programmer may select the latitude and longitude where χ is calculated. $\cos\chi$ can be found for any location from the equation

$$\cos\chi = \sin\varphi \sin\delta + \cos\alpha \cos\varphi \cos\delta,$$

where φ is the geographic latitude, δ is the solar declination, and α is the local hour angle of the sun.

Snell's law is used to calculate the refraction of the rays through the ionosphere. Figure A1 is a sketch of the refraction geometry employed in the ray trace.

It can be seen in Fig. A1 that, for the interface between the ith and the $(i+1)$th layers, $\sin\beta_i n_i = \sin(\alpha_{i+1})\, n_{i+1}$, where n_i is the group index of refraction in layer i. Also,

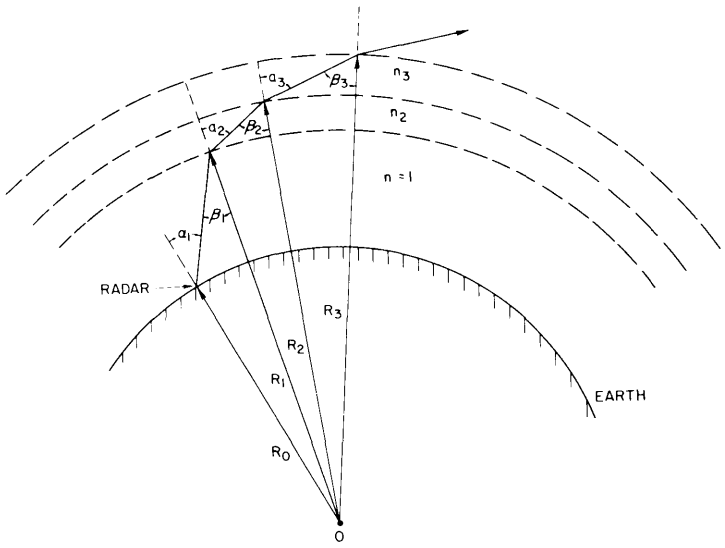

Fig. A1 - Ionospheric refraction geometry for the ray-tracing computer program

$$\frac{\sin\,(\pi - \alpha_{i+1})}{R_{i+1}} = \frac{\sin\,\beta_{i+1}}{R_i} .$$

Therefore,

$$\sin\,\alpha_i = \frac{R_i}{R_{i-1}} \sin\,\beta_i ;$$

and from Snell's law,

$$\sin\,\alpha_i = \frac{R_i}{R_{i-1}} \left[\frac{n_{i+1}}{n_i}\right] \sin\,\alpha_{i+1} .$$

Using this equation, and given an initial angle of elevation, it is possible to trace the path of any ray through the ionosphere.

Reflection of a ray is assumed to occur when $\alpha_{i+1} = \pi/2$. At this point

$$(n_{i+1})R_i = R_0 n_1 \sin\,\alpha_1 .$$

Since the variation of the product $(n_{i+1})R_i$ is a known function of height, the maximum height achieved by a ray for any elevation is determined. At this point the ray path is reflected through a vertical plane and returned to the earth.

At some elevation angles, particularly at the higher frequencies, there will be rays which are not reflected but which penetrate the F_2 layer. These rays are refracted in the same manner until they reach an arbitrary height of 200 km above the F_2-layer maximum. They are labeled with a flag in the program to differentiate them from the reflected rays contributing to the backscatter pattern.

MISSILE COVERAGE ROUTINE

Since the ionosphere being used is isotropic, each ray is assumed to lie in a plane. For this reason a Cartesian coordinate system with an origin at the center of the earth is used to describe both the ray paths and the missile path. The straight-line path of any ray between adjacent ionospheric layers is known as a ray segment and can be described completely by the x and y coordinates of its end points. The missile data read into the computer are latitude, longitude, time after launch in seconds, and height above the earth in kilometers. They are then transformed into the earth-centered coordinate system used in the ray trace. Although the missile path does not lie in a plane, it is not necessary to provide for this fact in determining whether or not any one ray and the missile trajectory will intersect. The height above the earth and the ground range from the radar are the only determining factors.

The ray trace is begun by assuming an initial elevation angle for the ray. The first ray segment extends from the radar site to the point where it reaches the first ionospheric layer; the x and y coordinates of the end points are placed in storage, and the equation for this straight-line segment is determined.

A parabola is then fitted to the first three points of the missile trajectory. A test is made to determine if an intersection between this parabola and the straight-line equation of the ray segment exists. If a point of intersection is found, another test is made to determine whether or not this intersection lies between both the end points of the ray segment and between the first and third points determining the parabola.

If the intersection test is affirmative, the ray is said to intersect with the missile path, and the computer goes to an intersect routine (described in the next section of this appendix). If it does not pass this test, the second, third, and fourth points of the missile data are used to determine another parabola, and the process is repeated.

If the ray segment does not intersect the missile path at any point, the program reinitiates the ray-tracing routine, another ray segment is determined, and the process is repeated. This procedure continues until the ray is either refracted back to the earth or penetrates the ionosphere to a point 200 km above the F_2-layer maximum.

INTERSECT ROUTINE

When a ray intersects the missile path, the latitude, longitude, and time of the intersection after launch are determined using a parabolic interpolation in which the height above the earth is the known quantity. These data are labeled MLATINT, MLONINT, and MTINT, respectively, and the height is designated MHINT. The program also stores the latitudes, longitudes, times, and heights of the missile immediately before and after the intersection.

Once the geographic coordinates of the intersection have been calculated, the bearing of the intersecting ray must be determined. Since the refracting medium is assumed to be isotropic, the ray then lies in a plane passing through the center of the earth, the location of the radar, and the point of intersection.

For convenience, a new three-dimensional coordinate system is now defined by the equations

$$x = r \sin(\theta) \cos(l),$$

$$y = r \sin(\theta) \sin(l) ,$$

and

$$z = r \cos(\theta) ,$$

where r is the distance from the earth's center, θ is the colatitude, and l is the longitude measured east from Greenwich.

The latitudes, longitudes, and heights of the ray segments' end points are transformed via these equations and stored as: XRAY1, YRAY1, and ZRAY1; and XRAY2, YRAY2, and ZRAY2.

The three latitudes, longitudes, and heights of the missile (those preceding intersection, those at intersection, and those immediately after intersection) are also transformed, and labeled: XVMIS1, YVMIS1, ZVMIS1, XVMIS2, YVMIS2, and ZVMIS2; and XVMIS3, YVMIS3, and ZVMIS3. The points of intersection are XVMIS2, YVMIS2, and ZVMIS2.

The velocity vector of the missile at intersection is determined from the equations

$$MV_x = \frac{(x_2 - x_1)(t_3 - t_2)^2 + (x_3 - x_2)(t_2 - t_1)^2}{(t_3 - t_1)(t_3 - t_2)(t_2 - t_1)} ,$$

$$MV_y = \frac{(y_2 - y_1)(t_3 - t_2)^2 + (y_3 - y_2)(t_2 - t_1)^2}{(t_3 - t_1)(t_3 - t_2)(t_2 - t_1)} ,$$

and

$$MV_z = \frac{(z_2 - z_1)(t_3 - t_2)^2 + (z_3 - z_2)(t_2 - t_1)^2}{(t_3 - t_1)(t_3 - t_2)(t_2 - t_1)} ,$$

where

$$x_i = \text{XVMIS}i , \text{ etc.}$$

$$\mathbf{v}_{mis} = \mathbf{i} MV_x + \mathbf{j} MV_y + \mathbf{k} MV_z .$$

The vector expression for the ray segment is simply

$$\mathbf{R} = \mathbf{i}(\text{XRAY2} - \text{XRAY1}) + \mathbf{j}(\text{YRAY2} - \text{YRAY1}) + \mathbf{k}(\text{ZRAY2} - \text{ZRAY1}) .$$

The aspect angle A between the ray and the missile at intersection is then

$$A = \cos^{-1}\left[\frac{\mathbf{v}_{mis} \cdot \mathbf{R}}{|\mathbf{v}_{mis}||\mathbf{R}|}\right] ,$$

and the component of velocity along the ray is

$$\mathbf{v}_{ray} = |\mathbf{v}_{mis}| \cos(A) .$$

The geomagnetic field is calculated at the point of intersection using the subroutine labeled BFIELD. The method used involves the expansion of the scalar geomagnetic

field potential, including the quadrupole terms, in geographic coordinates and using orthogonal Schmidt polynomials (A3).

The general scalar field potential can be expressed as the series expansion

$$V = r_0 \sum_{n=1}^{\infty} \sum_{m=0}^{n} \left(\frac{r_0}{r}\right)^{n+1} \left[g_n^m \cos(m\varphi) + h_n^m \sin(m\varphi)\right] P_n^m(\theta) ,$$

where

r_0 is the radius of the earth,

r is the distance from the center of the earth to the point at which the field strength is desired,

g_n^m and h_n^m are the Finch-Leaton coefficients,

φ is the geographic longitude measured east from Greenwich,

θ is the geographic latitude, and

$P_n^m(\theta)$ are Schmidt polynomials.

The expression for the quadrupole field is

$$V = r_0 \sum_{n=1}^{2} \sum_{m=0}^{n} \left(\frac{r_0}{r}\right)^{n+1} \left[g_n^m \cos(m\varphi) + h_n^m \sin(m\varphi)\right] P_n^m(\theta) ,$$

where

$$P_1^0(\theta) = \cos\theta ,$$

$$P_1^1(\theta) = \sin\theta ,$$

$$P_2^0(\theta) = 1/4\,[3\cos(2\theta) + 1] ,$$

$$P_2^1(\theta) = \frac{3}{2\sqrt{3}}\,[\sin(2\theta)] ,$$

and

$$P_2^2(\theta) = \frac{3}{2\sqrt{3}} \sin^2\theta .$$

The Finch-Leaton coefficients (A4) for the geographic coordinates (in cgs units) are

$$g_1^0 = -0.3055 \qquad g_2^1 = 0.0303$$

$$g_1^1 = -0.0277 \qquad h_2^1 = -0.0190$$

$$h_1^1 = 0.0590 \qquad g_2^2 = 0.0158$$

$$g_2^0 = -0.0152 \qquad h_2^2 = 0.0024 .$$

The spherical-coordinate components of the magnetic field induction (in cgs units) are

$$B_\rho = -\frac{\partial}{\partial r} V,$$

$$B_\theta = -\frac{1}{r}\frac{\partial}{\partial \theta} V,$$

and

$$B_\phi = -\frac{1}{r \sin\theta}\frac{\partial V}{\partial \phi},$$

where

$$B_\rho = \frac{2r_0^3}{r^3}\left[g_1^0 P_1^0(\theta) + (g_1^1 \cos\phi + h_1^1 \sin\phi) P_1^1(\theta)\right]$$

$$+ \frac{3r_0^4}{r^4}\left\{g_2^0 P_2^0(\theta) + (g_2^1 \cos\phi + h_2^1 \sin\phi) P_2^1(\theta) + \left[g_2^2 \cos(2\phi) + h_2^2 \sin(2\phi)\right] P_2^2(\theta)\right\},$$

$$B_\theta = \frac{r_0^3}{r^3}\left[g_1^0 \sin\theta - (g_1^1 \cos\phi + h_1^1 \sin\phi)\cos\theta\right]$$

$$+ \frac{r_0^4}{r^4}\left\{g_2^0 \frac{3\sin(2\theta)}{2} - (g_2^1 \cos\phi + h_2^1 \sin\phi)\frac{3}{\sqrt{3}}\cos(2\theta) + \left[-g_2^2 \cos(2\phi) - h_2^2 \sin(2\phi)\right]\frac{3}{\sqrt{3}}\sin\theta\cos\theta\right\},$$

and

$$B_\phi = \frac{r_0^3}{r^3 \sin\theta}\left[g_1^1 \sin\phi - h_1^1 \cos\phi\right] P_1^1(\theta)$$

$$+ \frac{r_0^4}{r^4 \sin\theta}\left\{(g_2^1 \sin\phi - h_2^1 \cos\phi) P_2^1(\theta) + \left[2g_2^2 \sin(2\theta) - 2h_2^2 \cos(2\phi)\right] P_2^2(\theta)\right\}.$$

These components are transformed into the Cartesian system as follows:

$$\boldsymbol{B} = \boldsymbol{i}\left[\sin\theta\cos\phi B_\rho + \cos\theta\cos\phi B_\theta - \sin\phi B_\phi\right]$$

$$+ \boldsymbol{j}\left[\sin\theta\sin\phi B_\rho + \cos\theta\sin\phi B_\theta + \cos\phi B_\phi\right] + \boldsymbol{k}\left[\cos\theta B_\rho - \sin\theta B_\theta\right].$$

The angle between the magnetic field and the ray at intersection, and the angle between the magnetic field and the direction of the missile at intersection, are placed into storage for printout. These quantities are, respectively,

$$A_{BR} = \cos^{-1}\left[\frac{\boldsymbol{B}\cdot\boldsymbol{R}}{|\boldsymbol{B}||\boldsymbol{R}|}\right]$$

and

$$A_{BV} = \cos^{-1}\left[\frac{\boldsymbol{B}\cdot\boldsymbol{v}_{mis}}{|\boldsymbol{B}||\boldsymbol{v}_{mis}|}\right].$$

The Mach number of the missile at intersection is calculated using the velocity of the missile and the velocity of sound at the height of intersection. A temperature-versus-height curve is stored permanently in the program with the height ranging from 0 to 500 km. When the height of intersection is determined, a linear interpolation is performed on the temperature-versus-height curve to determine the temperature at intersection. The velocity of sound (in m/sec) is given by

$$S = 20.1 \sqrt{T},$$

where T is the temperature in degrees Kelvin. The Mach number is then

$$M = \frac{|\mathbf{v}_{mis}|}{S}.$$

The doppler return from the missile can be found from the component of velocity along the ray, the pulse-repetition frequency (prf), the carrier frequency of the radar, and the electron density at the point of intersection. Before computation begins the prf and the carrier frequency are entered as input data. The phase velocity of electromagnetic waves at intersection is given by

$$v_p = c/n_i,$$

where c is the velocity of light in free space and n_i is the group index of refraction at the point of intersection. The expected doppler shift is then

$$\text{Dop} = f_c \left[\frac{v_p + |\mathbf{v}_R|}{v_p - |\mathbf{v}_R|} - 1 \right],$$

where v_p is the phase velocity at intersection, $|\mathbf{v}_R|$ is the magnitude of the velocity component of the missile along the ray, and f_c is the carrier frequency of the radar. On the radar display, however, the doppler shift of the received signal is folded about a frequency equal to one-half the prf. For example, for a prf of 90 Hz a true doppler shift from 0 Hz to 45 Hz would not be altered, but a doppler return between 45 Hz and 90 Hz would be displayed as a doppler return between 45 Hz and 0 Hz at the receiver, and a true doppler shift of 135 Hz would be viewed as 45 Hz, etc. Therefore, for predicting the appearance of doppler-shifted signals on the radar display, a routine has been included in the program to compute the "folded" or "ambiguous" doppler.

The ground range, the group path, and the true slant range to the missile along the intersecting rays are also calculated. In the ray-tracing process, the length of each ray segment is added to a variable in storage labeled APATH, which has been preset to zero prior to each ray trace. When the ray intersects the missile path the length of the ray segment, from its point of origin to the point of intersection is calculated. Then APATH is added to this length, and this sum, which is the slant range to the missile, is placed in storage as SRANGEM. During the ray trace, in a similar manner, the length of each ray segment divided by the index of refraction gives the group length of that segment, and the group lengths are accumulated as a variable labeled TGRP. This quantity is set to zero prior to each tracing. The length of the intersecting ray segment, from its point of origin to the point of intersection is divided by the appropriate group index of refraction for that segment and stored, and the value of TGRP is added. The resulting group path to the missile is placed in storage as GPATHM.

The total length of the segments are added to APATH, until the tracing of that particular ray is completed; this quantity then gives the total slant range of the ray. The value of TGRP is treated in the same manner. The ground range to the missile at the point of intersection is found by calculating the angle subtended in the earth-centered system by a great-circle arc from the radar to the projection onto the surface of the earth of the point of intersection of the ray and the missile trajectory. This angle is multiplied by the average earth radius of 6368 km to give the ground range. The total ground range of each ray is found by accumulating the angles subtended at the center of the earth by each ray segment until the ray has either penetrated the ionosphere to a height of 200 km above the F_2-layer maximum or has returned to earth.

The antenna pattern is determined from the product of the separate calculations of the vertical and the azimuthal patterns. A description of the method used for this procedure is as follows: measured vertical antenna patterns for three different frequencies from 0 degree to 30 degrees elevation are entered in permanent storage. The expected vertical gain pattern at any operating frequency is calculated independently on the basis of each of the three given patterns, yielding three values of the expected gain. The final vertical gain for any ray from 0 degree to 30 degrees in elevation is then obtained by a weighted average of the three predicted gains. The weighting factor used is $1/|\lambda_0 - \lambda_m|$, where λ_0 is the wavelength at the operating frequency, and λ_m is the wavelength at the measured frequency. This procedure makes the final result most closely approximate the prediction from the measured gain nearest the operating frequency. The azimuthal gain of any ray intersecting the missile is calculated by assuming that the bearing of the ray is equal to the bearing of the great-circle arc from the radar site to the projection of the intersection on the surface of the earth. The deviation of the ray from the center of the beam (which had been entered as data prior to calculation) is then used to calculate the reduction in gain due to the azimuthal antenna pattern. This operation is accomplished by fitting a parabola to the dependence of the azimuthal gains upon the deviation from beam center. The deviation from the center of the beam is also predicted from three measured sets of data at three frequencies. The final gain of an intersecting ray is simply the product of the vertical and the azimuthal gains. No azimuthal gain is predicted, however, for a nonintersecting ray.

OUTPUT

Plot

The following five plots are made from the original ray-tracing program:

1. A plot of the ray paths which do not completely penetrate the ionosphere, but which return to the earth and thereby contribute to the ground backscatter. The missile trajectory is also shown to give a visual display of radar coverage after launch. The scale of height above the surface of the earth is expanded by a factor of two, and the separation of the rays in elevation is weighted according to the vertical antenna pattern to give a better understanding of the coverage.

2. A plot of all rays which do not penetrate the ionosphere, but which are refracted back to earth. This plot is incremented by 1 degree in elevation and has an undistorted height scale. The missile path is also drawn on this plot.

3. A plot of the "folded" or "ambiguous" doppler, versus time after launch, expected from all intersecting rays.

4. A plot of the Mach number of the missile versus the time after launch.

5. A plot of the true doppler versus the time expected from all intersecting rays.

Printout

Printout from the rays not intersecting the missile path consists of the following:

1. RACOUNT — an index which tells the ray sequence in elevation. At present the increment in elevation angle is 0.1°, i.e., Racount = 1 indicates Elevation = 0.1°, Racount = 2 indicates Elevation = 0.2°, etc.

2. Elevation angle in degrees of ray number RACOUNT.

3. Total slant range of ray number RACOUNT from the radar to the intersection with the earth.

4. Total group path of ray number RACOUNT from the radar to the intersection with the earth.

5. Ground range from the radar to the intersection of ray number RACOUNT with the earth.

6. The three vertical gains predicted for ray number RACOUNT, by the three measured vertical antenna patterns.

7. The final gain obtained by a weighted average of the three gains printed above.

8. The words NO AZIMUTHAL SIGNIFICANCE for a ray which does not intercept the missile.

Printout from the rays intersecting the missile path consists of the following:

1. RACOUNT (same as before).

2. The elevation angle in degrees of ray number RACOUNT.

3. Total slant range of ray number RACOUNT from the radar to the intersection with the earth.

4. Total group path of ray number RACOUNT from the radar to the intersection with the earth.

5. Total ground range from the radar to the intersection of ray number RACOUNT with the earth.

6. Time after launch at which ray number RACOUNT intersects the missile.

7. Height above the earth at which ray number RACOUNT intersects the missile.

8. Slant range along ray number RACOUNT from the radar to the missile.

9. Group path along ray number RACOUNT from the radar to the missile.

10. Ground range from the radar to the missile at the point of intersection with ray number RACOUNT.

11. Bearing of the missile from the radar at the time of intersection with ray number RACOUNT.

12. Velocity of the missile at the time of intersection with ray number RACOUNT.

13. Mach number of the missile at the time of intersection with ray number RACOUNT.

14. Aspect angle between the ray and the direction of the missile at the time of intersection.

15. The component of the missile velocity in the direction of ray number RACOUNT at the time of intersection.

16. The doppler shift which would be expected at the time of intersection, assuming the phase velocity of light to be 3×10^8 m/sec.

17. The actual doppler shift expected at the time of intersection with ray number RACOUNT, taking into account the rate of change in phase path.

18. The "folded" doppler which is actually displayed as a result of reflection about one-half the prf.

19. The magnitude of the geomagnetic field strength at the point of intersection between ray number RACOUNT and the missile.

20. The angle between the geomagnetic field and the velocity of the missile at the point of intersection with ray number RACOUNT.

21. The angle between the geomagnetic field and ray number RACOUNT at the point of intersection with the missile.

22. The three vertical gains predicted for ray number RACOUNT from the measured antenna patterns.

23. The vertical gain of ray number RACOUNT computed from a weighted average of the three predicted vertical gains.

24. The decrease in gain for ray number RACOUNT due to the azimuthal deviation from the beam center at intersection with the missile.

25. The total gain for ray number RACOUNT, which is a product of the vertical and the azimuthal gain factors.

REFERENCES

A1. Budden, K.G., "A Method for Determining the Variation of Electron Density with Height ($N(z)$ curves) from Curves of Equivalent Height Against Frequency ((h', f) curves)," Physics of the Ionosphere, Report of Phys. Soc. Conference, Physical Society, London, 1955, pp. 332-339

A2. Shinn, D.H., and Whale, H.A., "Group Velocities and Group Heights from the Magneto-ionic Theory," J. Atmos. Terres. Phys. 2(No. 2):85-105 (1951)

A3. Chapman, S., and Bartels, J., Geomagnetism, Vol. II, Oxford:Clarendon Press, 1940

A4. Pennington, R.H., "Equation of a Charged Particle Shell in a Perturbed Dipole Field," J. Geophys. Res. 66:709-712, 1961

Appendix B

DESCRIPTION OF THE BACKSCATTER SYNTHESIS ROUTINE

The backscatter synthesis subroutine is available for use with the basic ray-tracing program. Input data peculiar to this program are the twelve-month running average sunspot number, the Greenwich hour angle and declination of the sun at the time of the experiment, the time duration of the radar pulse, the maximum delay time (in milliseconds) at which the ground backscatter return for a one-hop mode can be expected normally about 25 msec), the peak power (in megawatts) of the radar pulse, and the ground specular-reflection coefficient. The last parameter is at present arbitrarily assumed to be 0.97. All other data are obtained from the ray-trace program.

An assumption basic to this routine is that the energy contained between two adjacent rays is distributed uniformly in elevation. Adjacent rays are said to form an energy flux-tube which, when refracted and returned to the ground, illuminates an annulus on the earth's surface. Figure B1 illustrates a flux tube of elevation ϵ and azimuthal width $\Delta\phi$, and the ground area illuminated by this flux tube.

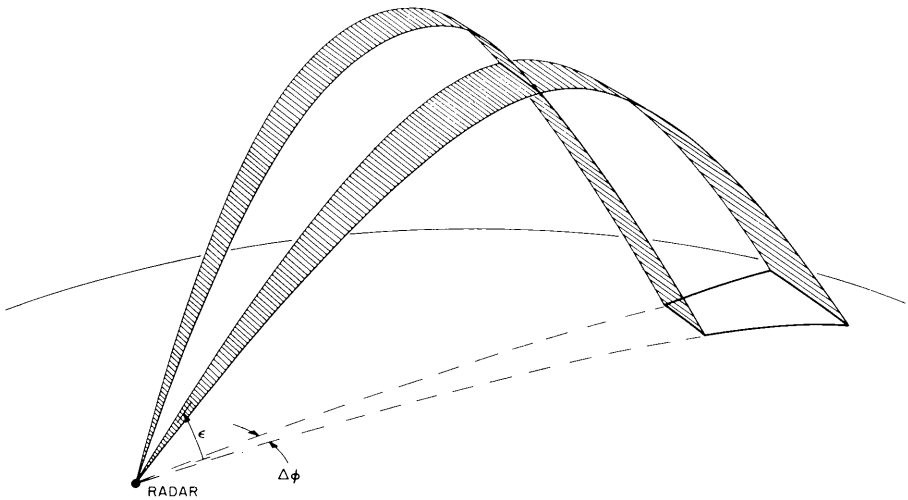

Fig. B1 - Sketch of a flux tube of elevation ϵ and azimuthal angular width $\Delta\phi$ between the radar transmitter and the earth after an ionospheric traversal

The transmitted energy contained between two adjacent rays will undergo nondeviative absorption as it passes through the ionospheric D layer. A ray which is refracted back to the earth will pass through the D layer twice, so it is necessary to calculate the absorption for both traversals of the D layer.

Referring to Fig. B2, a ray at an angle of elevation ϵ will travel in a straight line (assuming no atmospheric deviation) until it strikes the D layer at an assumed height of

75 km. The ground range from the radar to the intersection of the ray with the D layer is given by

$$R_D = R_0 \left\{ \cos^{-1} \left[\frac{R_0 \cos(\epsilon)}{(R_0 + 75)} \right] - \epsilon \right\},$$

where R_0 is the radius of the earth. R_D is also the ground range from the intersection of the downcoming ray with the D layer to its intersection with the earth.

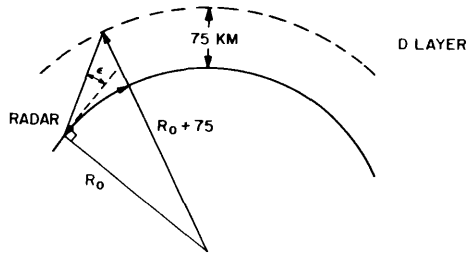

Fig. B2 - Ray geometry for D-layer absorption calculation

Because the energy in the flux tubes is contained between two adjacent rays, the appropriate parameters (elevation, ground range, and vertical antenna gain) averaged over a flux tube are computed for use in these calculations.

Once R_D has been determined the geographic coordinates of the radar and the average ground range of the flux tube are used to calculate the latitudes and longitudes at the points of penetration of the D layer. The zenith angle of the sun at these points is calculated using the equation

$$\cos \chi = \sin \phi \sin \delta + \cos \phi \cos \delta \cos \alpha,$$

where ϕ is the geographic latitude, δ is the solar declination, and α is the local hour angle of the sun.

The absorption for a single transit of the D layer (22) is given by

$$Ab = \frac{615.5\,(1.0 + 0.0037S)\,[\cos(0.881\chi)]^{1.3}\,(f_c + f_h)^{-1.98}}{\cos(\phi_D)},$$

where

Ab is the absorption in decibels,

S is the running average monthly sunspot number,

f_c is the frequency of the radar,

f_h is the electron gyro frequency, assumed to be 1.42 MHz, and

ϕ_D is the angle of intersection between the flux tube and the D layer.

This quantity is calculated for both the upgoing and downcoming D-layer transits of each flux tube. Thé fraction of energy from each flux tube that returns to the ground after absorption is then stored as $RHOA(I)$:

$$RHOA(I) = \exp(-Ab/8.7),$$

where I indexes each flux tube.

The ratio of the energy transmitted through a given flux tube I incident on the Ith annulus on the surface of the earth to the total energy transmitted is given by

$$ERG(I) = \frac{[\epsilon(I+1) - \epsilon(I)] \cos(\bar{\epsilon})}{4\pi} \bar{G}_v G_{AZ}[RHOA(I)],$$

where

$\bar{G}_v$ is the average vertical gain at the initial elevation angle of the flux tube,

$\epsilon(I)$ is the elevation angle of ray I which forms the lower boundary of the flux tube, and

G_{AZ} is the azimuthal gain factor, which is an integration of the azimuthal gain pattern over the entire beamwidth of the antenna at the operating frequency.

Here G_{AZ} is calculated using a six-point interpolation of the measured azimuthal gain factors versus the frequency. This energy ratio, $ERG(I)$, is calculated for all flux tubes which return to the earth. The ray-trace program makes available to the backscatter-synthesis subroutine the ground range from the radar to each returning ray, so that the distribution of the energy on the ground versus the distance from the radar can be calculated.

The backscatter-synthesis subroutine divides the ground range from the radar along the center of the antenna beam into a series of 4-km increments. Starting with the first increment (which extends 4 km in ground range from the radar), the segment is added to a variable labeled RANGE (J), and a search is made of all flux tubes for any which return to the earth and overlap or partially overlap this segment. If there is no flux tube returning to this segment, the next segment is added to RANGE (J), and the search is repeated. When a flux tube is found to overlap a range segment, the energy ratio in this segment from the flux tube is calculated, using

$$E_{SEG}(J) = \frac{[ERG(I)]\, R_s}{R_F},$$

where R_F is the ground range over which the flux tube is distributed and R_s is the ground range inside the segment which is overlapped by the flux tube. If the segment lies entirely within the flux tube, R_s = 4 km. A search is made of all other flux tubes, and all energy ratios in this segment are accumulated and stored as $ERGT(J)$. The entire process is repeated until a complete distribution of energy ratios versus ground range from the radar has been calculated.

Then RANGE (J) is converted to RANGE (J - 0.5) to consider the energy ratio at the center of each segment. The energy ratio in each segment is converted to average power using the relationship

$$\bar{P}_j = [ERGT(J)]\,(\mathrm{prf})\,\frac{P_t}{2}\,(\text{pulse length}),$$

where prf is the pulse-repetition frequency, P_t is the peak power, and $ERGT(J)$ is the energy ratio. A factor of one-half is necessary to account for the cosine-squared pulse shape.

A semilogarithmic plot is then drawn of $\bar{P}_j$, in decibels below 1 mW versus RANGE (J).

Upon striking the earth, a certain percentage (ρ_{sp}) of the incident energy is specularly reflected; the remainder (1 - ρ_{sp}) is diffusely scattered. The diffusely scattered

energy is allowed to return to the radar either via the same flux tube by which it arrived or via any other tube whose area on the surface of the earth is wholly or partially within the area subtended by the initial transmission flux tube.

For return via the same mode, the entire amount of energy, modified by the scatter pattern, is available for retransmission; the fraction of the arrival energy available for return by this mode is given by

$$E_r = \left(\frac{A_c}{A_t}\right) E_t ,$$

where A_c is the area common to both tubes on the earth's surface, A_t is the area of the transmission tube on the earth's surface, and E_t is the arrival energy.

All return modes are modified by a scatter pattern $K(\epsilon)$ according to their elevation angle of departure. Although the scattering pattern is in general dependent on the terrain and the frequency, it is assumed in this subroutine that the scatter pattern is dependent only on the elevation angle of departure. For the calculations in this report $K(\epsilon)$ is allowed to be isotropic, although the programmer has the option of choosing a scattering coefficient which varies as even powers of $\sin \epsilon$, where ϵ is the angle of departure. A feature is being added to this subroutine to permit a variety of scattering models to be used.

The radar pulse length τ is read into the computer prior to computation. The pulse length in milliseconds is divided into twenty incremental units of time; each time unit is considered to be a small rectangular pulse of duration $\delta\tau$. The backscattered energy returned to the radar is calculated for each of these small incremental pulses, and the contributions from all pulses are integrated to obtain the total energy returned from the original cosine-squared radar pulse of length τ.

The arrival energy from an incremental pulse $\delta\tau$ for any transit tube, bounded by rays labeled with the integer indices I and $I+1$, is given by

$$E_t = \frac{[P_t][\delta\tau][\bar{G}_{vI}][G_{AZ}][RHOA(I)](\cos \epsilon)[\epsilon(I+1) - \epsilon(I)]}{4\pi} ,$$

where

P_t is the peak power,

$\delta\tau$ is the incremental unit of time,

$\bar{G}_{vI}$ is the average vertical gain between rays I and $I+1$,

G_{AZ} is the azimuthal gain factor (a 40-point Romberg integration, interpolated for the operating frequency from six stored frequencies ranging from 10 MHz to 30 MHz),

$RHOA(I)$ is the nondeviative absorption calculated for this tube, and

$\epsilon(I)$ is the elevation of ray number I.

The fraction of this arrival energy available for return through any tube, bounded by rays labeled with the integer indices J and $J+1$, is given by

$$E_{AV} = [E_t]\left[\frac{A_{IJ}}{A_I}\right](1-\rho_{sp})\,[K(\bar{\epsilon}_J)],$$

where E_t is the arrival energy from a pulse of duration $\delta\tau$, A_{IJ} is the ground area common to both tubes, A_I is the ground area covered by transmitting tube I, ρ_{sp} is the fraction of energy which is specularly scattered, and $K(\bar{\epsilon}_J)$ is the ground scattering coefficient for energy returned via a tube with an average departure angle $\bar{\epsilon}_J$.

The solid angle Ω by which the scattered energy is returned for the Jth tube is given by

$$\Omega_T = \Delta\phi\,[\epsilon_{(J+1)} - \epsilon_{(J)}]\cos\bar{\epsilon}_J,$$

where $\Delta\phi$ is the azimuthal increment. The energy diffusely scattered into the flux tube is given by

$$E_{DIF} = (E_{AV})\left(\frac{\Omega_T}{2\pi}\right)\frac{1}{2}.$$

The factor 1/2 accounts for random polarization of the returning energy. The energy E_{DIF} returning through tube J is subject to nondeviative absorption as it passes through the D layer. This absorption has been calculated for rays J and $J+1$ by the ray-tracing program, and is labeled $RHOA(J)$ and $RHOA(J+1)$. The average absorption is calculated for this flux tube and labeled $\overline{RHOA(J)}$. The total energy incident on the ground at the position of the receiving antenna is then given by

$$E_G = (E_{DIF})\,[\overline{RHOA(J)}].$$

This energy must be further reduced by the ratio of the effective antenna aperture to the area subtended on the ground by the flux tube J.

The area subtended at the antenna by the returning flux tube is given by

$$A_{ANT} = [\sin(\bar{\epsilon}_J)](\Delta\phi)\,[\mathrm{GRRANG}(J+1) - \mathrm{GRRANG}(J)](r_0)\left\{\sin\left[\frac{\overline{\mathrm{GRRANG}(J)}}{r_0}\right]\right\},$$

where

GRRANG(J) is the ground range covered by ray number J,

r_0 is the radius of the earth,

$\Delta\phi$ is the increment in azimuth occupied by tube number J, and

$\bar{\epsilon}_J$ is the average elevation angle of tube J.

The effective aperture of the antenna is given by

$$A_{AP} = \frac{c^2\bar{G}_{vJ}}{4\pi f_c^2},$$

where

c is the velocity of light,

$\bar{G}_{nJ}$ is the average vertical gain of the antenna for a ray returning at an average angle of elevation $\bar{\epsilon}_J$, and

f_c is the operating frequency of the radar.

This ratio is then given by

$$A_{RAT} = \frac{c^2 \bar{G}_{nJ}}{4\pi \sin(\bar{\epsilon}_J) f_c^2 \Delta\phi r_0 \sin\left[\frac{\overline{GRRANG(J)}}{r_0}\right] [GRRANG(J+1) - GRRANG(J)]}$$

The energy from an incremental pulse of duration τ, transmitted through flux tube I and returned through flux tube J, which is received by the antenna, is then

$$\left[E_{TOT}\right]_{IJ} = E_G A_{RAT}.$$

The power received due to the incremental pulse of duration $\delta\tau$ is determined by dividing the total energy received from this pulse, $(E_{TOT})_{IJ}$, by the difference between the maximum and the minimum delay times $(TD_{IJ}^{max} - TD_{IJ}^{min})$ at which energy is received due to this pulse.

The minimum delay time is calculated by adding the smallest delay time possible, for that portion of transit tube I which impinges upon the area common to both transit tube I and return tube J, to the smallest delay time possible for that portion of return tube J which exists from this common area. The maximum delay time possible is calculated in a similar manner. The power received by this incremental pulse is then given by

$$[P_{\delta\tau}]_{IJ}(t) = \frac{(E_{TOT})_{IJ}}{TD_{IJ}^{max} - TD_{IJ}^{min}}, \qquad TD_{IJ}^{min} \leq t \leq TD_{IJ}^{max}.$$

The actual pulse shape is given by

$$f(t) = P_T \cos^2\left[\frac{\pi}{\tau}\left(t - \frac{\tau}{2}\right)\right], \qquad 0 \leq t \leq \tau,$$

where τ is the pulse length.

To obtain the total power received from all modes of propagation, all the $(P_{\delta\tau})_{IJ}$ must be summed along the delay time base. This sum is labeled $P_{\delta\tau}(t)$.

If at some delay time $t = m\delta\tau$ (where m is an integer index) greater than the pulse length τ the first increment of the pulse is superimposed upon the $P_{\delta\tau}$ distribution, then the second increment is superimposed at delay time $(m-1)\delta\tau$, the third increment is superimposed at delay time $(m-2)\delta\tau$, and so forth. The final, nth $\delta\tau$ increment of the pulse will be superimposed on the $P_{\delta\tau}$ distribution at $(m-n)\delta\tau$. This is illustrated in Fig. B3.

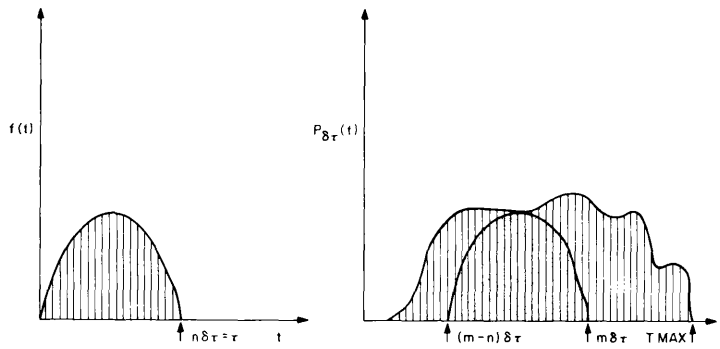

Fig. B3 - Illustration of the use of convolution to yield the amplitude of the received ground-backscattered energy due to an illuminating pulse of arbitrary pulse-shape

The power received at some delay time t is then given by

$$P(m\delta\tau) = \sum_{k=1}^{n} P_{\delta\tau}(m-k+1)f(k\delta\tau).$$

The power $P(m\delta\tau)$ in decibels below a millivolt versus the delay time is plotted on a semilogarithmic scale. This power $P(t)$ is then converted to voltage, and the voltage $V(t)$ versus the delay time t is plotted. The plot of voltage versus delay time yields the predicted backscatter pattern, which may be compared with the measured ground backscatter.

Security Classification

DOCUMENT CONTROL DATA - R & D

(Security classification of title, body of abstract and indexing annotation must be entered when the overall report is classified)

1. ORIGINATING ACTIVITY (Corporate author)	2a. REPORT SECURITY CLASSIFICATION
Naval Research Laboratory Washington, D.C. 20390	2b. GROUP

3. REPORT TITLE

APPLICATIONS OF COMPUTER-AIDED IONOSPHERIC RAY-TRACING TECHNIQUES TO THE ANALYSIS OF OVER-THE-HORIZON RADAR SIGNATURES FROM LAUNCH-PHASE ROCKETS [Unclassified Title]

4. DESCRIPTIVE NOTES (Type of report and inclusive dates) A final report on the problem; work on this problem and associated problems continues.

5. AUTHOR(S) (First name, middle initial, last name)

J.R. Davis, M.E. Harding, J.W. Willis, and F.H. Utley

6. REPORT DATE	7a. TOTAL NO. OF PAGES	7b. NO. OF REFS
July 30, 1968	74	26

8a. CONTRACT OR GRANT NO.	9a. ORIGINATOR'S REPORT NUMBER(S)
NRL Problem R02-23	
b. PROJECT NO.	NRL Report 6731
USAF MIPR FD2310-7-0016	
c.	9b. OTHER REPORT NO(S) (Any other numbers that may be assigned this report)
d.	

10. DISTRIBUTION STATEMENT

11. SUPPLEMENTARY NOTES	12. SPONSORING MILITARY ACTIVITY
	Department of the Air Force (Rome Air Development Center), Rome, New York 13440

13. ABSTRACT

NRL's Madre research radar has been used for 11 years in a long-term investigation of the applicability of high-frequency ionospheric radar for detecting and tracking over-the-horizon aircraft and launch-phase rocket vehicles. Associated with this investigation is a concurrent and complementary study of the ionosphere as a propagating medium and of the earth as a scatterer for decameter electromagnetic waves.

An ionospheric ray-tracing program has been developed to perform a propagation analysis which uses ionosonde data from stations located along the transmission path to describe a family of propagation rays between the radar site and a selected target region. This program permits ground-backscatter profiles to be synthesized and compared with observed ground-backscatter data and allows the adjustment of such parameters as the angular dependence of the earth's scattering coefficient and nondeviative absorption of the electromagnetic energy in the ionosphere, to achieve a fit to the observed data. The resultant propagation model is used to predict the behavior of a launch-phase missile's signature as detected by an over-the-horizon radar under appropriate propagation conditions.

(over)

14. KEY WORDS	LINK A		LINK B		LINK C	
	ROLE	WT	ROLE	WT	ROLE	WT
Radar Over-the-horizon radar Launch-phase missile detection Coherent signal processing Velocity processing Acceleration processing Coherent pulse doppler Radar propagation paths Ionospheric electron density Simulated propagation paths Ground-backscatter echo						

The results of this computer-aided propagation analysis were compiled for several Polaris missile launches on the Eastern Test Range and were then compared with data acquired by the Madre radar. The ray-tracing technique has been generally quite successful, for the cases treated, in predicting:

(a) the position and the extent of the ground-backscatter echo,

(b) the locations and the relative amplitude of localized peaks and nulls in the illumination caused by ionospheric layer structure,

(c) the onset and the loss time of missile signatures (with some exceptions),

(d) the doppler shift of missile signatures, including multipath effects, and

(e) the temporary losses of signal due to voids in the illumination of the missile.